JAHRESBERICHT
2006

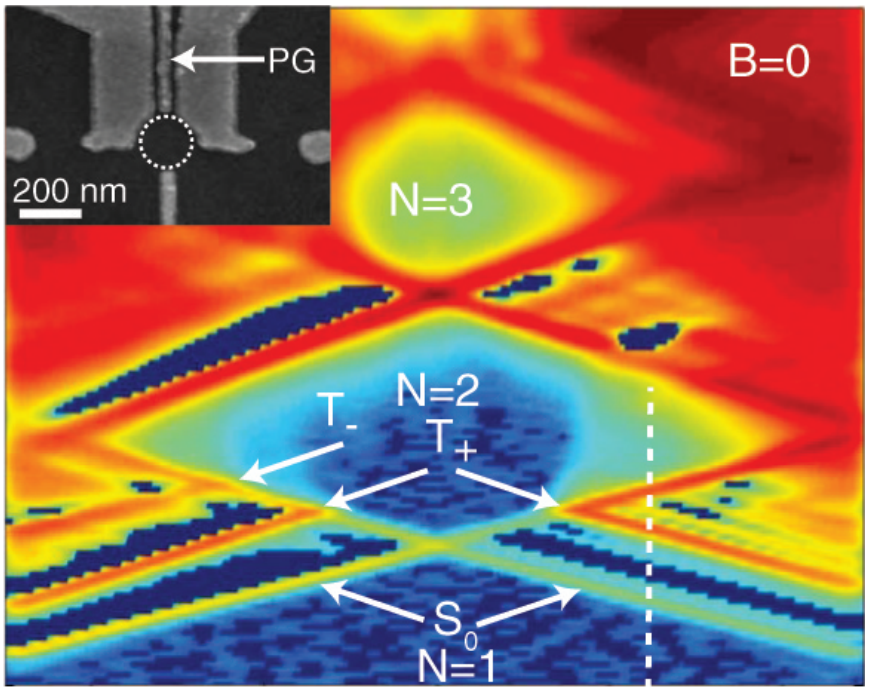

Laboratorium für Festkörperphysik
der
Eidgenössischen Technischen Hochschule
Zürich

Cover page:

Excitation spectrum of two correlated electrons in a lateral quantum dot. The figure shows the differential conductance $dI/dV_{\rm bias}$ of the quantum dot versus bias voltage (x-axis) and plunger gate voltage (y-axis), taken at zero magnetic field. Electron numbers N are indicated in the diamonds. The arrows mark the transitions between the one electron ground state and the 2e spin-singlet (S0) and spin-triplet states (T). Inset: scanning electron micrograph of the sample. The quantum dot is marked with a dotted circle and PG labels the plunger gate.

Phys. Rev. Lett. **96**, 126806 (2006)

This annual report was edited by: S. Gustavsson

PREFACE

The Laboratory for Solid State Physics at ETH Zurich is pleased to present the Annual Report for 2006. This report summarizes the highlights of the research groups who have continued their highly productive activities in a diverse spectrum of topics.

Members of the Laboratory are committed to all aspects of teaching physics students on all levels, as well as for students in other departments at ETH on the introductory level and in lab courses.

Two extraordinary events marked the 2006 calendar: In May, an international expert panel reviewed the ETH Physics Department and the Laboratory for Solid State Physics received high recognition, as did the Department as a whole. Later in the year, the Laboratory celebrated its 50th anniversary. Its history was revisited in a series of presentations: from the visionary founding by Prof. Dr. Georg Busch, through expansion of research topics with broad impact on science and technology, to today's thriving research and teaching activities.

We would like to express our heartfelt thanks to the many people who have supported us, particularly to the technical and administrative staff of the Laboratory and of the Physics Department whose expertise and dedication are a foundation for effective research and teaching.

For providing continued support and the substantial financial means we would like to thank the Schulleitung of ETH Zürich, the Swiss National Science Foundation, KTI, our partners in industry, and all other external sources.

Last, but not least, we are very grateful to Prof. Dr. Klaus Ensslin who has been serving the Laboratory as Vorsteher for so many years.

Zürich, May 2007

Der Vorsteher

Prof. Dr. B. Batlogg

Contents

Chapter 1

Physics of new materials

(http://www.pnm.ethz.ch/)

Head
Prof. Dr. Bertram Batlogg

Academic Staff

Markus Brühwiler	Claudia Goldmann	Simon Haas
Wolfgang Kalb	Kurt Pernstich	Benjamin Rössner
Dr. Arno F. Stassen	Dr. Hans von Känel	Dr. Peter Cristea

Technical Staff

Kurt Mattenberger	Hans Peter Staub

Administrative Staff
Gabriela Strahm

High pressure materials synthesis group

Head
Dr. Janusz Karpinski

Academic Staff

Andrey Belousov	Dr. Zbigniew Bukowski	Jan Jun
Dr. Sergiy Katrych	Dr. Nikolai Zhigadlo	

Academic Guests
Dr. Andrey V. Mironov, Moscow State University, Moscow (Russia)
Dr. Roman Puzniak, Polish Academy of Sciences, Warsaw (Poland)
Dr. Krzysztof Rogacki, Polish Academy of Sciences, Wroclaw (Poland)
Mauro Tortello, Politecnico di Torino, Torino (Italy)

Semester/Diploma Students
Priska Studer

Melting and freezing

Head
Prof. Dr. Jörg Bilgram

Academic Staff
Oliver M. Wittwer Marco Fell

Technical Staff
Hansrudolf Aeschbach

Optical Spectroscopy

Head
Prof. Dr. L. Degiorgi

Academic Staff
F. Pfuner M. Lavagnini A. Sacchetti (until June 2006)

Technical Staff
J. Müller

Administrative Staff
I. Heer-Mettler

Doctoral theses
Claudia Goldmann
Charge transport in organic single crystal field-effect transistors
07.04.2006

Markus E. Brühwiler
Groundstate properties of electrons on the triangular lattice
04.07.2006

Simon Haas
Crystal structure analysis and trap spectroscopy in organic semiconducting crystals
02.06.2006

Benjamin Rössner
Electric transport phenomena in high mobility strained-Ge channels
08.08.2006

Oliver Marc Wittwer
Solidification of xenon: Instabilities leading to complex structures
13.06.2006

Diploma theses
Thomas Mathis
WS 2005/06

Fabian Meier
WS 2005/06

Sieghard Seyrling
WS 2005/06

Semester Students

Thomas Brenner
Jakob Kanter
Peter Maurer
Julian Perrenoud
Fabien Wildhaber
Roger Häusermann
Tobias Kesselring
Tobias Morf
Andreas Reinhard
Sarah Hellmüller
Amir Khiar
Patrick Nüesch
Tim Schulze

1.1 Organic semiconductor field-effect transistors of unprecedented electrical stability employing polymeric dielectrics

W. L. Kalb, T. Mathis, S. Haas, A. F. Stassen, and B. Batlogg

To take advantage of the processability of organic semiconductors by low-cost methods it is mandatory to employ easily processable gate dielectrics. Moreover, the performance of organic field-effect transistors critically depends on the surface of the gate dielectric. We have investigated several solution processable polymeric insulators in organic field-effect transistors such as the nonfluorinated materials polystyrene (PS), poly-α-methylstyrene (AMS) and polyvinylalcohol (PVA) as well as the fluoropolymer Cytop^{TM} (Fig. 1.1). The polymers were employed to either constitute all or part of the gate insulator. Particular attention was directed towards electrical stability which is a key issue for a successful commercialization.

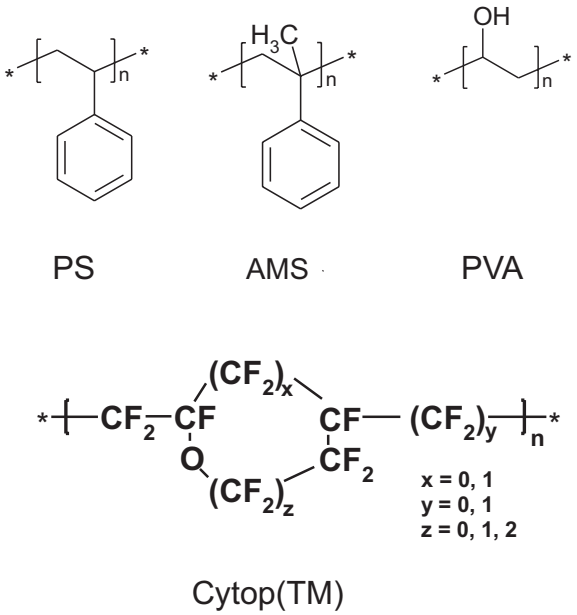

Figure 1.1: Chemical structure of the polymeric gate insulators polystyrene (PS), poly-α-methylstyrene (AMS), polyvinylalcohol (PVA) and Cytop^{TM}. The best devices were obtained with the amorphous fluoropolymer Cytop^{TM}.

The highly hydrophobic fluoropolymer Cytop^{TM} (**Cy**clic **T**ransparent **O**ptical **P**olymer) has an amorphous nature which leads to properties such as solubility, smooth thin-films and a high optical transparency. Employing this material as gate dielectric led to field-effect transistors with outstanding electrical stability. The rubrene and pentacene SC-FETs had a negligible current hysteresis, record subthreshold swings up to 0.75 nF V/(dec cm^2) and a near zero onset voltage. Furthermore, extended gate bias stress only led to marginal changes in the transfer characteristics. Pentacene-based TFTs showed a very small current hysteresis and field-effect mobilities up to 0.7 cm^2/Vs.

Additionally, Cytop^{TM} thin films had a high dielectric breakdown field (9.8 MV/cm) which is remarkable for an organic insulator. The excellent device performance can be ascribed to the very high water repellency and smoothness of the insulator surface. Water at the insulator-semiconductor interface leads to deep/long-lived electronic states which are the cause of electrical instability. The highly hydrophobic Cytop^{TM} (water contact angle of $\sim 112°$) keeps the detrimental water molecules away from the critical interface. This is of particular importance, when the organic semiconductor is deposited onto the dielectric in air.

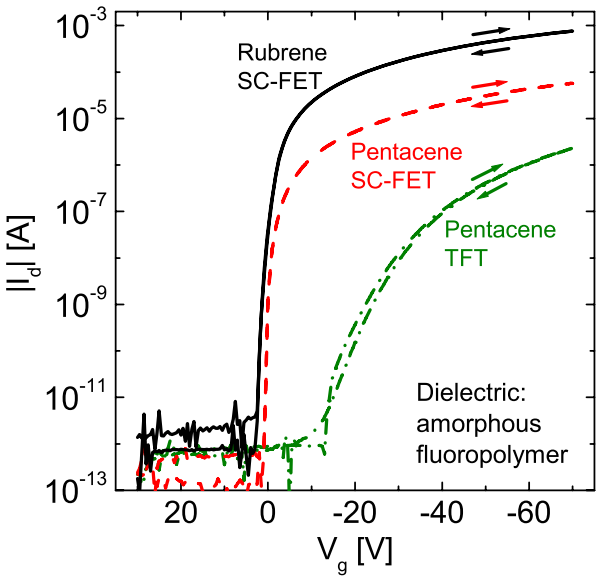

Figure 1.2: Transfer characteristics of a rubrene single-crystal FET, a pentacene SC-FET and a pentacene thin-film transistor with a Cytop^{TM} gate dielectric. The devices have an unprecedented electrical stability.

1.2 Organic field-effect transistors with novel semiconducing materials

S. Seyrling, S. Haas, A. F. Stassen, W. Kalb, and B. Batlogg
in collaboration with U. Berens, F. Bienewald, and H. J. Kirner, Ciba Specialty Chemistry, Basel

The market for organic electronics applications, such as OLED displays, radio-frequency identification (RFID) tags and other flexible devices, is expected to grow significantly in the near future. Our industry partner is about to enter the market. In order to achieve good electric performance and sufficient chemical stability, novel modifications or classes of molecules are synthesized.

To test these materials, we have fabricated field-effect transistors (FETs) with single crystals (SC) and thin films. Single crystals were grown by physical vapor transport in high purity argon, whereas thin films were thermally evaporated onto the dielectric layer, such as SiO_2 and polymers. The choice of the dielectric turns out to be crucial for the performance in terms of the charge carrier mobility, the onset voltage, and the electric stability of the devices. Charge trapping at the surface of the dielectric and charge transfer to/from the semiconductor seem to be the essential microscopic reason for the effect of the dielectric. In addition, the dielectric obviously governs the thin film growth. In particular, SC-FETs with Cytop^{TM} as the dielectric exhibit an exeptional quality of the characteristics and a remarkable stability against bias stress (cf. Section 1.1). On the other hand, devices with polystyrene coated SiO_2 as dielectric show a significant shift of the onset voltage of +19.5 V, i.e. the device is already turned on at zero gate voltage (see Fig. 1.3). Furthermore, prolonged gate bias stress shifts the transfer characteristic by 15–20 V in both directions (depending on the sign of the applied voltage). Subsequent relaxation, however, is very slow, and the recovery remains incomplete. In addition, long term stability measurements have been performed, both in inert atmosphere and room air. Finally, reliable electronic circuits depend on transistors which do not degrade with time nor show any detrimental bias stress effect.

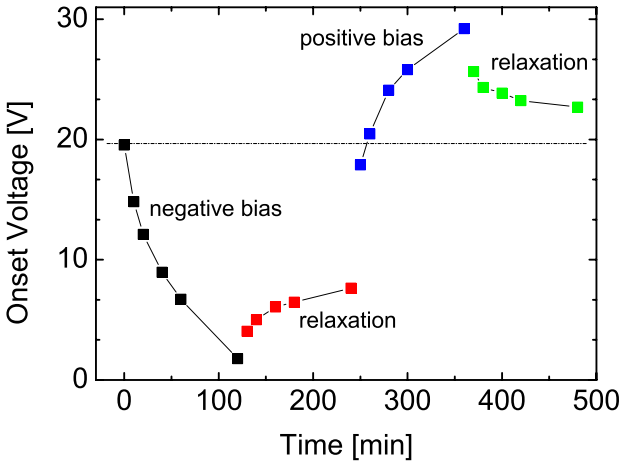

Figure 1.3: Gate bias stress and relaxation: Evolution of the onset voltage of a SC-FET (UBE 1089 on polystyrene coated SiO_2) during a bias stress measurement ($V_G = \mp 50$ V). The high initial onset voltage of 19.5 V is due to the polystyrene coating. The shift due to the gate bias stress is of comparable magnitude.

1.3 The Seebeck coefficient of two organic semiconductors

K. P. Pernstich, B. Rössner, and B. Batlogg

We have measured the Seebeck coefficient S in high mobility rubrene single-crystal field-effect transistors (FET) and pentacene thin film transistors. The hole density and concomitantly the Fermi level E_F in the transistor's channel is varied by the gate voltage. The Seebeck coefficient S near the threshold voltage ($V_{th} \approx 0$ V) is >1 mV/K, and decreases linearly with $\log(V_g)$ to < 0.4 mV/K at high gate voltages where the charge carrier density reaches the level of several per cent per molecule, illustrated in Fig. 1.4. Notably, S is temperature independent between 200 K and 295 K. The magnitude of $S(V_g)$ is significantly higher than expected for a hole gas with energy independent scattering rate and a constant density of band states. A quantitative estimate of the thermopower enhancement requires the knowledge of the Fermi level position relative to the mobility edge (transport energy). This gate-voltage dependent quantity is derived from a device model that reproduces the simultaneously measured output and the transfer characteristics of the FETs. With the knowledge of $E_F(V_g)$ the dependence of $S(V_g)$ can be explained over a wide range of carrier concentrations.

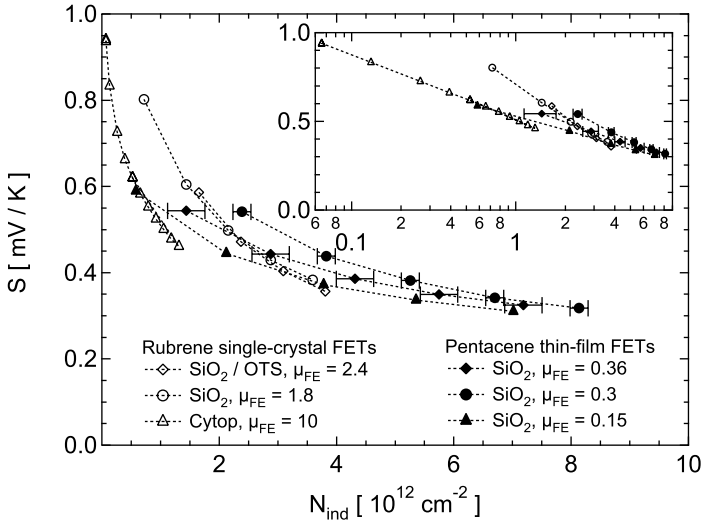

Figure 1.4: Measured Seebeck coefficient in rubrene single crystal FETs and pentacene thin film FETs employing various gate insulators.

1.4 Modelling the water related trap state created in pentacene transistors

K. P. Pernstich, D. Oberhoff, C. Goldmann, and B. Batlogg

As more and more organic electronic devices are integrated into commercial products, the study of the materials' intrinsic capabilities and of the limiting factors, such as defect formation, is of great significance. With the knowledge of the physical and chemical mechanisms causing degradation, ways can be found to fabricate more stable devices in a systematic manner. The importance of water in the degradation of the device performance has been described in several reports. Here we describe the modelling of the water related trap state formation found in pentacene single crystal transistors by Goldmann et al. [1]. After a prolonged application of a gate bias to pentacene single-crystal transistors ($V_g = -60$ V, 100 min), a pronounced kink was observed in the subthreshold region of the transfer characteristic as seen in Fig. 1.5.

We have used the FET model developed in our group [2] which allows to specify an arbitrary density-of-states (DOS) as illustrated in Fig. 1.5, and calculates the drain current for a given drain- and gate voltage $I_d(V_d, V_g)$. The model considers transport in extended states, and assuming only exponentially distributed tail states with a characteristic width of 25 meV yields curve (1) in Figure 1.5. The simulated current is higher than the measured one, clearly indicating the need to adapt the DOS. By introducing a discrete trap state, that is only located in the first pentacene monolyer and at an energy of 430 ± 50 meV from the valence band edge E_v (cf. Fig. 1.5), the unstressed characteristic is well described by curve (2) in the Figure. Increasing the density of the discrete trap state from 2 to 10.5×10^{18} /cm^3 describes the stressed characteristic as shown in curve (3). This clearly indicates that a trap state is formed in pentacene single-crystal transistors during a prolonged application of a gate bias. Since the traps are formed in a thin interface layer only, about 0.5 % of the pentacene molecules in the first monolyer are affected by bias stress. Our results can help identify the microscopic mechanism of trap formation by comparing the energetic position found from the simulations with results from computational chemistry. A possible origin of the trap state formation are oriented water molecules.

[1] C. Goldmann, D. J. Gundlach, and B. Batlogg, *Applied Physics Letters*, 88(6):063501, 2006.
[2] D. Oberhoff, K. P. Pernstich, D. J. Gundlach, and B. Batlogg, *Electron Devices, IEEE Trans.*, 54(1):17–25, 2007.

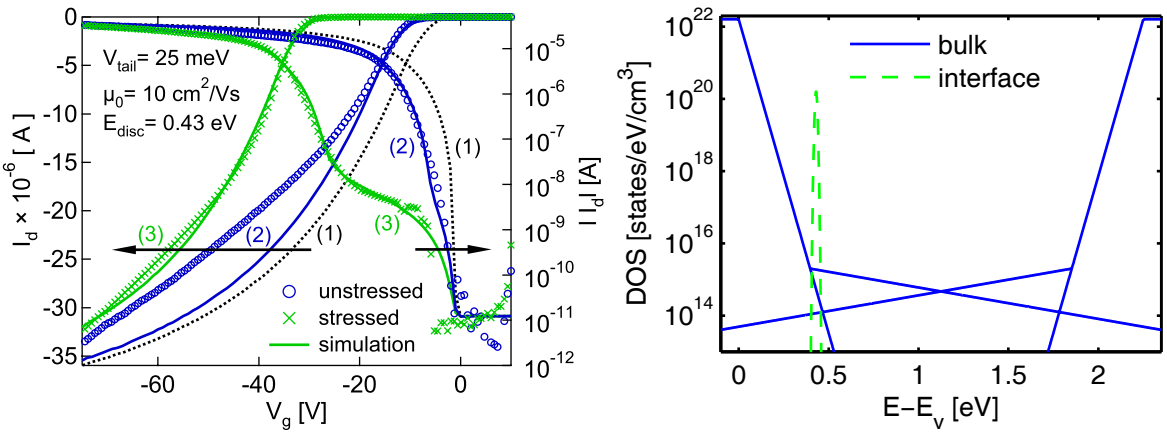

Figure 1.5: Transfer characteristics [left panel] of the stressed and the unstressed transistor (symbols) together with the simulation results (lines). Curves (1)-(3) are calculated using the DOS distribution shown in the right panel with a density of the discrete trap state of 0, 2 and 10.5×10^{18} /cm^3.

1.5 SiGe modulation doped heterostructures

B. Rössner, H. von Känel

in collaboration with D. Chrastina, G. Isella, J. Osmond (Politecnico di Milano)

One of the most important parameters of 2-dimensional systems is the effective mass derived from the density of states. For parabolic bands, it is equal to the effective mass determined from either the cyclotron resonance frequency or the temperature dependence of Shubnikov–de Haas (SdH) oscillations in a magnetic field B. Non-parabolicity, commonly encountered in hole bands, complicates the picture. High-mobility p-Ge/$Si_{0.3}Ge_{0.7}$ heterostructures grown by low-energy plasma-enhanced chemical vapor deposition (LEPECVD) were used as a model system to shed light on the influence of band non-parabolicity on the measurement of the effective mass.

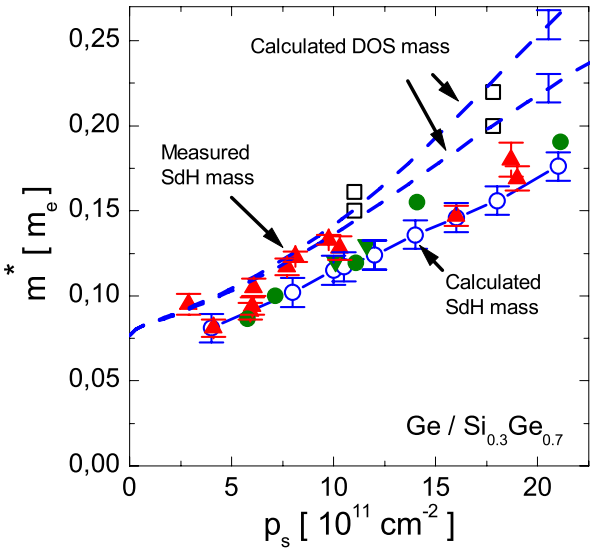

Figure 1.6: The experimental effective mass in Ge/$Si_{0.3}Ge_{0.7}$ heterostructures is strongly dependent on sheet carrier density p_s. Calculated SdH masses (○) match experiment, while calculated DOS masses (dashed lines by authors, open squares taken from Winkler et al., Phys. Rev. B 53, 10858 (1996)) exceed experimental data, especially at high carrier densities. Predicted DOS and SdH masses vary within the indicated error bars for well widths from 8 to 18 nm, and spacer widths from 4 to 10 nm. DOS masses were calculated for asymmetric potential wells (one sided doping), such that spin degeneracy is lifted, leading to two sets of distinct masses. The mass for symmetric wells would roughly lie midway in between the two. Experimental data by the authors (red triangles) and from Irisawa et al., Appl. Phys. Lett. 82, 1425 (2003) (green bullits SdH, green triangles CR).

To this end, both band mass and SdH mass were calculated within a 6×6 envelope function approximation as a function of hole density p_s in the strained-Ge channel. The theoretically derived SdH mass was found to agree both with our own experimentally measured masses as well as those from literature for similar heterostructures. By contrast, the (zero-field) density of states (DOS) mass coincides with measured SdH masses only for carrier densities below about 10^{12} cm^{-2}. With increasing density, however, the calculated DOS mass exceeds more and more the measured SdH mass. Since our calculations include the effect of nonparabolic bands both on DOS masses and simulated SdH masses, our results provide an upper limit of carrier densities up to which identification of the two remains permissible.

1.6 SDW–like ground state with strong Fermi surface gapping in Na_xCoO_2, $x \approx 0.8$

M. Brühwiler, B. Batlogg, S.M. Kazakov, J. Karpinski; in collaboration with D. Sheptyakov (PSI, Villigen)

In Na_xCoO_2 the electrons move on a triangular lattice and in the Na-rich composition range ($x \geq 0.75$) form a SDW ground state below $T_c \approx 22.5$ K with a small ordered moment. We have studied this Fermi surface instability with heat capacity, magnetic and transport measurements on a series of samples with various nominal Na content. All signatures of the Fermi surface instability are most pronounced in the samples with the highest nominal Na composition. The SDW phase is characterized by a jump ΔC at T_c and an associated reduction of the electronic density of states. This removal of DOS has been deduced from the high-temperature value of the Sommerfeld coefficient γ and the extrapolation from below 1K to $T \rightarrow 0$. Interestingly, the ratio $\Delta C/(\delta\gamma \cdot T_c) \approx 1.5$ is close to the BCS weak coupling value. Even more surprising is the observation that up to $\approx$ 80% of the DOS is removed in this Fermi surface instability. Crystal structure analysis at room temperature reveals for the SDW an orthorhombic symmetry and thus a slight distortion of the triangular lattice. This distortion is likely due to ordering of Na ions, influencing the potential experienced by the electrons in the CoO_2 layers. Thus the SDW-like state bears some similarity to the CDW-like state, which forms at $x = 0.5$ also in a distorted triangular lattice.

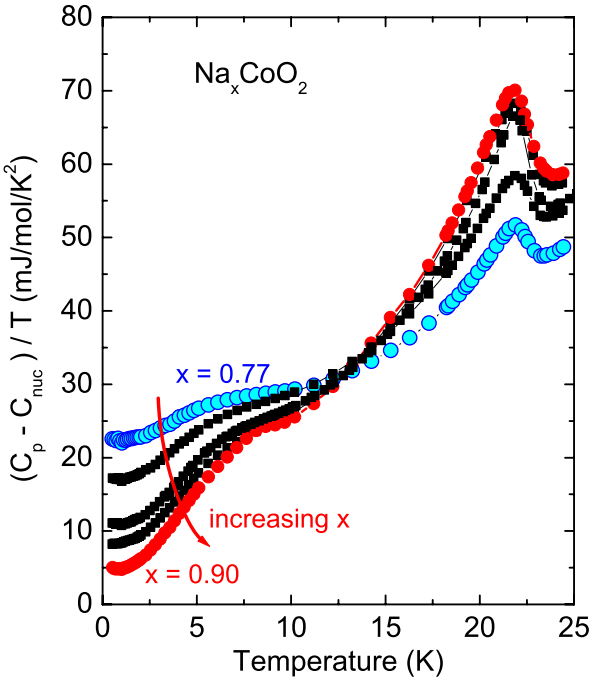

1.7 Crystal growth, phase diagram studies, structural and superconducting properties of $Mg_{1-x}Li_x(B_{1-y}C_y)_2$

N. D. Zhigadlo, S. Katrych, J. Karpinski, B. Batlogg in collaboration with R. Puzniak, K. Rogacki, M. Tortello, J. Jun, A. V. Mironov

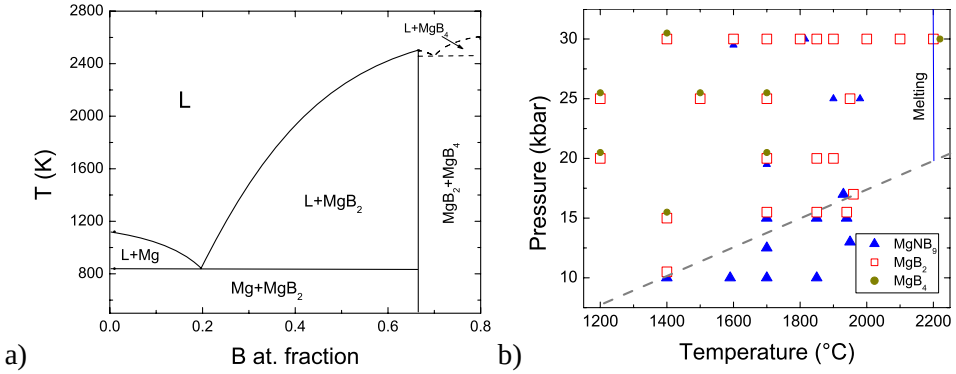

Figure 1.7: a) T-x phase diagram of the Mg-B system at 3 GPa plotted using our experimental data and some data of Ref. [1]. b) P-T phase diagram of Mg-B-N system. Symbols show phases observed in the samples. MgB_2 single crystals have been grown above 1800 °C.

Single crystals of $Mg_{1-x}Li_x(B_{1-y}C_y)_2$ were grown at temperatures between 1850 and 2000 °C and under pressure of 30 kbar in a cubic anvil apparatus. The effect of Li substitution for Mg and Li-C co-doping on the superconducting properties and crystallographic structure of MgB_2 single crystals has been investigated. Studies of the phase diagram of Mg-B and of the Mg-B-N system have been performed at 10-30 kbar and temperatures up to 2200 °C. Figure. 1.7 a) presents the phase diagram of Mg-B system obtained from our data and from the data of Ref. [1]. Accordingly, MgB_2 can be grown from solution at temperatures up to 2200 °C, as well as from the stoichiometric melt. Figure 1.7 b) shows the P-T phase diagram of the Mg-B-N system used for the crystal growth from solution with the phases obtained in our experiments. Additionally, the BN hexagonal phase and Mg have been present in all samples (not shown). Above the dashed line MgB_2 plus BN are stable phases. MgB_2 crystals grew at T>1800 °C. As a result of crystal growth experiments we obtained Li substituted and double Li and C substituted MgB_2 single crystals with dimensions up to 1.5x0.8x0.1 mm^3 (Fig. 1.8).

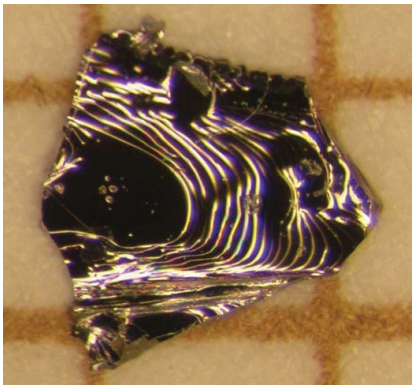

Figure 1.8: MgB_2 crystal grown in BN crucible. Scale is 1 mm.

Li and C contents have been determined from the single crystal X-ray refinement. The critical temperature and other superconducting properties of a two-band superconductor depend on the doping level and on the interband and intraband scattering and therefore, they can be modified by chemical substitutions. Doping with electrons, introduced by C or Al substitution, decreases T_c due to a shift of the Fermi level, and also due to additional scattering. T_c also decreases with Li hole doping, however the rate of this decrease is much lower than for C or Al substitutions. This reduction of T_c with both hole and electron doping indicates that MgB_2 is close to optimally doped. Because it can bring new information about the role of electronic band doping and of intra- and interband scattering, co-doping with holes and electrons is a very interesting issue. In the crystals where Li and C are substituted simultaneously one can expect compensation of the electron doping effect and an increase of T_c. However, the T_c reduction in co-doped crystals is a sum of T_c reduction of separate C and Li doping (Fig. 1.9). Holes introduced with Li cannot counterbalance electrons coming from C. The possible reason of it can be that holes coming from Li occupy the π band and do not compensate the electrons coming from C, which fill the σ band [2]. The total influence of co-doping on T_c of MgB_2 should be understood as a result of both electronic doping and impurity scattering.

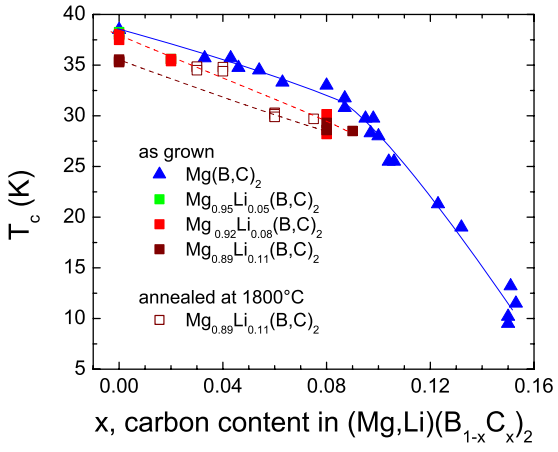

Figure 1.9: T_c dependence on substitution with C (triangles) or co-substitution with C and Li (reversed triangles, circles, and squares). Dashed lines show the same level of Li content for various levels of C substitution.

The electrical resistivity of substituted samples is systematically higher than in undoped samples. The most dominant change is associated with an increase of the residual resistivity, while the temperature-dependent part due to electro-phonon scattering remains essentially unmodified (within the experimental uncertainty). This indicates enhanced scattering due to defects introduced by substitutions including distortion of the lattice.

[1] V. Z. Turkevich et. al., Journal of Superhard Materials 25, 6 (2003)
[2] F. Bernardini and S. Massidda, Phys. Rev. B, 74, 014513 (2006).

1.8 Crystal growth and superconducting properties of $Ca_{2-x}Na_xCuO_2Cl_2$

N. D. Zhigadlo, S. Katrych, J. Karpinski

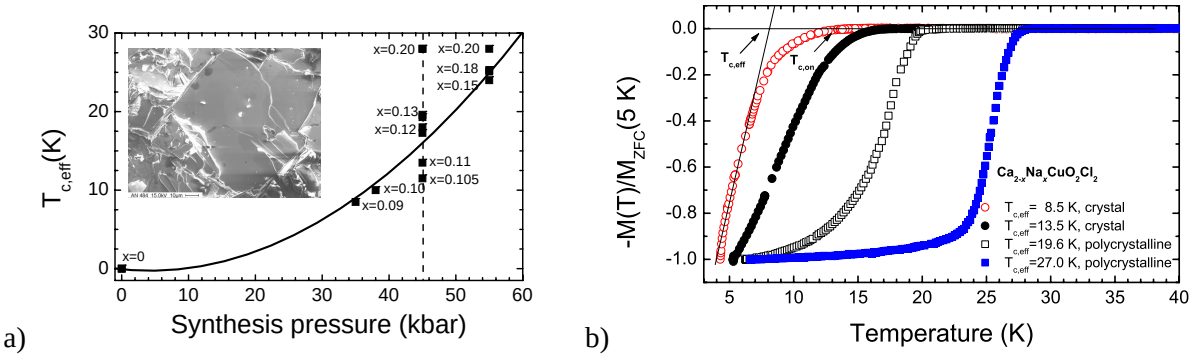

Figure 1.10: a) T_c as a function of synthesis pressure. For $p = 45$ kbar the variation of synthesis temperature leads to a systematic variation of the Ca/Na content. Inset: $Ca_{2-x}Na_xCuO_2Cl_2$ crystal grown under high-pressure. b) Normalized diamagnetic signal for a series of $Ca_{2-x}Na_xCuO_2Cl_2$ samples with various contents grown at high pressure.

$Ca_{2-x}Na_xCuO_2Cl_2$ is a structural analogue to the $La_{2-x}Sr_xCuO_4$ superconductor. By substituting Na^+ for Ca^{2+} mobile holes are introduced into the CuO_2 planes. The synthesis of the $Ca_{2-x}Na_xCuO_2Cl_2$ compounds is only possible under high pressure of several tens of kbar. High-pressure experiments have been performed in a cubic anvil cell and in an opposed anvil-type high-pressure cell. $Ca_{2-x}Na_xCuO_2Cl_2$ crystals have been grown by a flux method at 35–55 kbar and temperatures up to 1700 °C. Solidified blocks with crystallites of sizes up to 1x1mm^2 form under these conditions. The hole concentration has been tuned by Na substitution resulting in either insulating or superconducting compounds. A series of experiments at a synthesis pressure of 45 kbar and temperature of 1250-1700 °C shows formation of compounds from underdoped to optimally doped with a maximum T_c of 28 K and almost 100 % superconducting volume fraction. Applying a higher synthesis pressure (55 kbar) and temperature (up to 1700 °C) results in samples with x≈0.20 and a highest $T_{c,on}$ of 28.0 K. Our experiments show that the Na content depends not only on the synthesis pressure, as it was established before [1,2], but also on the reaction temperature and time (see vertical dash line in Fig. 1.10a). Figure. 1.10b) shows the normalized diamagnetic signal for a series of $Ca_{2-x}Na_xCuO_2Cl_2$ samples with various Na content. The T_c varies systematically with the Na content. Introducing holes by Na substitution is accompanied by an expansion of the unit cell along the crystallographic c-direction, and a contraction along the a axis.

[1] Z. Hiroi, N. Kobayashi, M. Takano, Nature (London) 371 (1994) 139.
[2] A. Azuma, et al., J. Low Temp. Phys., 13 (2003) 671.

1.9 Growth of β-pyrochlore $RbOs_2O_6$ single crystals. Superconducting properties of KOs_2O_6 and $RbOs_2O_6$

Z. Bukowski, N. D. Zhigadlo, M. Brühwiler, M. Tortello, J. Karpinski, B. Batlogg

Pyrochlore-structured osmate superconductors with T_c up to 9.5 K are a paricularly fascinating materials class due to the fact that the K and Rb ions occupy within the Os–O network a lattice site that is too large for the small K ions. The extremely non-harmonic potential experienced by K leads to a rattling of the K-ions and the coupling to the conduction electrons. Single crystals of superconducting β-pyrochlore RbOs2O6 with sizes up to 0.4 mm have been grown. Measurements of the electrical resistivity for the KOs_2O_6 and $RbOs_2O_6$ single crystals have been carried out at low temperatures and in high magnetic fields (Fig. 1.11). The temperature dependences of the upper critical field

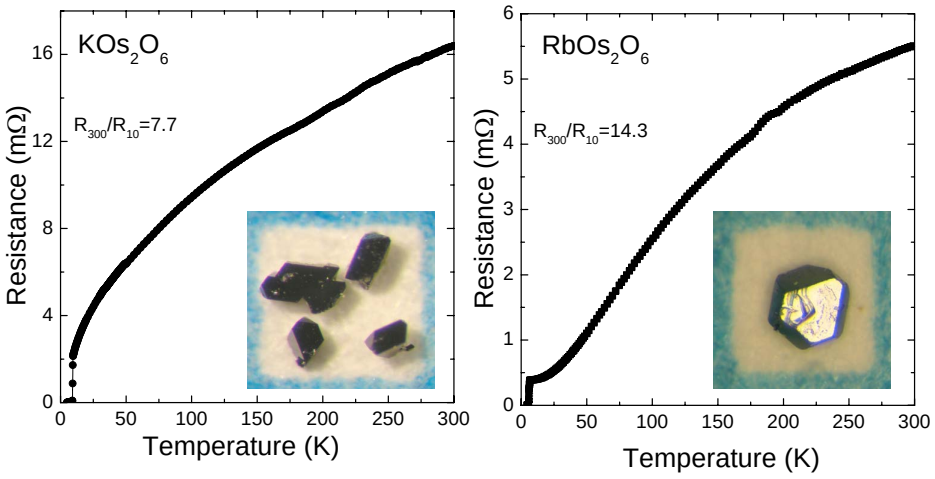

Figure 1.11: The temperature dependence of the electrical resistance for the KOs_2O_6 and $RbOs_2O_6$ single crystals with the β-pyrochlore structure.

H_{c2} for KOs_2O_6 and $RbOs_2O_6$ were determined from the resistivity data. In agreement with results on polycrystalline samples and with H_{c2} results from heat capacity measurements, the variation of the upper critical field near T_c in the various compounds shows these osmate superconductors to be in the clean limit.

1.10 Novel pyrochlore compounds using high-pressure high-temperature synthesis

Z. Bukowski, N. D. Zhigadlo, M. Brühwiler, M. Tortello, A. V. Mironov, S. Katrych, J. Karpinski, B. Batlogg

High pressure synthesis is highly effective in preparation of pyrochlore-type compounds [1]. This motivated us to use high-pressure and high-temperature techniques in a search for other pyrochlore compounds in related systems. The syntheses were carried out in a cubic anvil apparatus at 30 kbar in the temperature range of 800-1100 °C. Previously, we reported on the high-pressure synthesis of sodium osmate $Na_{1.6}Os_2O_{6.6}$ with the α-pyrochlore structure. Heat capacity measurements (Fig. 1.12) show an enhanced value of the Sommerfeld coefficient (γ=21 mJ/mol K^2), roughly half of the value observed for the superconducting β-pyrochlore $RbOs_2O_6$ [2].

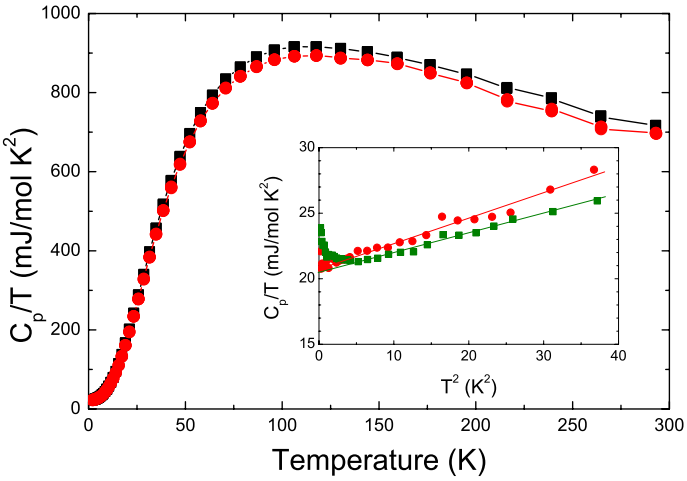

Figure 1.12: Heat capacity for α-pyrochlore $Na_{1.6}Os_2O_{6.6}$.

The magnetic susceptibility of this compound is temperature independent indicative of Pauli paramagnetism due to itinerant electrons. The absolute value of the electrical resistivity is relatively low but in contrast to typical metals, it is almost temperature independent for the as-grown crystals (Fig. 1.13). After annealing at 200 °C $\rho(T)$ is more typical for a metal which suggests that water is incorporated in the as grown crystals. Using high pressure synthesis we have obtained α-pyrochlore $Cd_2Os_2O_7$ which is reported to show metal-to-insulator transition at 225 K [3]. Our attempt to prepare strontium osmate under high pressure resulted in a novel compound $Sr_3Os_4O_{14}$. We have determined its crystal structure as tetragonal, isostructural to $Pb_3Nb_4O_{12}F_2$ [4] with lattice parameters a=12.2909(8) Å, and c=7.2478(5) Å. The structure analysis suggests P42nm or P42/mnm as a possible space group.

In general, the structure may be regarded as the pyrochlore-type. This compound is metallic (see Fig. 1.14a) and exhibits temperature independent paramagnetism. Heat capacity measurements (Fig. 1.14b) revealed a slightly enhanced value of the Sommerfeld coefficient γ=34 mJ/molOs K^2. Superconductivity has not been observed down to 2 K. The high-pressure synthesis of lithium osmate resulted in a novel compound $LiOsO_3$. This phase crystallizes in a rhombohedral structure and presumably is isostructural to $LiReO_3$. In an attempt to substitute Ca by Na in $Ca_2Ru_2O_7$ a novel cubic $Ca_{1-x}Na_xRuO_3$ has been synthesized under high pressure.

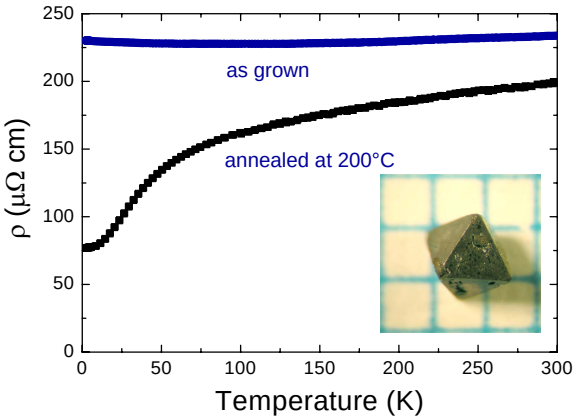

Figure 1.13: Resistivity as a function of temperature for the single crystal of α-pyrochlore $Na_{1.6}Os_2O_{6.6}$. Inset: Single crystal grown at 30 kbar.

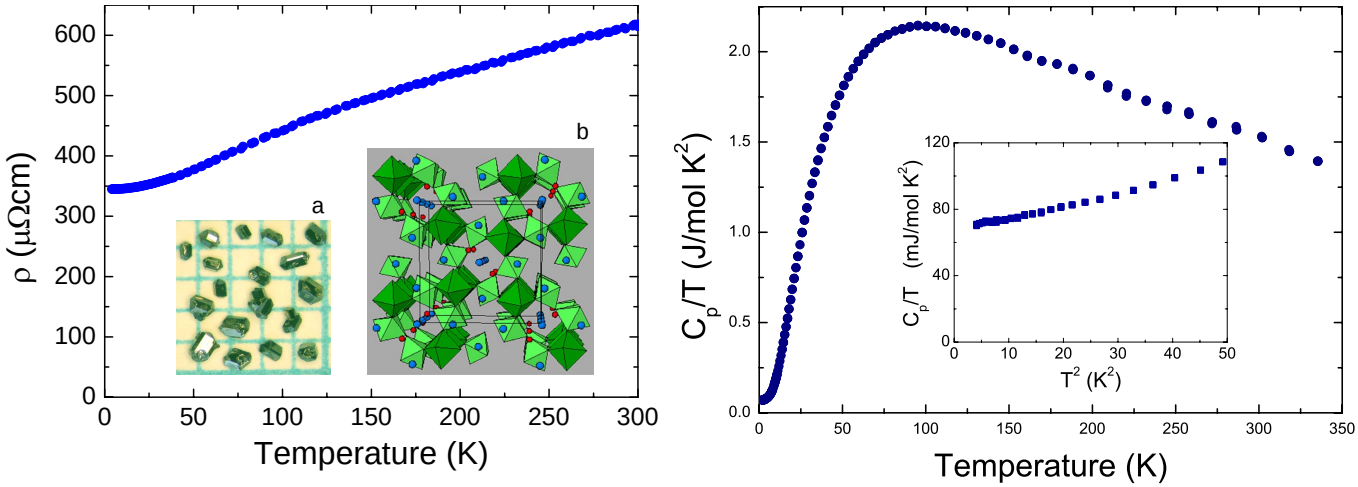

Figure 1.14: Left panel: Temperature dependence of resistivity for $Sr_3Os_4O_{14}$. Insets: (a) Single crystals of $Sr_3Os_4O_{14}$ grown at 30 kbar. (b) Crystal structure of $Sr_3Os_4O_{14}$ (view along [001] direction). Right panel: Heat capacity for $Sr_3Os_4O_{14}$.

[1] M. A. Subramanian et al., Prog. Solid State Chem., 15 (1983) 55.
[2] M. Brühwiler et al., Phys. Rev. B, 73 (2006) 094518.
[3] A. W. Sleight et al., Solid State Commun., 14, 357 (1974).
[4] Ö. Sävborg, M. Lundberg, J. Solid State Chemistry, 57 (1985) 135.

1.11 Low-temperature ion exchange in the pyrochlore compounds

Z. Bukowski, N. D. Zhigadlo, J. Karpinski

The pyrochlore structure (AB_2O_6 or $A_2B_2O_7$)contains tunnels surrounded by six BO_6 octahedra. These tunnels intersect in a three-dimensional manner. The mobility of ions in the tunnels are expected to be strongly dependent on the relative size of the ion and the tunnel. The sodium or potassium ions in the pyrochlore structure are readily exchanged by most other monovalent cations. This low temperature ion exchange allows the formation of novel, often metastable, compounds that cannot be synthesized by conventional high-temperature solid-state reactions. The ionic exchange experiments were carried out in reaction of the sodium or potassium pyrochlore powder with an excess of metal nitrates in air at 175-300 °C or with 1M HNO_3 at 80 °C. We have observed that Na^+ ions in α-pyrochlore

$Na_{1.6}Os_2O_{6.6}$ can be easily exchanged for K^+, Ag^+ or H^+. Similarly, K^+ in β-pyrochlore KOs_2O_6 can be exchanged for Na^+, and Ag^+. It is interesting to note that when Na^+ ions are exchanged for K^+ in $Na_{1.6}Os_2O_{6.6}$ the α-pyrochlore structure transforms into the β-pyrochlore one and the product becomes superconducting and vice versa, when K^+ ions in superconducting β-pyrochlore KOs_2O_6 are exchanged for Na^+, nonsuperconducting α-pyrochlore is formed. The exchange of Na^+ or K^+ ions for Ag^+ results in the formation of the α-pyrochlore $Ag_xOs_2O_{6+d}$ (nonsuperconducting). Since the ionic radius of Ag^+ is larger than that of Na^+, but smaller than that of K^+, we may conclude that for the pyrochlore osmates K^+ is the smallest cation which can occupy the 8b sites in the β-pyrochlore structure. All smaller cations occupy 16d sites and the α-pyrochlore structure is formed. We have found that Na^+ ions can be also exchanged for Sr^{2+} cations but this process is very slow and requires a long time (3 weeks).

1.12 Pressure dependence of the charge-density-wave gap in rare-earth tri-tellurides

A. Sacchetti, M. Lavagnini, and L. Degiorgi

work in collaboration with N. Ru and I.R. Fisher, Stanford University, California

The physical properties of low-dimensional systems have fascinated researchers for a great part of the last century, and have recently become one of the primary centers of interest in condensed matter research. Low-dimensional systems not only experience strong quantum and thermal fluctuations, but also admit ordering tendencies which are difficult to realize in three-dimensional materials. Prominent examples are spin- and charge-density waves in quasi-one-dimensional compounds. Moreover, the competition among several possible order parameters leads to rich phase diagrams, which can be tuned by external variables as temperature, magnetic field, and both chemical and applied pressure. Tunable external parameters also affect the effective dimensionality of the interacting electron gas and thus the intrinsic electronic properties of the investigated systems.

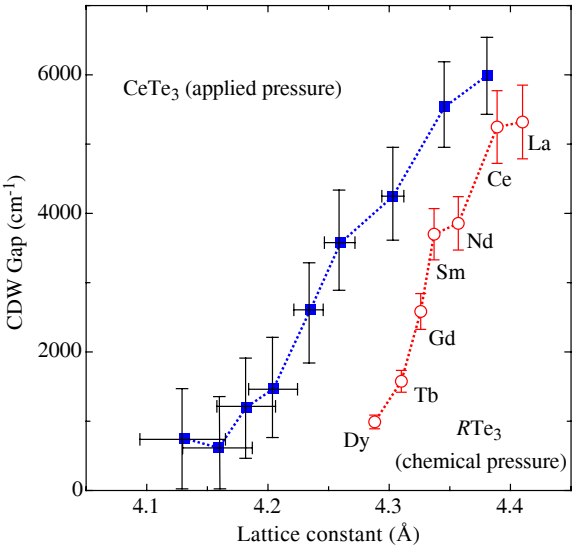

Figure 1.15: CDW gap as a function of the lattice constant a for $CeTe_3$ under applied pressures and for the RTe_3 series. Dotted lines are guides to the eye.

The rare-earth tri-tellurides RTe_3 (R= La-Tm, excepting Eu) are the latest paramount examples of low dimensional systems exhibiting the formation of an incommensurate charge-density-wave (CDW) state. The average crystal structure is layered and weakly orthorhombic, consisting of double layers of nominally square-planar Te sheets, separated by corrugated RTe slabs. The lattice constant decreases on going from R = La to R = Tm, i.e. by chemically compressing the lattice, as consequence of the reduced ionic radius of the rare-earth atom. The physical properties in RTe_3 can be then investigated as a function of the in-plane lattice constant a, which is directly related to the Te-Te distance in the Te-layers. Therefore, the motivation of our work originates from the fact that RTe_3 generally provides an adequate playground to study the effect of chemical pressure and externally applied pressure in shaping the predisposition of these materials to undergo a CDW phase transition.

We first have reported on the optical measurements of RTe_3. Our data, collected over an extremely broad spectral range, allowed us to observe both the Drude component and the single-particle peak, ascribed to the contributions due to the free charge carriers and to the excitation across the charge-density-wave gap, respectively. On decreasing a, a reduction of the CDW gap together with an enhancement of the metallic (Drude) contribution were observed in the absorption spectrum.

We have then presented infrared optical investigations of the pressure dependence of the optical reflectivity on $CeTe_3$ at 300 K, i.e., below the CDW transition temperature. We demonstrate that one can tune (in this case gradually suppress) the charge density wave gap by reducing the lattice parameter upon application of pressure. Such control

of the CDW gap is similar to that caused by chemical means, when compressing the lattice by substituting large with small ionic radius rare-earth elements (i.e., by reducing a).

Therefore, we have established the equivalence of chemical and applied pressure in governing the onset of the CDW broken symmetry ground state (see Fig. 1.15). This is especially interesting because the present results emphasize that the suppression of the CDW gap is not a result of disorder (which necessarily comes into play as a result of chemical substitution), but clearly arises from internal changes of the effective dimensionality of the electronic structure. This strengthens the arguments regarding the link between CDWs and nesting of the Fermi surface in low dimensional materials. We propose that the broadening of the bands upon lattice compression in the layered rare earth tri-tellurides removes the perfect nesting condition of the Fermi surface and therefore diminishes the impact of the CDW transition on the electronic properties of $R\mathrm{Te}_3$.

The formation of the CDW state in the $R\mathrm{Te}_3$ series was also found to be an indication for a hidden one-dimensional behavior in these quasi two-dimensional compounds. Our work at ambient pressure shows the development of characteristic power law behaviour in the high frequency tail of the optical conductivity. The latter investigation of CeTe_3 under applied external pressure, on the other hand, does not address to which extent the applied pressure might influence the effect of electron-electron interactions and Umklapp processes, as suggested in our experiment at zero pressure over the rare-earth series, as well as the dimensionality crossover, in driving the CDW transition. This awaits for further experimental effort, allowing the extension of the measured spectral range under pressure up to higher as well as to lower energies than the energy window presented here. This could open new perspectives to a comprehensive study about the pressure dependence of the characteristic power law behavior, seen in the absorption spectrum of the $R\mathrm{Te}_3$ series, and more generally about the influence of pressure in the formation of the Luttinger liquid state in quasi one-dimensional systems.

Chapter 2

Nanophysics

(http://www.nanophys.ethz.ch)

Head
Prof. Dr. K. Ensslin
Prof. Dr. R. Monnier

Academic Staff

Dr. C. Ellenberger	Dr. S. Kicin	E. Ruh
A. Gildemeister	Y. Komijani	Dr. I. Shorubalko
D. Graf	Dr. R. Leturcq	Dr. M. Sigrist
B. Grbic	L. Meier	U. Szerer
S. Gustavsson	F. Molitor	
M. Hüfner	T. Müller	
PD Dr. T. Ihn	A. Pfund	

Technical Staff

C. Barengo	P. Studerus

Administrative Staff
B. Abt

Academic Guests
Prof. Yigal Meir, Ben-Gurion University, Israel, 16.-17.3.2006
Mira Bartosik, Brno University of Technology, Czech Republic, 7.-18.8.2006
Dr. V. I. Tokar, Institute of Magnetism, National Academy of Sciences, Kiev, Ukraine, 1.4. - 31. 7. 2006

Doctoral theses
Christoph Ellenberger
Electron transport through nanostructures on parabolic quantum wells
25.8.2006

Diploma theses
Romeo Bianchetti
Magnetic field symmetries of quantum rings in the nonlinear transport regime
WS 2005/06

Hannes Erntell
Fabrication and charaterization of nanoscale SrTiO3 memory cells
WS 2005/06 (work done at IBM Rueschlikon)

Thomas Müller
A radio frequency quantum point contact detecting electrons on submicrosecond timescales
WS 2005/06

Fabio Torriani
Characterization of cantilever tuning fork sensors for atomic force microscopy
WS 2005/06

Francoise Molitor
Raman spectroscopy and transport experiments on few-layer graphene flakes
SS 2006

Christian Roth
Non-linear transport effects in an Aharonov-Bohm ring
SS 2006

Sophie Schönenberger
Electrical Characterization of Silicon-Nanowires
SS 2006 (work done at IBM Rüschlikon)

Kilian Vollenweider
Radio frequency measurements with a quantum point contact
SS 2006

2.1 Shot noise of single electron transport in quantum dots

S. Gustavsson, R. Leturcq, B. Simovic, R. Schleser, T. Ihn, P. Studerus, and K. Ensslin, in collaboration with D. C. Driscoll and A. C. Gossard, University of California, Santa Barbara, USA

Current fluctuations in conductors have been extensively studied because they provide additional information compared to the average current, in particular, for interacting systems. Shot noise measurements demonstrated the charge of quasiparticles in the fractional quantum Hall effect and in superconductors. However, to perform such measurements for semiconductor quantum dots (QDs) using conventional noise measurements techniques is very challenging. This is because of the very low currents and the corresponding low noise levels in these systems.

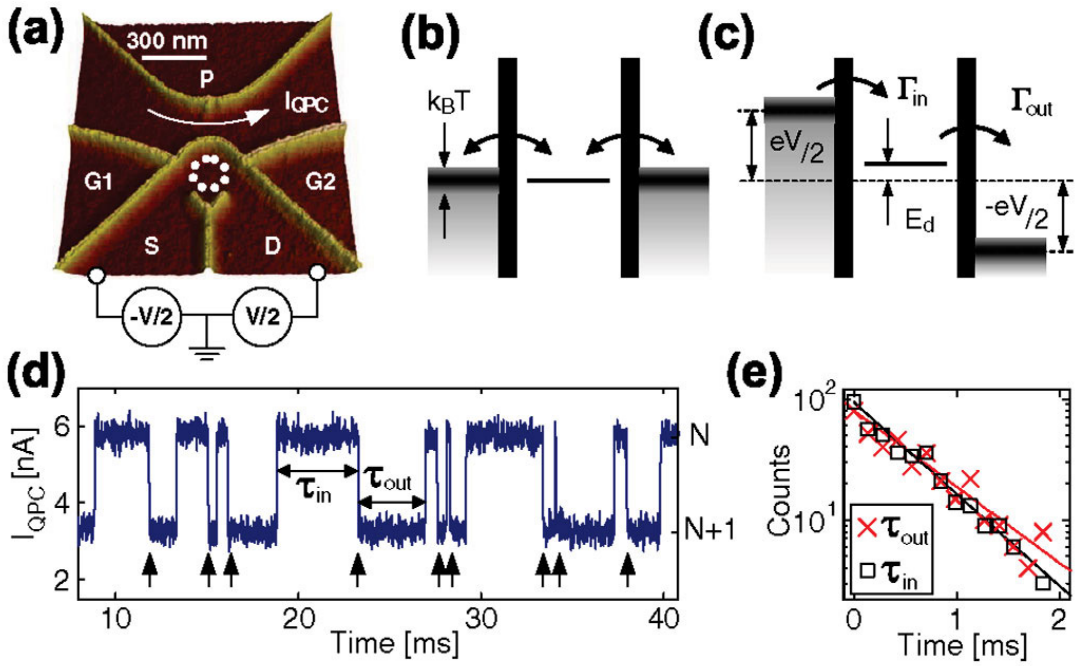

Figure 2.1: (a) AFM micrograph of the sample consisting of a QD connected to two contacts S and D and a nearby QPC. G1, G2, and P are lateral gates allowing the tuning of the tunnel coupling to the source S, the coupling to the drain D, and the conductance of the QPC. G1 and G2 are also used to tune the number of electrons in the QD. A symmetric bias voltage V is applied between the source and the drain on the QD. (b),(c) Scheme of the quantum dot in the case of equilibrium charge fluctuations (b) and nonequilibrium charge fluctuations (c). (d) Time trace of the current measured through the QPC corresponding to fluctuations of the charge of the dot between N and N+1 electrons. The arrows indicate transitions where an electron is entering the QD from the source lead. (e) Probability density of the times in and out obtained from time traces similar to the one in (d). The lines correspond to the expected exponential dependence.

We report on the real-time detection of single electron tunneling through a QD using a quantum point contact (QPC) as a charge detector. With this method, we can directly measure the distribution function of current fluctuations in the QD by counting electrons.

Figure 2.1 (a) shows the structure, fabricated on a GaAs- GaAlAs heterostructure containing a two-dimensional electron gas 34 nm below the surface. An atomic force microscope (AFM) was used to locally oxidize the surface, thereby defining depleted regions below the oxide lines. In order to measure the current with a charge detector, one has to avoid that electrons travel back and forth between the dot and one lead or to the other lead due to thermal fluctuations [Fig. 2.1(b)]. This is achieved by applying a large bias voltage between source and drain, such that the potential drop across the dot is larger than the thermal energy kT, see Fig. 2.1(c).

An example of a time trace of the QPC current in this configuration is shown in Fig. 2.1(d). The number of electrons in the QD fluctuates between N and N+1. Since this trace corresponds to the non-equilibrium regime, we can attribute each transition N to N+1 to an electron entering the QD from the source contact, and each transition N+1 to N to an electron leaving the QD to the drain contact. The charge fluctuations in the QD correspond to a non-equilibrium

process and are directly related to the current through the dot. Because of the Coulomb blockade, only one electron at a time can enter the QD, which allows one to count electrons traveling through the system.

The first application of electron counting in the nonequilibrium regime concerns the determination of the individual tunneling rates from the source to the quantum dot and from the quantum dot to the drain. In the trace of Fig. 2.1(d), the time τ_{in} corresponds to the time it takes for an electron to enter the quantum dot from the source contact, and τ_{out} to the time it takes for the electron to leave the quantum dot to the drain contact. It is interesting to note that, in the case shown in Fig. 2.1(e), the QD is almost symmetrically coupled. We demonstrate here a very sensitive method to determine the symmetry of the coupling.

An alternative way to investigate current fluctuations, introduced by Levitov et al., is known as full counting statistics (FCS). This method relies on the evaluation of the probability distribution function of the number of electrons transferred through a conductor within a given time period. In addition to the current and the shot noise, which are the first and second moments of this distribution, this method gives access to higher order moments.

The most intuitive method for measuring the FCS of electron transport is to count electrons passing one by one through the conductor. It is a challenging task since it requires a very sensitive, low-noise, and noninvasive electrometer, as well as a high-bandwidth circuit.

To our knowledge, this is the first measurement of the full counting statistics for electrons in a solid state device. In addition, we can tune the coupling of the QD with both leads and measure the respective tunneling rates. We show experimentally the suppression of the second and third moments of the current fluctuations when the QD is symmetrically coupled to the leads.

2.2 Magnetic field symmetry and phase rigidity of the nonlinear conductance in a ring

R. Leturcq, G. Götz, T. Ihn, and K. Ensslin, in collaboration with D. Sanchez, Universitat de les Illes Balears, Mallorca, Spain, and D. C. Driscoll and A. C. Gossard, University of California, Santa Barbara, USA

A mesoscopic ring can be used as an electron interferometer in order to compare the electronic phase of electrons traveling through both arms of the ring using the Aharonov-Bohm (AB) effect. However, it has been shown that a two-terminal ring does not allow us to measure directly this phase difference in the linear transport: The two-terminal conductance shows AB oscillations with a phase constrained to 0 or π. This phase rigidity is a consequence of microreversibility, showing that the linear conductance of a two-terminal system must be symmetric in the magnetic field. While the Onsager-Casimir relations hold close to equilibrium (linear conductance), there is no fundamental reason why far from equilibrium the nonlinear conductance should still follow this symmetry; i.e., one could expect $G(V,B) \neq G(V,-B)$. It is then natural to ask whether the phase rigidity would still hold for the nonlinear transport in a two-terminal ring.

The two-terminal ring geometry has been fabricated on a GaAs=GaAlAs heterostructure containing a two-dimensional electron gas (2DEG) 34 nm below the surface. The I-V curves show a clear nonlinear behavior at voltages above about 100 μV. Furthermore, they demonstrate that the conductance is not exactly equal for opposite magnetic fields. In order to quantify the nonlinear behavior, the $I-V$ curve is fitted with a fifth order polynomial, allowing a voltage offset V_0 :

$$I = \sum_{n=1}^{5} G^{\{n\}}(V - V_0)^n. \tag{2.1}$$

Here $G^{\{n\}}$ and V_0 are fitting parameters. In this decomposition, the odd coefficients ($G^{\{1\}}$, $G^{\{3\}}$,...) correspond to the voltage-symmetric part of the differential conductance $G(V,B) = dI/dV$, and the even coefficients ($G^{\{2\}}$, $G^{\{4\}}$,...) to the voltage-antisymmetric part of $G(V,B)$.

The fitting parameters are shown as a function of magnetic field in Fig. 2.2 for fixed gate voltages. In each panel, the dashed line corresponds to the same curve as the plain line, but mirrored horizontally at $B = 0$ in order to check the magnetic field symmetry. All conductances show AB oscillations as a function of magnetic field, with a period close to 75 mT. This period corresponds to a diameter of the ring of 260 nm, compatible with the lithographic size of the ring. In addition to h/e oscillations, the odd coefficients show strong $h/2e$ oscillations. It is interesting to note that the even coefficients do not show any significant $h/2e$ oscillations.

It is clear from the uppermost panel that the linear conductance $G^{\{1\}}$ is symmetric in magnetic field. The higher order coefficients show a remarkable behavior. While the odd coefficients are symmetric in magnetic field within experimental errors, the even coefficients are not symmetric in magnetic field.

While electron heating could explain both the origin and the symmetry of the odd coefficients, it cannot explain the even ones, since the temperature should depend on the electric power. We have checked that nonlinearities on the QPCs depend only weakly on the magnetic field.

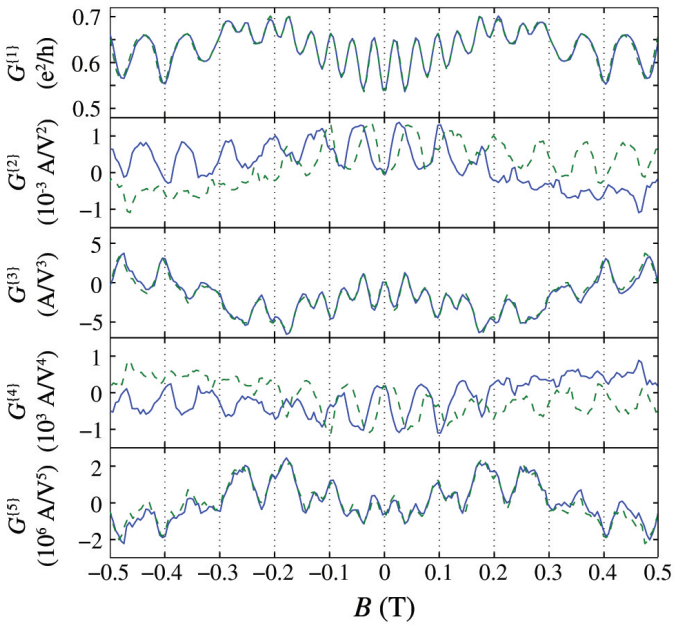

Figure 2.2: Magnetic field dependence of the nonlinear conductance coefficients $G^{\{n\}}$, for $V_{PG2} = V_{PG3} = 0$ and $V_{PG1} = -0.050$ V. The dashed curves correspond to the inversion of the plain curves compared to $B = 0$.

The scattering theory for nonlinear mesoscopic transport establishes that the current,

$$I = \frac{2e}{h} \int dE\, T(E;U)[f(E - eV/2) - f(E + eV/2)]\,, \tag{2.2}$$

depends on the transmission T, which is a functional of the screening potential U in the mesoscopic conductor. For simplicity, we assume that U is uniform though the full theory takes into account the spatial distribution. In Eq. (2.2), $f(x) = 1/(1 + \exp{(x - E_F)/k_BT})$ with E_F the Fermi energy. Within the Fermi-Thomas approximation, the induced charge density is a linear function of the external bias V. Assuming that the density of states is weakly energy dependent, charge conservation demands that $U(V) = U_{\rm eq} + uV$, where the characteristic potential $u = (\partial U/\partial V)_{\rm eq}$ relates the change in the screening due to a voltage shift. Such response is, in general, asymmetric under B reversal. We emphasize that this effect arises in the nonlinear regime only since microreversibility requires $U_{\rm eq}(B) = U_{\rm eq}(-B)$ at equilibrium.

Inserting $U(V)$ in Eq. (2.2) and expanding in powers of V, we find at zero temperature:

$$G^{\{n\}} = \frac{1}{2^{n-2}n!} \frac{e^{n+1}}{h} T^{(n-1)}(E_F)[\delta_{n,\rm odd} - 2u\delta_{n,\rm even}]\,. \tag{2.3}$$

Clearly, since the transmission and its energy derivatives $T^{(n)}$ are B-symmetric, only the even coefficients are asymmetric under B reversal. The internal potential depends on the phase accumulated along both arms, which can be tuned with gate voltages, thus affecting the magnetic field asymmetry. This asymmetry arises when the conductor is asymmetrically coupled to the leads.

We show that the voltage-symmetric part of the conductance is symmetric in magnetic field, while the voltage-antisymmetric part is asymmetric in magnetic field, compatible with the scattering theory for nonlinear transport. Furthermore we can tune the phase of the asymmetry by changing the voltage of gates placed nearby the ring, which shows that the nonlinear conductance is not phase-rigid in contrast to the linear conductance.

2.3 Excitation spectrum of two correlated electrons in a lateral quantum dot with negligible Zeeman splitting

C. Ellenberger, T. Ihn, K. Ensslin, in collaboration with C. Yannouleas and U. Landman, Georgia Instititute of Technology, USA, and D. C. Driscoll and A. C. Gossard, University of California, Santa Barbara, USA

Two-electron (2e) systems (e.g., the He atom and the H_2 molecule) have played an important role in the development of the theory of many-body effects in quantum mechanics and the understanding of the chemical bond. Recently, two-dimensional (2D) man-made quantum dots (QDs), fabricated in semiconductor materials, have attracted attention as a laboratory for investigations of few-body systems with highly controlled parameters such as the electron number, confinement strength, interelectron repulsion, and the influence of an applied magnetic field (B). Furthermore, 2e QDs may be used for implementing logic gates in quantum computing, or, as suggested recently, by using 2e singlet and triplet states as the two states of a qubit; here the 2e populate a single QD.

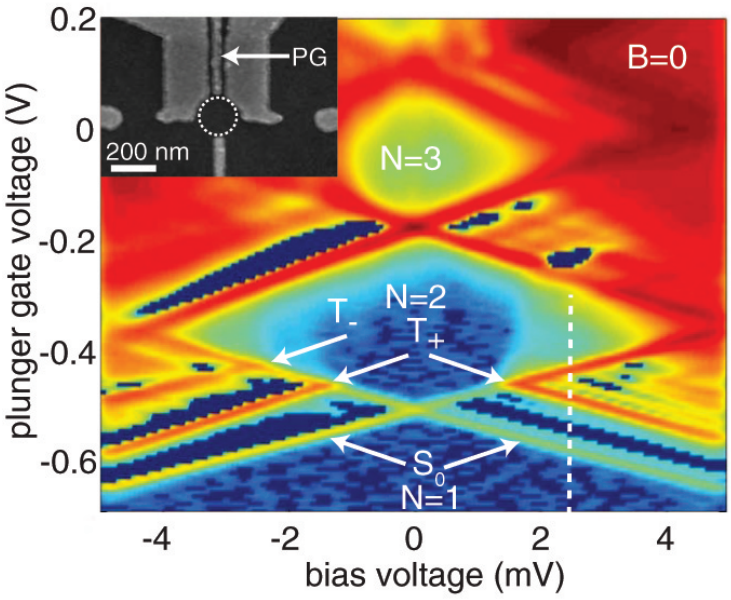

Figure 2.3: Differential conductance dI/dV_{bias} at zero magnetic field. Electron numbers N are indicated in the diamonds. The arrows mark the transitions between the one electron ground state and the 2e spin-singlet (S0) and spin-triplet states (T). Inset: scanning electron micrograph of the sample. The quantum dot is marked with a dotted circle and PG labels the plunger gate.

The sample is based on a 55 nm wide Ga Al As parabolic quantum well with the center located 75 nm below the surface. The parabola ranges from 6% Al concentration in the center to 23% at the edges. It was designed for having a g factor for electrons $\|g\| \approx 0$ following from the average material composition. The quantum dot (geometric diameter 220 nm) with integrated charge readout depicted in Fig. 2.3 (inset) was defined using electron beam lithography patterned split gates. All measurements were performed at an electronic temperature below 300 mK as estimated from the width of conductance resonances in the Coulomb-blockade regime.

Figure 2.3 shows the differential conductance of the QD in the plane of bias and plunger-gate voltages. The resulting diamond pattern of suppressed conductance corresponds to fixed electron numbers N in the dot as indicated in the figure. The values for the electron numbers were found by depleting the dot down to zero electrons with more negative gate voltages and by using the quantum point contact near the quantum dot as a charge detector. Strong lines parallel to the diamond boundaries outside the diamonds correspond to excited states of the level spectrum. This allows to measure the singlet-triplet splitting as a function of magnetic field. A quantitative understanding of the measured excitation spectrum and of the underlying strong correlations in the 2e QD were obtained through exact diagonalization of the Hamiltonian for two 2D interacting electrons.

We emphasize that the negligible Zeeman splitting in our sample is crucial for the observation of this trend which should even lead to singlet-triplet oscillations of the ground state spins at higher magnetic fields. Experimentally, however, the accessible magnetic-field range is limited, because conductance resonances disappear with increasing field due to wave function shrinkage, and counterbalancing this effect by changing gate voltages would seriously change the confinement potential.

The excitation spectra of a lateral 2e QD with negligible Zeeman splitting, moderate anisotropy, and parabolic z confinement have been investigated. Exact-diagonalization calculations, including a rather small (14%) decrease in the effective interelectron Coulomb repulsion, explain in detail the observed features of the spectra under the influence of a variable magnetic field, including the variation of the singlet-triplet splitting, J. The theoretical analysis of the salient excitation spectra patterns (e.g., avoided level crossings, the line shape of J(B), and the lifting of level degeneracies in

comparison to the circular case) indicates significant electronic correlations associated with the formation of a Wigner molecule.

2.4 Coherent probing of excited quantum dot states in an interferometer

M. Sigrist, T. Ihn, and K. Ensslin, in collaboration with M. Reinwald and W. Wegscheider, University of Regensburg, Germany

Quantum coherence and inelastic processes are valuable concepts for the understanding of quantum systems and the limitations for their manipulation. These topics can be studied by embedding semiconductor quantum dots (QDs) in interfering paths of electronic Aharonov- Bohm (AB) interferometers. If an electron traverses the N-electron dot elastically, but nonresonantly via an $N \pm 1$-electron virtual state (cotunneling), the resulting current still has a coherent contribution. At finite bias voltages inelastic processes are possible in which the tunneling electron loses energy by exciting the QD. These processes lead to incoherent contributions if the QD excitation allows which-path detection in the interferometer.

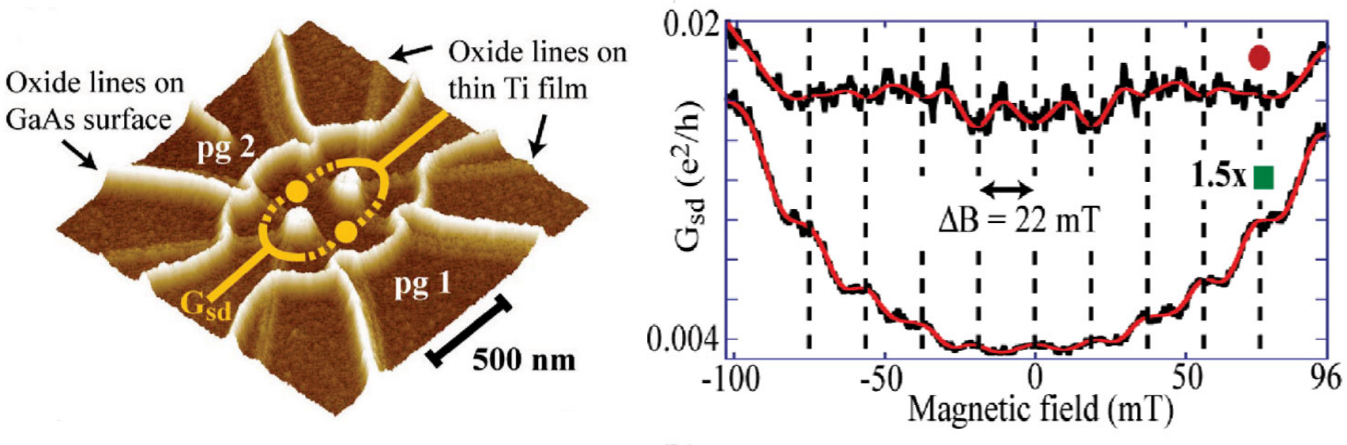

Figure 2.4: Left: SFM micrograph of the structure. Right: Magnetic field dependence of the differential conductance for gate voltages below (lower curve) and above (upper curve) the inelastic onset

The sample shown in Fig. 2.4 is based on a Ga[Al]As heterostructure with a two-dimensional electron gas (2DEG) 34 nm below the surface. It was fabricated by multiple-layer local oxidation with a scanning force microscope : the 2DEG is depleted below the oxide lines written on the GaAs surface [bright lines in Fig. 2.4] thus defining the ring interferometer. A Ti film evaporated on top is cut by local oxidation [faint lines in Fig. 2.4] into mutually isolated top gates. A QD is embedded in each arm of the resulting AB interferometer as indicated by the dots in Fig. 2.4. Direct tunneling between the two dots is suppressed by applying a negative voltage between the 2DEG and the metallic top gate.

With the dots strongly coupled to the ring (open regime) and applying a magnetic field, B, normal to the 2DEG plane, we observe a periodically modulated conductance with an AB period of 22 mT, consistent with one magnetic flux quantum $\Phi_0 = h/e$ penetrating the area enclosed by the paths indicated in Fig. 2.4.

The dots are tuned into the Coulomb blockade regime where transport occurs via cotunneling events. We have measured the source-drain conductance G_{sd} as a function of B. The lower trace in Fig. 2.4 corresponds to low dc bias voltage smaller than the level separation where elastic cotunneling is the dominant transport mechanism. AB oscillations with a maximum at zero B and a period of 22 mT are observed confirming a phase-coherent contribution to the elastic cotunneling current. The upper trace in Fig. 2.4 taken at higher dc bias voltage involves inelastic cotunneling through one of the dots. Also in this case AB oscillations are observed, but show a minimum at B=0. It is evident from the data that the participation of the inelastic cotunneling process does not hamper the occurrence of

quantum interference. We emphasize that G_{sd} does not detect the total (energy integrated) dc current, but only a small (compared to temperature) energy window around the chemical potentials in source and drain.

We have shown that the measurement of the coherent contribution to the cotunneling current in an Aharonov-Bohm interference experiment can be used to detect coherent elastic cotunneling processes on a background of other inelastic processes. This coherent current contribution contains qualitative information about the occupation probability of the involved excited dot state and ratios of transport and relaxation rates. The results give a new perspective on inelastic cotunneling onsets. The measurement technique can be employed for further studies of coherent tunneling and interference involving quantum dots.

2.5 Gate tunability of stray-field-induced electron spin precession in a GaAs/ InGaAs quantum well below an interdigitated magnetized Fe grating

L. Meier, G. Salis (IBM Rüschlikon), C. Ellenberger, E. Gini (FIRST lab), and K. Ensslin

Considerable effort has been devoted to gaining coherent control over single electron spins in semiconductors, motivated by the potentially long coherence times that make such a two-level system an ideal candidate for a quantum bit.

Our sample consists of a 40 nm thick InGaAs QW 8.8 $\%$ In, sandwiched between the GaAs substrate and a 20 nm GaAs cap layer. Both well and cap are n doped with Si to ensure long spin lifetimes, the latter with a delta-doping in the middle of the layer, the former with a bulk doping. On the surface, arrays of 80 nm thick Fe Au bars have been evaporated using electron-beam lithography and standard lift-off processes with a 10 nm Ti adhesion layer between the Fe (Au) and the GaAs surface. The Fe bars were protected from oxidation by 10 nm Al. Neighboring bars have separate electrical connections, so that they can be put on different potentials. We have fabricated interdigitated gratings 100 μm x 100 μm in size having periods p of 1, 2, and 4 μm and a bar width of half the period.

We use time-resolved Faraday rotation (TRFR) to trace the electron spin precession in the QW: a circularly polarized picosecond pump pulse from a Ti:Sapphire laser tuned to the absorption edge of the QW and focused on the grating creates spin-polarized electrons in the conduction band of the QW. The polarization axis of the linearly polarized probe pulse, focused on the same spot, which arrives with a time delay on the sample, is rotated by an angle proportional to the projection of the spin polarization on the laser beam axis perpendicularly to the QW . When an external magnetic field is applied in-plane with the QW and perpendicular to the bars, the electron spins precess about the magnetic field axis.

A numerical simulation of the magnetic stray field obtained is shown in the top of Fig. 2.5. The stray field in the center of the QW is expected to be 200 mT close to a Fe bar and 50 mT in the middle of the gap. The x component, which our measurement geometry is most sensitive to, changes sign at the edge of a bar. It is parallel to Bext between the bars and antiparallel below a bar. The lower part of Fig. 2.5 shows for different voltages applied between neighboring stripes the dependence of the precession frequency ν on Bext with a linear background subtracted. While on the sample with the Au grating $\nu - \nu_0$ is constant in Bext, $\nu - \nu_0$ on the Fe sample increases linearly up to Bext $\approx$ 0.3 T. For Bext below 0.3 T, $\nu - \nu_0$ remains constant at about 0.05 GHz, corresponding to an average stray field of 7 mT. Magneto-optical Kerr measurements confirm that at this external field, the magnetization of the Fe grating and with it the stray field saturates.

We have observed a tunability of the electron spin precession below a magnetized Fe grating. By applying a gate voltage to an interdigitated grating, we are able to tune the electron spin precession frequency by 0.5 GHz/V, corresponding to an effective magnetic stray field of about 70 mT/V. Modulating the gate potential with a frequency of 1.44 GHz enables the electron spin precession to be controlled on a nanosecond timescale. This could be useful for further experiments that address electron spin resonance using magnetic stray fields.

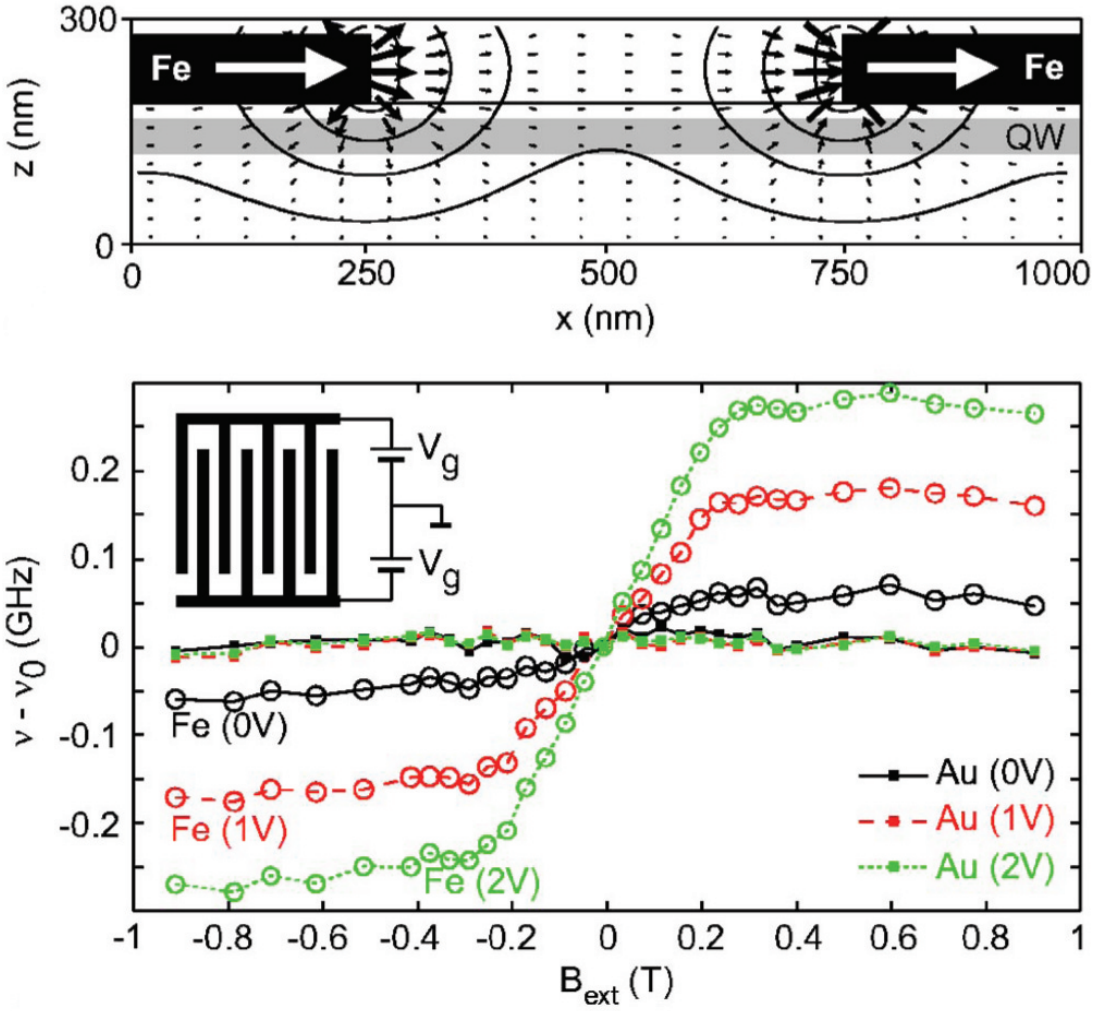

Figure 2.5: Top: Micromagnetic simulation of the magnetic stray field of a grating with period 1 μm. The solid lines of constant field indicate magnetic fields of 500, 200, 100, and 50 mT. The QW is shaded gray. Bottom: Electron precession frequency in the QW below the 1 um grating for different gate voltages. A linear fit $\nu_0 = g\mu_B B_e xt$ to the data has been subtracted (for Fe the fit only included the saturated region $|B_{ext}| > 0.3$ T). Inset: sketch of a gated interdigitated grating.

2.6 Classical Hall effect in scanning gate experiments

A. Baumgartner, T. Ihn, and K. Ensslin, in collaboration with G. Papp and F. Peeters, University of Antwerp, Belgium, and K. Maranowski and A. C. Gossard, University of California, Santa Barbara, USA

A macroscopically well-known system in solid state physics is a Hall bar defined on a GaAs/AlGaAs heterostructure incorporating a two-dimensional electron gas 2DEG . Many topics of recent research and development are investigated in Hall bar systems, e.g., the integer quantum Hall effect, including its importance in metrology as a resistance standard, the fractional quantum Hall effect, or the optimization of the geometry in local probe and magnetic field sensors. One of the microscopic properties of this system is the local potential landscape that determines the electron scattering and therefore the electrical resistance of the sample. An elegant experimental tool to investigate such questions is a scanning probe microscope. The operation at cryogenic temperatures, high magnetic fields, and in high vacuum makes these experiments on 2DEGs a challenge, but recently a number of results have been reported.

In a scanning gate experiment on a Hall bar the longitudinal and the Hall resistances are measured by macroscopic Ohmic contacts. The conductive tip of an atomic force microscope AFM is scanned across the surface with a dc voltage applied with respect to the sample, thereby acting as a local gate that couples capacitively to the sample.

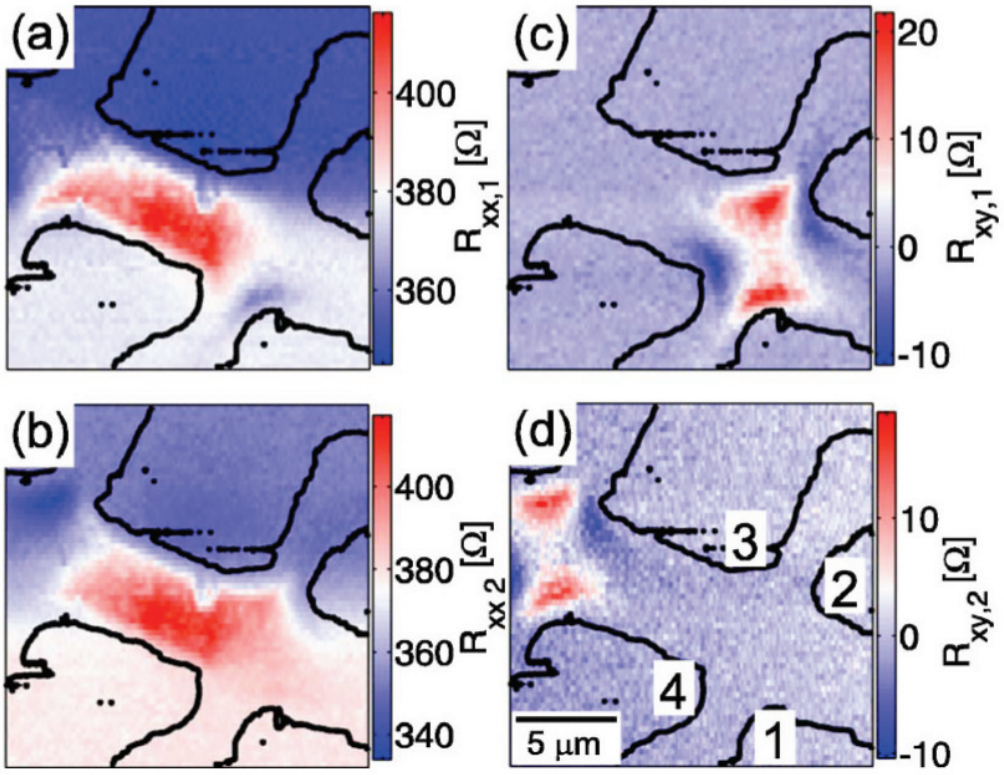

Figure 2.6: (a) Rxx,1, (b) Rxx,2, (c) Rxy,1, and (d) Rxy,2 in a scanning gate experiment at B=0. The numbers in (d) identify the corners of a Hall cross. The black lines are taken from a topography scan and overlaid on the scanning gate images.

Scans are performed either in constant height or in z-feedback mode. The tip-induced potential changes the local potential seen by the conduction band electrons at a position defined by the tip. The systemÕs response to this manipulation may lead to changes in the measured quantities. These are recorded as a function of tip position, which results in the so-called scanning gate images. A scanning gate experiment can be viewed as investigating a series of different samples, each with a controlled inhomogeneity at the tip position.

The experiments were performed on two Hall bars of width W=4.0 μm and contact separation L=10 μm, defined on a GaAlAs heterostructures with the 2DEG 52 nm below the sample surface. In Fig. 2.6 scanning gate images taken at zero magnetic field are presented. Figures 2.6 (a) and (b) show the longitudinal resistance measured at the lower two voltage contacts Rxx,1 and at the upper two contacts Rxx,2 of a Hall bar. One particular observation is that these two images are not exactly identical, i.e., the experiments allow one to distinguish the two pairs of measurement contacts. The scanning gate images for the Hall resistances Rxy,1 and Rxy,2 are depicted in Fig. 2.6 (c) and Fig. 2.6 (d), respectively. For further discussion we label the corners of the Hall crosses with numbers as introduced in Fig. 2.6 (d) . The images show that the Hall resistance, which is zero in a homogeneous sample, can be made nonzero by introducing an inhomogeneity in the sample. In contrast to the longitudinal resistance the Hall resistance is influenced only near the respective Hall cross area. A very distinct pattern is found: Around corners 1 and 3 (numbers refer to Fig. 2.6 (d)) the AFM tip leads to a positive Hall voltage, whereas in corners 2 and 4 the Hall voltage is negative. One can observe two lines of symmetry where the influence of the tip changes sign, namely along the respective centers of the current and voltage leads. The induced resistance changes are about $\pm 15\ \Omega$.

Scanning gate measurements on a Hall cross have been presented in the regime of the classical Hall effect. The real space patterns of induced resistance changes are manifestations of the symmetry properties of such a Hall system. The detailed behavior in the diffusive regime has been shown to be compatible with models based on a local conductivity tensor. Scanning gate experiments on a sample with a larger mean free path were found to show quasi-ballistic transport due to individual scatterers inside the Hall cross. We anticipate that experiments on smaller Hall bars or quantum wires will lead to the observation of coherent conductance fluctuations in real space and as a function of magnetic field.

2.7 Discrete charging of traps visualized by scanning gate experiments on a quantum point contact

A. Pioda, S. Kicin, D. Brunner, T. Ihn, M. Sigrist, and K. Ensslin, in collaboration with M. Reinwald and W. Wegscheider, University of Regensburg, Germany

Quantum point contacts QPCs are fundamental building blocks of semiconductor nanostructures. Their characteristic property is the quantization of the conductance at low temperatures, observed in very clean samples. The sensitivity of a QPC to single elementary charges placed in its proximity has been used for charge detection in quantum dots. Scanning probe techniques have been employed for the local investigation of QPCs. The nanostructure consists of a quantum dot and three QPCs. It has been defined by room temperature local anodic oxidation with a scanning force microscope (SFM) which allows us to write oxide lines on the surface of a semiconductor, below which the 2DEG is depleted. The measurements were performed with a SFM in a 3He cryostat with a base temperature of 300 mK. Magnetic fields of up to 9 T can be applied normal to the plane of the 2DEG. The scanning sensor consists of an electrochemically sharpened PtIr tip with a typical diameter of 30-60 nm for this experiment, mounted on a piezoelectric quartz tuning fork.

We identify two different effects of the scanning tip on the conductance of the QPC. The straightforward way to understand the influence of the tip on the QPC is to consider it as an additional gate which shifts the energies of the quantized modes. This leads to large conductance changes, and can be modeled in terms of elementary electrostatics. We call this the Ògating effectÓ of the tip. The second effect leads to much more subtle features, which can be barely recognized without further data analysis, and form sets of concentric conductance steps around different centers.

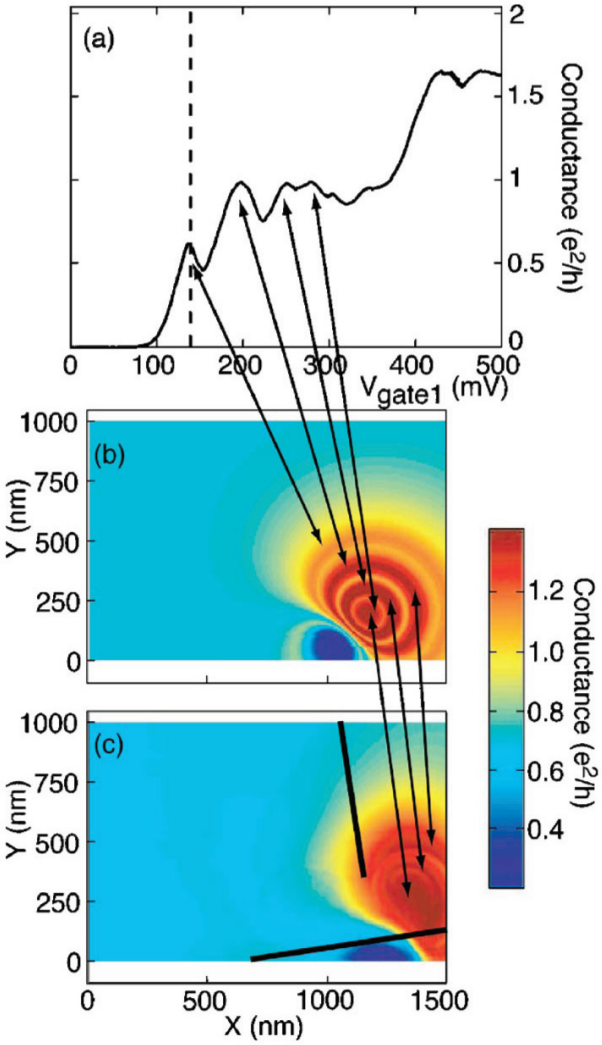

Figure 2.7: (a) Conductance trace of the QPC with the tip placed over the constriction. The voltage applied on gate 1 for the measurement in (c) is marked by the dashed line. (b) Simulation of the gating effect obtained by using the conductance trace and a model for the tip-induced potential explained in the text with the same parameters as used for the experiment. (c) Measured scanning gate image showing very similar features as the simulated image. The transmission modulations match almost exactly the experimentally observed ones. The position of the QPC is drawn in the image.

A typical scanning gate image is displayed in Fig. 2.7 (c). The position of the oxide lines defining the QPC constriction obtained from a topography scan has been drawn into the figure for better orientation as thick black lines . The voltage applied on gate 1 is 140 mV, and corresponds to a position in the conductance trace Fig. 2.7 (a) , dashed line slightly below the first peaked structure in the transmission, while the tip voltage is 1100 mV. The influence of the two different tips in the scanning gate image [Fig. 2.7 (c)] is evident. In the lower right part of the figure, the conductance through the QPC is reduced almost to zero, when the tip with an effective voltage of 600 mV is scanned over the constriction. The remaining right part of the figure shows a strong increase in conductance, with some oscillations, due to the presence of the tip with a positive effective voltage of 1300 mV. The oscillations can be matched quite exactly with the modulated transmission observed on the conductance trace in (a) . Thus, the tip, acting as an external gate shifts the position of the conductance trace of the QPC to lower or higher gate voltages. It is possible to verify this effect with a model of the tip-induced potential [see Fig. 2.7 (b)].

2.8 Top-gate defined double quantum dots in InAs nanowires

A. Pfund, I. Shorubalko, R. Leturcq, and K. Ensslin

Semiconductor nanowires (NWs) are gaining interest as possible building blocks in new bottom-up nanoelectronics and as versatile systems for transport studies in reduced dimensions. We describe a technologically simple and reliable process to create top-gate-defined double quantum dots in InAs NWs. The growth process is catalyzed by monodisperse Au particles with diameters of 40 nm. The resulting NWs are between 5 and 10 μm long and have diameters around 100 nm. They emerge with crystalline facets and hexagonal cross section. After growth, the NWs are transferred to a highly doped Si substrate covered by 300 nm of SiO_2. No predefined markers are needed, since the NWs can be located optically and contacts are defined by a single optical lithography step. Before metallization with subsequent layers of Ti (20 nm) and Au (180 nm), the contact areas are simultaneously etched and passivated with a diluted solution of $(NH_4)_2S_x$. The resulting contacts are of good quality with contact resistances below 100 Ω. Finally, top-gate fingers are created by electron beam lithography, followed by deposition of 6 nm Cr, 66 nm Au, and standard lift-off. A scanning electron microscope image of the device is shown in Fig. 2.8.

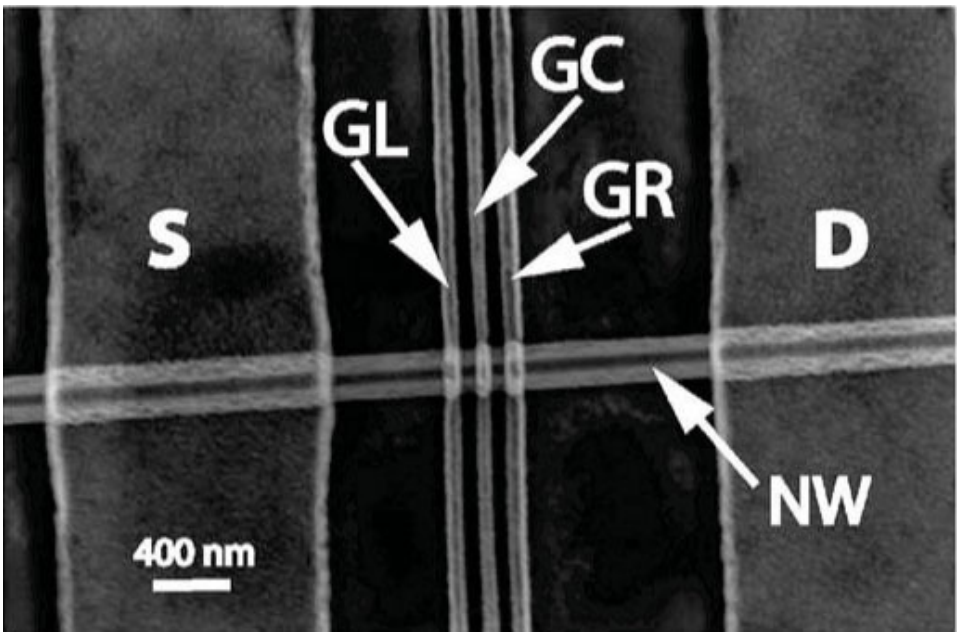

Figure 2.8: Scanning electron micrograph of a device similar to the one measured. Source S and drain D Ohmic contacts to the nanowire NW are defined by optical lithography. Top gates GL, GR, and GC have width and spacing of about 70 nm.

Data of one sample measured in a dilution refrigerator at a base temperature of 30 mK are presented. Two quantum dots in series can be formed by reducing the voltages on gates GL, GC, and GR. Figure 2.9 shows plots of the source-drain current I_{SD} at $V_{SD} = 140\mu V$ as a function of the voltages on left V_{GL} and right V_{GR} top gates for three different values of the center gate voltage VGC . In Fig. 2.8 (a) no significant barrier is induced by GC and a single quantum dot is formed between GL and GR. The current exhibits Coulomb oscillations: peaks occur when the electrochemical potential for the transition of an N electron state to the N+1 electron state is aligned with the electrochemical potentials in the contacts. Reducing V_{GC} leads to the formation of a double-well potential and induces a redistribution of the N electrons between the two valleys Fig. 2.8 (b). The electron numbers in the left and right dots are denoted as n and m, respectively. For even smaller V_{GC}, we obtain the characteristic honeycomb pattern for the charge stability diagram of the double dot. Within each hexagon of Fig. 2.8 (c) , the charge configuration (n,m) of the double dot is fixed. Elastic electron transport leading to high current is only possible at the corners of the hexagons marking the so-called triple points. Here, the electrochemical potentials of the n to n+1 electron transition in the left dot and the m to m+1 electron transition in the right dot are aligned with the source and drain chemical potentials. The series shown in Fig. 2.8 demonstrates the tunability from one large single dot to two mainly capacitively coupled dots.

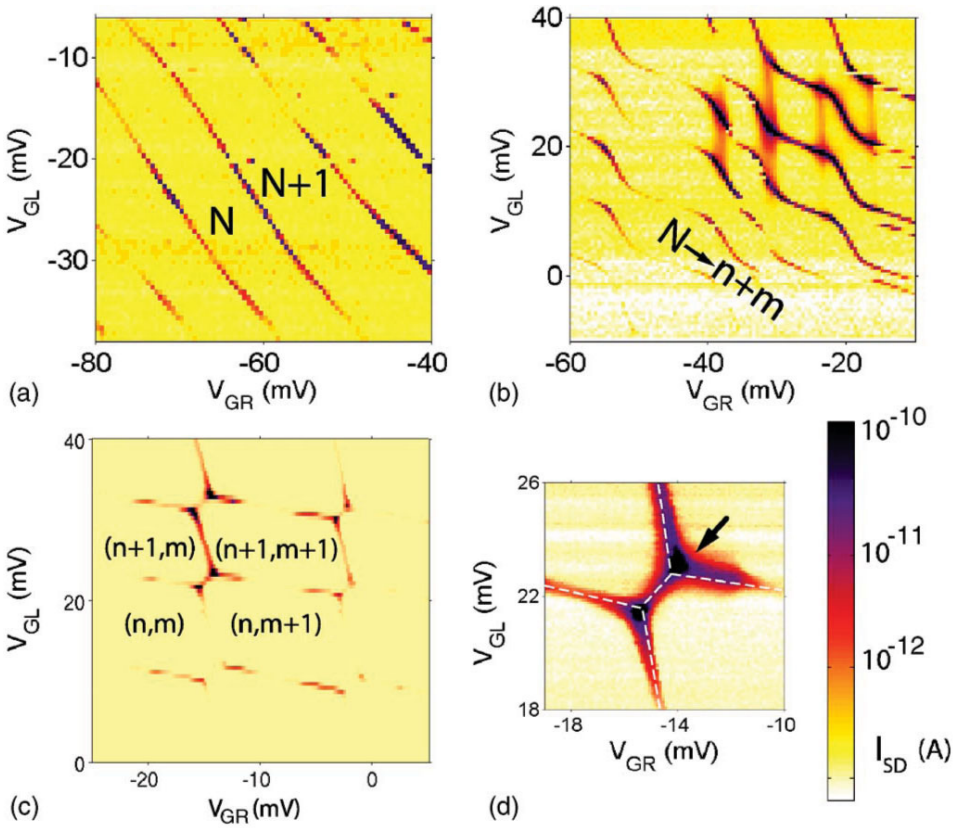

Figure 2.9: Source-drain current I_{SD} as a function of left and right gate voltages for different center gate voltages at fixed bias $V_{SD} = 140\ \mu$V. (a) At $V_{GC} = +200$ mV, an effective single dot is formed. The total number of electrons between the Coulomb peaks is fixed N,N +1, ... (b) $V_{GC} = 0$ mV. Electrons are redistributed in the double well potential. (c) $V_{GC} = -120$ mV yields the charge-stability diagram for two capacitively coupled dots. (d) Zoom around one pair of degeneracy points. The deviation from the capacitive model (dashed lines) is clearly visible see arrow .

2.9 Construction of a dilution refrigerator cooled scanning force microscope

A. E. Gildemeister, T. Ihn, C. Barengo, P. Studerus, and K. Ensslin

It is desirable to cool scanning force microscopes (SFMs) to very low temperatures either to improve the force sensitivity or to study samples that only function at low temperatures. While liquid helium SFMs are now commercially available and several scanning tunneling microscopes for dilution refrigerators have been reported, to date only a handful of SFMs was built for dilution refrigerators.

Figure 2.10 shows the microscope, consisting of two main components, the x-y table at the top and the z module at the bottom. The sample is mounted in a ceramic chip carrier which fits into the chip socket at the bottom of the x-y table. The z module comprises the sensor, the scan piezo, and the Macor tube holding the piezo. The upside-down geometry reduces the contamination of the sample surface by dust particles. The different components are mounted in a rigid single-piece CuBe frame. The x-y table contains a Pt100-, an Allen-Bradley-, and a RuO_2 thermometer to cover the instrumentÕs temperature range. A resistive wire allows in situ heating of the sample to room temperature, and a LED can illuminate the sample. The chip socket connects to 24 coaxial cables. Five of these allow driven-shield operation which increases the bandwidth by a factor of about 5 compared to operation with a grounded shield. Slip-stick motors allow lateral coarse positioning with a range of about 3 mm at low temperatures. For this we use three 16 mm long piezo tubes that are glued perpendicular to the plane of motion. Small sapphire spheres are glued to both ends of each tube. These support stainless-steel caps which are polished and coated with Balinit C/WC. The tubes with the caps are sandwiched between two sapphire surfaces that are clamped together by a spring. These form the x-y table and support the sample mount.

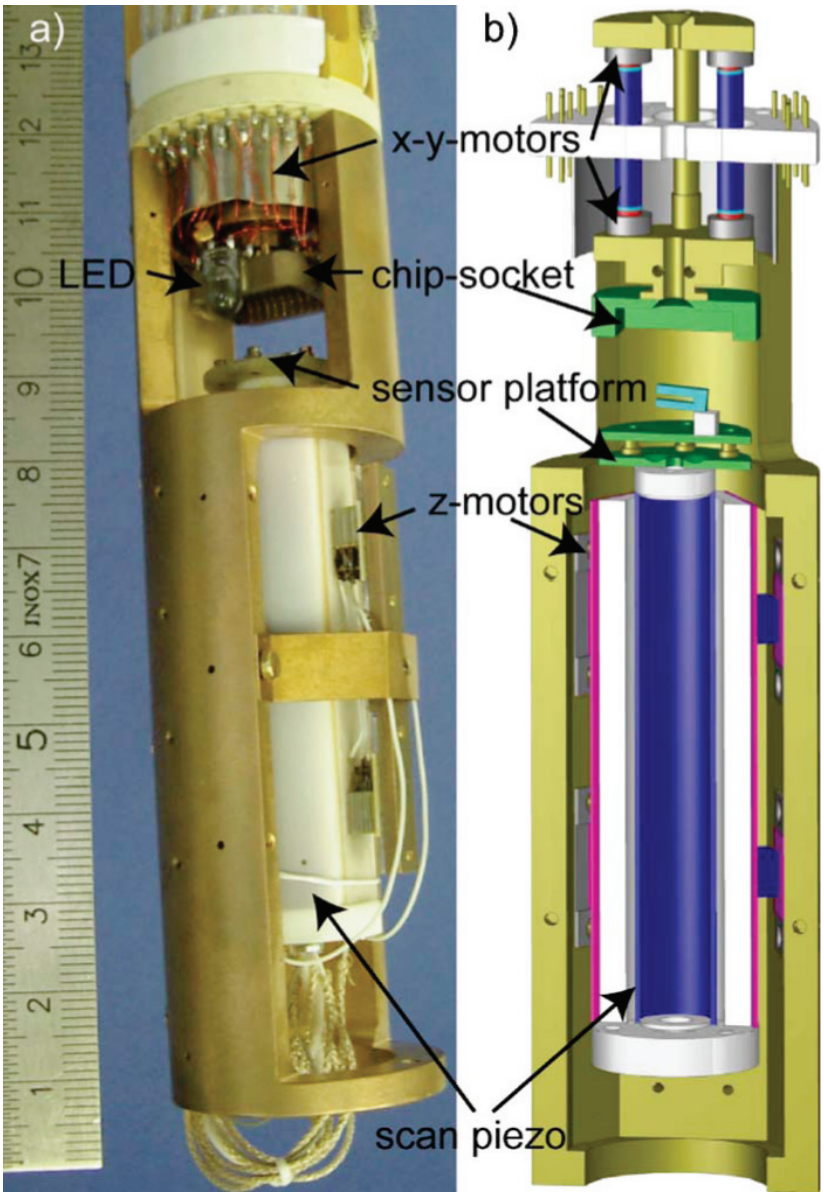

Figure 2.10: (a) A photograph and (b) a sectional drawing of the microscope. It connects to the mixing chamber at the top.

For transport measurements and sensor control we use homebuilt preamplifiers operating at room temperature. They are installed in a HF-tight box mounted at the top of the dewar, thereby preventing noise pickup on the long cables from the dewar to the instrument rack. Using differential inputs eliminates ground loops. The Nanonis system that we use for controlling the microscope features a digital phase-locked loop, a real-time computer for all time-critical operations, and user-friendly software.

As first application we demonstrate that this microscope can be used to image oxide lines defining a quantum dot at milliKelvin temperatures. Furthermore, scanning gate images of quantum dots have been obtained.

2.10 Spatially Resolved Raman Spectroscopy of Single- and Few-Layer Graphene

D. Graf, F. Molitor, and K. Ensslin, in collaboration with C. Stampfer, A. Jungen, and C.Hierold, Micro and Nanosystems, ETH Zurich, Switzerland, and L. Wirtz, CNRS Lille, France

The interest in graphite has been revived in the last two decades with the advent of fullerenes and carbon nanotubes. However, only recently single- and few-layer graphene could be transferred to a substrate. Transport measurements revealed a highly-tunable two-dimensional electron/hole gas of relativistic Dirac Fermions embedded in a solid-state environment. Going to few-layer graphene, however, disturbs this unique system in such a way that the usual parabolic energy dispersion is recovered. The large structural anisotropy makes few-layer graphene therefore a promising candidate to study the rich physics at the crossover from bulk to purely two- dimensional systems. Turning on the weak interlayer coupling while stacking a second layer onto a graphene sheet leads to a branching of the electronic bands and the phonon dispersion at the K point. Double-resonant Raman scattering which depends on electronic and vibrational properties turns out to be an ingenious tool to probe the lifting of that specific degeneracy.

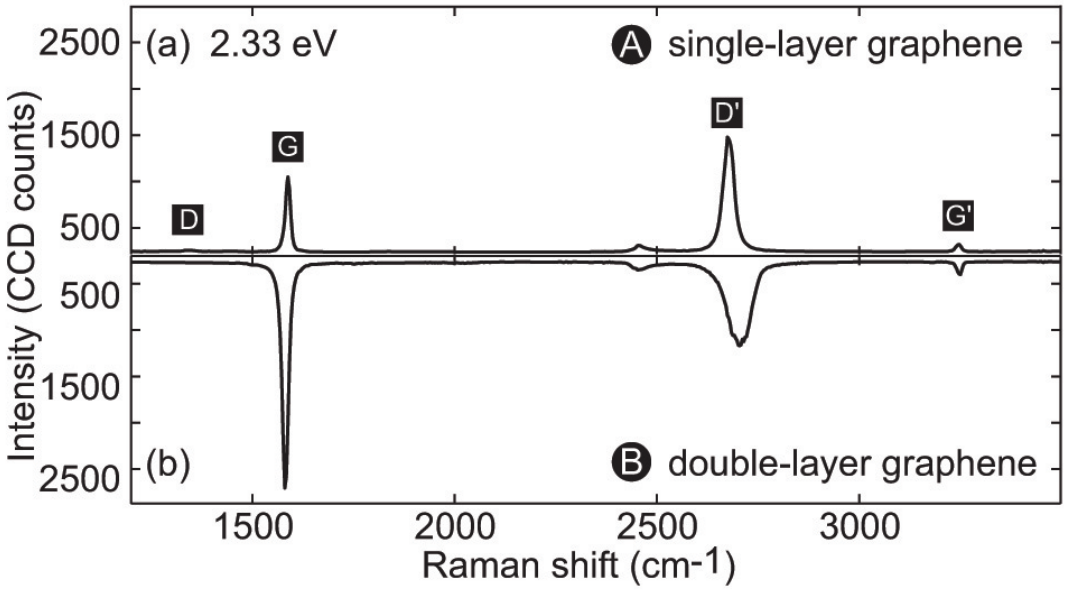

Figure 2.11: Raman spectra of (a) single- and (b) double-layer graphene.

The graphite films were prepared by mechanical exfoliation of highly oriented pyrolytic graphite (HOPG) and subsequent transfer to a highly doped Si waver with 300 nm SiO_2 (atomic oxidation process) cap layer. The combination of optical microscopy using phase contrast and SFM makes it possible to locate flakes with various thicknesses down to a monolayer with lateral extensions in the micrometer range. The Raman spectra were acquired using a laser excitation of 532 nm (2.33 eV) delivered through a single-mode optical fiber, whose spot size is limited by diffraction. Using a long working distance focusing lens with a numerical aperture NA=0.80 we obtain a spot size of about 400 nm.

The Raman spectrum of graphite has four prominent peaks (Fig. 2.11). The peak around 1582 cm^{-1}, commonly called G line, is caused by the Raman active E_{2g} phonon, (in-plane optical mode) close to the Γ point. The D line around 1350 cm^{-1} exhibits two remarkable features: its position shifts to higher frequencies with increasing incident laser excitation energies and its relative signal strength (compared to the G line) depends strongly on the amount of disorder in the graphitic material. The associated overtone D' around 2700 cm^{-1} is pronounced even in the absence of a D signal. Raman spectra for multiple graphene layers can be compared qualitatively and quantitatively while investigating flakes with sections of various thicknesses. The FWHM (full width at half maximum) of the D' line shows a narrowing at the transition to a single-layer (see e.g. Fig. 2.11) and gives an evident contrast between single- and few-layer graphene sections.

In Fig. 2.11(a) and (b), we compare the Raman spectra of the double- and single-layer graphene. The Raman signal is significantly altered when peeling off the penultimate layer: the G peak decreases strongly in intensity and shifts towards higher wave numbers.

Raman mapping reveals to be a powerful tool to investigate single- and few-layer graphene flakes. It turns out that the width of the D' line is highly sensitive to the crossover from single- to double-layer graphene, which is explained by a peak splitting following the double-resonant Raman model together with ab initio electronic band structure

calculations. A remaining open question is the decrease of the G line intensity with decreasing layer number compared to the almost constant spectral weight of the D' line. The structural quality of the flakes is studied by analyzing the D line intensity: no defects are detected in the inner part of the flake. The D line signal from the boundaries of the individual sections of the flake suggest that they act as elastic scatterer.

2.11 Phase coherence of holes and weak anti-localization in p-type GaAs heterostructures

B. Grbic, R. Leturcq, T. Ihn, and K. Ensslin, in collaboration with D. Reuter and A. Wieck, Univ. of Bochum, Germany

Weak localization is a quantum mechanical effect which arises from the constructive interference between time reversed paths and leads to an increase of the longitudinal magnetoresistance due to enhanced backscattering. However, in the presence of strong spin-orbit interaction, spins of the two interfering partial waves rotate in opposite directions, and therefore interfere destructively. This destructive interference leads to a decrease of the longitudinal magnetoresistance. This effect is called weak anti-localization. Thus, the change of the magnetoresistance around zero magnetic field from negative to positive is a clear sign for the presence of strong spin-orbit interaction in the system.

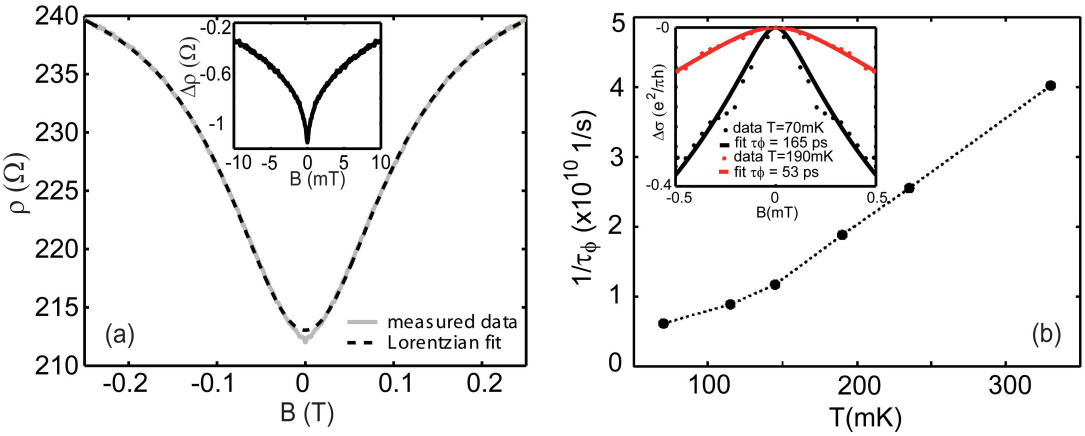

Figure 2.12: (a) Measured positive magnetoresistance of the p-type C-doped GaAs heterostructure (grey line) together with a fit of the classical Lorentzian-shaped positive magnetoresistance due to the presence of the two spin-split subbands (dashed line); Inset: Weak anti-localization correction to the resistance obtained as a difference between the measured data and the Lorentzian fit. (b) Temperature dependence of the phase-coherence time of holes; Inset: Extraction of the phase coherence time from the fit of the anti-localization peak with Hikami-Larkin-Nagaoka theory.

We measured the positive magnetoresistance of a two-dimensional hole gas with density $n = 2.3 \cdot 10^{15}$ cm^{-2} and mobility $\mu = 130000$ cm^2/Vs around B=0 T [gray line in Fig. 2.12 (a)]. In the measured data we can clearly distinguish two contributions in the low-field magnetoresistance: a classical Lorentzian-shaped positive magnetoresistance due to the presence of the two spin-split subbands [dashed line in Fig. 2.12 (a)] and weak anti-localization dip [inset in Fig. 2.12 (a)]. These two effects, together with the observed beating of Shubnikov-de Haas oscillations at higher magnetic fields represent clear evidence for the presence of strong spin orbit interaction in C-doped p-type GaAs heterostructures. The spin-orbit induced splitting of the two spin-split subbands at the Fermi level is estimated to be 10-15% of the total Fermi energy for the typical densities in our samples.

By fitting the weak anti-localization dip with standard Hikami-Larkin-Nagaoka theory up to the fields $B_{tr} \approx 0.5$ mT we extracted a phase-coherence time of holes to be $\tau_\phi \approx$165 ps at the base temperature of 70 mK [inset to Fig. 2.12]. This corresponds to the phase-coherence length larger than 2 μm, which is very promising for the fabrication of phase-coherent hole nanostructures. We found that the phase-coherence time of holes decreases in a almost linear fashion with increasing hole temperature [Fig. 2.12 (b)]. At 350 mK phase-coherence time is $\tau_\phi \approx$25 ps, and above this temperature it is not possible anymore to resolve the anti-localization dip.

Extraction of the spin-orbit scattering time τ_{SO} is limited by the fact that all present theories are developed for the diffusive regime and are formally valid only in magnetic fields up to the $B_{tr} \approx 0.5$ mT in our case. Besides, spin-orbit interaction is considered only as a weak perturbation in most of these theories. However, if we try to fit the tails of the anti-localization dip beyond the field $B_{tr} \approx 0.5$ mT we obtain a rough estimate of the $\tau_{SO} \approx 3$ ps. Although this number is not completely reliable, it represents a good indication that the sample is in the regime where $\tau_{SO} < \tau_{tr} < \tau_{\phi}$, ($\tau_{tr}$ is the transport scattering time and in our case about 26 ps) where spin-orbit interaction is very strong and only the anti-localization dip is present. In the case when spin-orbit interactions are only a weak perturbation, $\tau_{tr} < \tau_{SO} < \tau_{\phi}$, a small anti-localization dip is superimposed on a larger weak localization peak, while in the case when spin-orbit interactions are negligible, $\tau_{tr} < \tau_{\phi} < \tau_{SO}$, only a weak localization peak is present. Therefore our anti-localization measurements clearly demonstrate the presence of the strong spin-orbit interactions in two- dimensional hole systems and allow the determination of the phase-coherence time of holes.

2.12 Thermoelectric power of strongly correlated systems in the coherent regime

R. Monnier, in collaboration with V. Zlatic (Institute of Physics, Zagreb, Croatia) and J. Freericks (Georgetown University, Washington D.C., USA)

The low-temperature properties of heavy fermions and valence fluctuators with Ce, Eu, Yb and U ions are continuing to attract considerable attention. Several recent papers [1,2] have reported on a correlation between the low-temperature Seebeck coefficient α and the specific heat coefficient $\gamma = C_V/T$ and shown that the ratio $q = |e| \lim_{T\to 0} \alpha/\gamma T$ in most systems is about the same, although the absolute values of γ and α/T vary by orders of magnitude. A similar 'quasi-universal' behavior is exhibited by the Kadowaki-Woods (KW) ratio [3], $\rho(T))/(\gamma T)^2$, where $\rho(T)$ is the electrical resistance. These results suggest a 'universal law' for the low-temperature power factor $P = \alpha^2/\rho$ and bring to the fore the validity of the Wiedeman-Franz (WF) law and renormalization of the thermoelectric 'figure-of-merit' $ZT = \alpha^2 T/\kappa\rho$, where κ is the thermal conductivity. The 'universality' of the q-ratio and the KW ratio has been addressed recently by several authors [4-6] using different approximation schemes of the N-fold degenerate periodic Anderson model. In our work we have used the dynamical mean field theory (DMFT) to establish the Fermi liquid (FL) laws and we show that the KW ratio and the power factor have an explicit N-dependence, while the q-ratio and ZT do not. We also show that there is a temperature window in which the the electron correlations lead to a large deviations from the WF law and enhance $ZT > 1$.

[1] K. Behnia et al., J. Phys. C: Condensed Mat. **16**, 5187 (2004)
[2] J. Sakurai and Y. Isikawa, J. Phys. Soc. Japan **74**, 1926 (2005)
[3] K. Kadowaki and S. B. Woods, Solid State Commun. **71**, 1149 (1987)
[4] K. Miyake and H. Kohno, J. Phys. Soc. Japan **74**, 254 (2005)
[5] H. Kontani, J. Phys. Soc. Japan **73**, 515 (2004)
[6] N. Tsujii et al., Phys. Rev. Lett. **94**, 057201 (2005)

2.13 Non-local effects in dynamical mean field theory

R. Monnier, in collaboration with V. I. Tokar (Institute of Magnetism, National Academy of Sciences, Kiev, Ukraine)

As it stands, dynamical mean field theory (DMFT) replaces the problem of interacting fermions on a lattice by that of a an impurity carrying strongly correlated electron states, embedded in a bath of conduction electrons. The purpose of this work is to generalize the method in order to include spatially non-local effects, of which we think that they are crucial for the explanation of eg. magnetic order and superconductivity, but without resorting to the use of clusters, which is the route currently followed by a number of groups. Our approach is based on the gamma expansion method (GEM) introduced by one of us (V.I.T.) over 20 years ago for the study of short-range order in an FCC Ising lattice [1]. In the present context, the expansion parameter is the site-off-diagonal part of the electronic Green's function

in the original Hamiltonian and, to lowest order, the method reduces to the standard DMFT. As a first step, we have applied our method to the study of the magnetic short-range order parameter in the strongly correlated (i. e., large U) Hubbard model at half-filling.

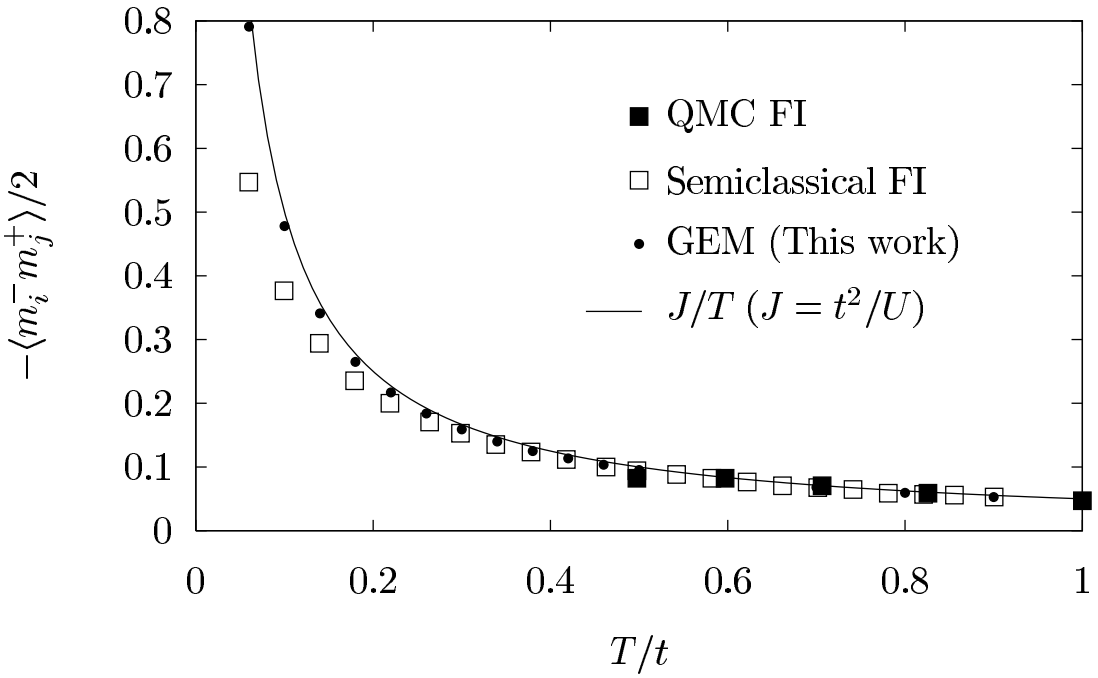

Figure 2.13: Magnetic short range order parameter for the NN sites i and j calculated to the lowest nontrivial order of the gamma expansion method (GEM) in comparison with the cluster technique of Ref. [2], called by the authors the fictive impurity (FI) method, and with the leading term of the high temperature expansion of the superexchange interaction. The square dots correspond to data calculated by two different methods in Ref. [2].

As seen in Fig. 1, our results compare well with those obtained by Okamoto et al. [2] with the so-called fictive impurity model, and confirm the shortcoming of the dynamical cluster approximation which yields far too large values for that parameter.

[1] V. I. Tokar, Phys. Lett. A **110**, 453 (1985)
[2] S. Okamoto et al., Phys. Rev. B **71**, 235113 (2005)

Chapter 3

Condensed matter at low temperatures

(http://www.solid.phys.ethz.ch/ott)

Head
Prof. Dr. H. R. Ott

Academic Staff
M. Weller Dr. A. Sacchetti

Technical Staff
H. R. Aeschbach

Administrative Staff
C. Vinzens

Doctoral theses
Sabine Streule
Neutron Diffraction Study of Cobaltite Systems
26.4.2006

Oliver Marc Wittwer
Solidification of Xenon: Instabilities leading to Complex Structures
13.6.2006

3.1 Low-field NMR investigation of $CeAl_3$ under hydrostatic pressure

^{27}Al NMR spectra and spin-lattice relaxation rates were measured under pressure in the heavy-electron compound $CeAl_3$. The measurements, using a powdered sample, were done in a rather low external magnetic field of approximately 0.1 T, under hydrostatic pressures up to 9 kbar and at temperatures between 60 mK and 2 K. In order to obtain reasonable signal to noise ratios, these experimental conditions required very long measurement times.

Drastic changes of the NMR spectra and of the spin-lattice relaxation rates T_1^{-1} were observed with increasing pressure. For $p < 1.2$ kbar, the ^{27}Al spectra are rather broad and complicated, as previously observed at ambient pressure [1]. The situation changes significantly at higher pressures (see Fig. 3.1). The spectra narrow rapidly and can be reproduced by simple simulation calculations (see Fig. 3.4). The spin-lattice relaxation rate drops by almost 2 orders of magnitude upon increasing the pressure up to 9 kbar, indicating a substantial decrease of the density of electronic states $D(E_F)$ at the Fermi energy. Likewise the Knight shift K decreases upon enhancing the pressure. The quoted earlier NMR experiments [1] on the same sample at zero external pressure revealed a broad NMR signal, consisting of at least two contributions and indicating a magnetically and electronically inhomogeneous ground state. Our experiments confirm this observation in the low-pressure regime, but our additional data at elevated pressures suggest that the ground state is that of a simple paramagnet at pressures exceeding 1.2 kbar. Rather unexpected is the considerable pressure induced variation of the anisotropy parameter η of the electric field gradients at the Al sites, which is revealed by the comparison of the measured spectra with corresponding simulation calculations (see also section 3 below).

Thus, rather moderate external pressures lead to a substantial alteration of the ambient pressure ground-state properties of $CeAl_3$. In particular we confirm a considerable reduction of the anomalously enhanced effective mass of the conduction electrons, as was concluded before from measurements of the specific heat under pressure [2]. Concomitantly, enhanced pressure seems to quench the electronic inhomogeneities that were reported in ref.1. The high-pressure low-temperature state of $CeAl_3$ exhibits the properties of a simple paramagnetic metal and our data indicate the absence of any magnetic order above 60 mK.

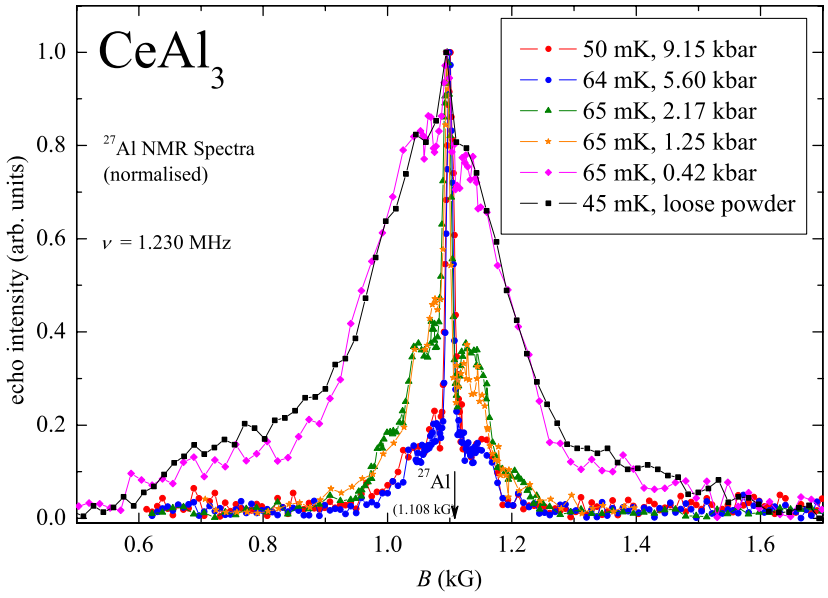

Figure 3.1: ^{27}Al NMR spectra of $CeAl_3$ at very low temperatures under various external pressures. The solid lines are guides to the eye.

3.2 Cu NQR measurements on $PrCu_2$

$PrCu_2$ is an intermetallic compound for which the Pr^{3+} 4f-electron Hund's rule ground state is completely split into singlet states. In such materials the onset of magnetic order is usually observed only at low temperatures, if at all. Motivated by a recent report of a μSR investigation [3] on $PrCu_2$, claiming the onset of magnetic order

in this compound at T = 65 K, we attempted to confirm or refute this rather unexpected result by means of Cu-NMR experiments. The recorded ^{63,65}Cu-NMR powder spectra and the relaxation data were very difficult to analyse, because of the large anisotropies of the Knight shift and of the electric-field gradient. More recently, our attempts to observe the Copper nuclear quadrupole resonance (NQR) in $PrCu_2$ in zero magnetic field were successful and we made a series of corresponding experiments in the temperature range between 4.2 K and room temperature (see Fig. 3.2). Our data reveals no anomaly around 65 K, neither in the temperature variation of the line-width or -shape, nor in the relaxation rates. By comparison with other similar data sets we conclude that our results do not reflect the onset of magnetic order in the claimed range of temperature. Nevertheless, the temperature dependence of the spin lattice relaxation rate $T_1^{-1}(T)$ exhibits anomalous features. Below 300 K, a power-law type decrease of T_1^{-1} with decreasing temperature is intercepted by another power-law type increase below 100 K (see Fig. 3.3). In view of the crystal-field split 4f electron levels and their decreasing occupancy with decreasing temperature, this latter feature of $T_1^{-1}(T)$is rather unexpected and not understood at present. The cusp like maximum in $T_1^{-1}(T)$ at $T = 7.5$ K reflects the previously reported phase transition [4,5] that was identified as an induced Jahn-Teller structural phase transition by neutron scattering experiments [6,7].

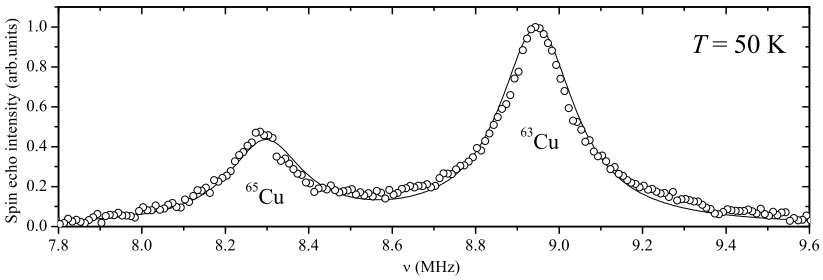

Figure 3.2: ^{63,65}Cu NQR spectrum of $PrCu_2$, representative for the entire covered temperature range. The open circles represent experimental data and the solid line is a simulation employing the code described in subsection 3.

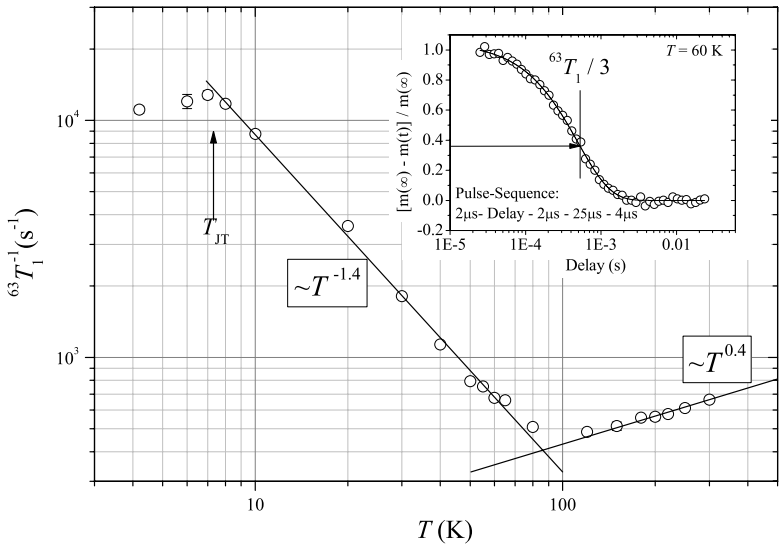

Figure 3.3: Temperature dependence of the spin-lattice relaxation rate T_1^{-1}(T) of the ^{63}Cu nuclei in $PrCu_2$. The inset represents the experimental magnetization recovery (open circles) and the appropriate fit function for extracting T_1 (solid line).

3.3 NMR/NQR spectrum simulation package

NMR and NQR spectra of solids are often characterized by very complex structures containing several peaks and broad features which are in most cases difficult to be identified and assigned *a priori*. The possibility of simulating

the NMR/NQR spectra starting from the microscopic parameters characterizing the nuclear-spin Hamiltonian is thus really useful in this context. Despite of this, to the best of our knowledge, such a tool, specifically developed for solid-state NMR/NQR, seems not to be available. On the other hand, applications of the presently existing general-purpose NMR-codes for this task are quite far from being straightforward. For this reason, we developed a simple but powerful *fortran77* code, especially designed for simulations of solid state NMR/NQR spectra. The program starts from the microscopic parameters describing the hyperfine field (in the form of the Knight-shift parameters) and the quadrupolar components (in the form of the electric-field-gradient parameters) of the nuclear spin Hamiltonian and performs a numerical diagonalization. The spectrum is then reconstructed according to the energy eigenvalues and the corresponding transition-probabilities obtained from the eigenvectors. We also implemented the possibility of considering different isotopes and/or different lattice sites for the respective nucleus, as well as the calculation of both single-crystal and powder spectra. The simulation can equivalently be run for a fixed magnetic field as a function of the frequency or for a fixed frequency and sweeping the magnetic field.

In Fig. 3.4 we compare the experimental ^{27}Al NMR field-sweep powder-spectrum obtained in the high-pressure phase of the heavy-electron compound $CeAl_3$. The corresponding simulation obtained by means of the present code is also shown. The good agreement between the experimental and simulated curves allowed us to conclude that the high pressure phase of $CeAl_3$ is characterized by an anomalously large anisotropy η parameter of the electric-field-gradients at the Al sites.

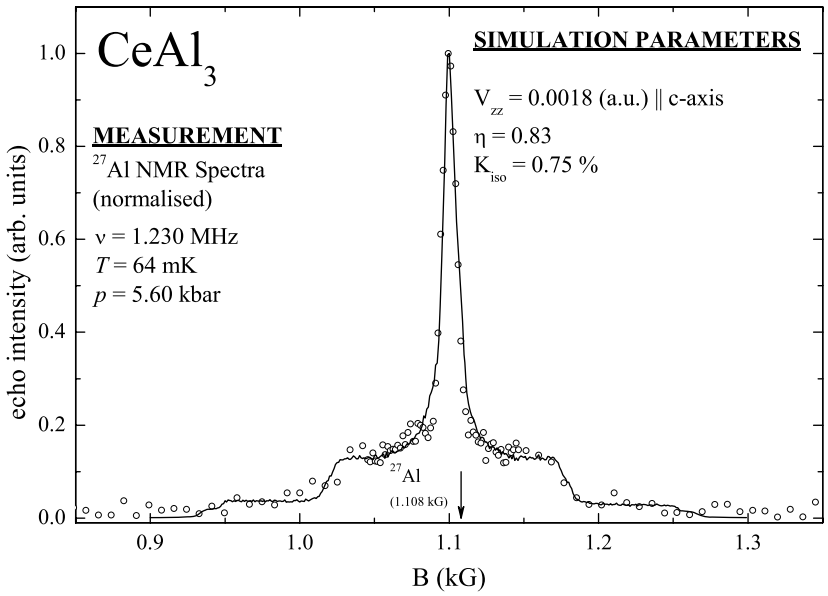

Figure 3.4: Field sweep NMR powder-spectrum of $CeAl_3$ at 5.60 kbar, 64 mK and for a frequency of 1.230 MHz. Symbols: experimental data, solid line: simulation. The essential numerical fit parameters, namely the principal axis electric-field-gradient (V_{zz}), the in-plane anisotropy (η) and the isotropic Knight-shift (K_{iso}), are displayed in the panel.

[1] J.L. Gavilano, J. Hunziker, and H.R. Ott, Phys. Rev. B **52** R13106 (1995).
[2] G.E. Brodale et al., PRL **56**, 390 (1986).
[3] A. Schenck, F. N. Gygax, and Y. Onuki, Phys. Rev. B **68** 104422 (2003).
[4] K. Andres, E. Bucher, J. P. Maita, and A. S. Cooper, Phys. Rev. Lett. **28** 1652 (1972).
[5] M. Wun and N.E. Phillips, Phys. Lett. **50A**, 195 (1974).
[6] H. R. Ott, J.K. Kjems and K. Andres, Proc. of the Conf. on Rare Earth and Actinides, Durham 1977, IOP Conference Series **37**, 149.
[7] J.K. Kjems, H.R. Ott, S.M. Shapiro and K. Andres, J. Phys.(Paris), Colloq. **39**, C6 (1978).

Chapter 4

Microstructure research

(http://www.microstructure.ethz.ch)

Head
Prof. Dr. D. Pescia
Prof. Dr. M. Erbudak

Academic Staff

S. Burkard (Ph.D.Student)	P. Can (- April)	J.-N. Longchamp (Ph.D.student)
T. Michlmayr (Ph.D. student)	O.Portmann (Postdoc)	N. Saratz (Ph.D. student)
Y. Weisskopf (Jan-Sep Ph.D. student, Sep-Dec Postdoc)		
Dr. U. Ramsperger (Postdoc)	Dr. M. Hochstrasser (Postdoc)	
Dr. A. Vindigni (Postdoc)	Dr. A. Vaterlaus (40%, Didactical teaching)	

Technical Staff
Th. Bähler (75%)

Academic Guests
Prof. Rifat Çapan, Balikesir University, Turkey, 30.1.2006 - 5.2.2006
Burak Bilki, Bogaziçi University, Istanbul, 5.2.2006 - 14.2.206
Dr. Michael Hochstrasser, Elettra, Italien, 10.5.2006 - 17.5.2006
Dr. Ilker Yildiz, METU, Ankara, 20.8.2006 - 27.8.2006
Prof. Dr. A. Cannas, University of Cordoba, Argentina, May 2006

Doctoral theses
Weisskopf Y.
Growth of CsCl-type domains on icosahedral quasicrystal Al-Pd-Mn
11.9.2006

Diploma theses
Zgraggen D.
SEMPA studies of the stripe phase in ultrathin films of Iron on Copper at low temperatures
WS 2005/06

Burkardt S.
Growth mode of Co deposited on AlCo domains formed on the pentagonal surface of an icosahedral Al-Pd-Mn quasicrystal
SS 2006

4.1 Nanoscale magnetism

4.1.1 Observation of stripe mobility in a dipolar frustrated ferromagnet

(O. Portmann, A. Vaterlaus, D. Pescia, Phys. Rev. Lett. **96**, 047212 (2006))

The dipolar frustrated ferromagnet (DFF) is a model system exhibiting frustration on different spatial scales. DFF is a example of a special class of Hamiltonians first investigated by Brasovsky and undergoing, in spatial dimensions ≥ 2, a first-order equilibrium phase transition to a structure with modulated order parameter. In 1995, Kivelson and coworkers proposed for such models the existence of at least three characteristic temperatures. Within a domain of a modulated phase, the order resembles that of the unfrustrated system. Thus, there is a temperature T_c^0 at which the 'local' (= inside the domain) value of the order parameter vanishes. A frustrating interaction of strength Q produces a further temperature T_c^Q – the Brasovsky temperature, at which a modulated ordered state develops out of the disordered state. In addition, the Brasovsky phase transition might be kinetically avoided, with the system undergoing a liquid-glass transition at T_A instead: lowering the temperature, one starts with an essentially featureless paramagnetic state, then mobile stripes or domains develop and form a stripe or domain liquid. Then, the dynamics becoming more and more sluggish, a stripe or domain glass appears. The existence of T_A has been confirmed by various theoretical works, but clear experimental evidence is still missing.

Here we demonstrate two new aspects of the stripe-domain-to-paramagnetic transition in perpendicularly magnetized ultrathin ferromagnetic films of Fe on Cu(100), which, because of the competition between the exchange interaction (J) and the dipolar interaction (Q), are an example of a stripe-forming DFF with $\frac{Q}{J} \ll 1$. First, we find a characteristic temperature, which we identify as T_c^0, close to which the mean stripe width $\bar{L}$ approaches a finite value $\bar{L}_c$ according to $(\bar{L}-\bar{L}_c) \propto (T_c^0-T)^2$, precisely the law we obtain from a mean field argument. Second, in a narrow temperature range below T_c^0 the stripes become mobile. This mobility could be indicative of the predicted dynamical singularity. Images of the stripe phase are taken with SEMPA (Scanning Electron Microscopy with Polarization Analysis). A focused electron beam with typically 2 keV primary energy is directed toward a single-crystal Cu(100) surface supporting MBE grown fcc Fe films with variable thickness D, D being in the $1-2$ AL (atomic layers) range. The incident electron beam locally ejects low-energy secondary electrons which are then sampled and analyzed with respect to their spin polarization vector $\vec{P}$ in a spin-sensitive experiment. $\vec{P}$ is a measure of the local magnetization vector within the electron beam focus: Scanning the primary electron beam across the surface produces images of the local magnetization vector. In the following, only the component of $\vec{P}$ perpendicular to the film surface is shown (denoted by P), because the two remaining in-plane components vanish within the sensitivity of our experiment. At each spatial location, a grey scale is used to represent P, the black-and-white contrast corresponding to domains with opposite values of P.

4.1.2 Local magnetic field generation with a scanning tunneling microscope

T. Michlmayr, N. Saratz, A. Vaterlaus, D. Pescia, U. Ramsperger, J. Appl. Phys. **99**, 08N502 (2006)

The aim of this project is magnetic manipulation on the nanoscale. Here we present a technique that allows the application of localized magnetic fields with the help of a ferromagnetic tip of a scanning tunneling mircroscope (STM). The STM tip is guided at will on top of the sought-for-magnetic element with the help of a Scanning Electron Microscope (SEM). We test the technique on a sample consisting of epitaxial Fe films grwon by Molecular Beam Epitaxy onto a Cu(100) surface. Sharp ferromagnetic Co-tips were produced by electrochemically etching in a solution of HCl in H_2O. The switch-off time of the etching current determines the apex radius of the tip. In addition, the cone angle can be altered by adjusting the submersion depth of the Co wire into the etching solution. In order to remove oxide layers from the tip's surface, it is annealed in UHV close to the melting point. Magnetic imaging of the ferromagnetic tips and of the magnetic elements is performed with SEMPA (see description in the previous paragraph).

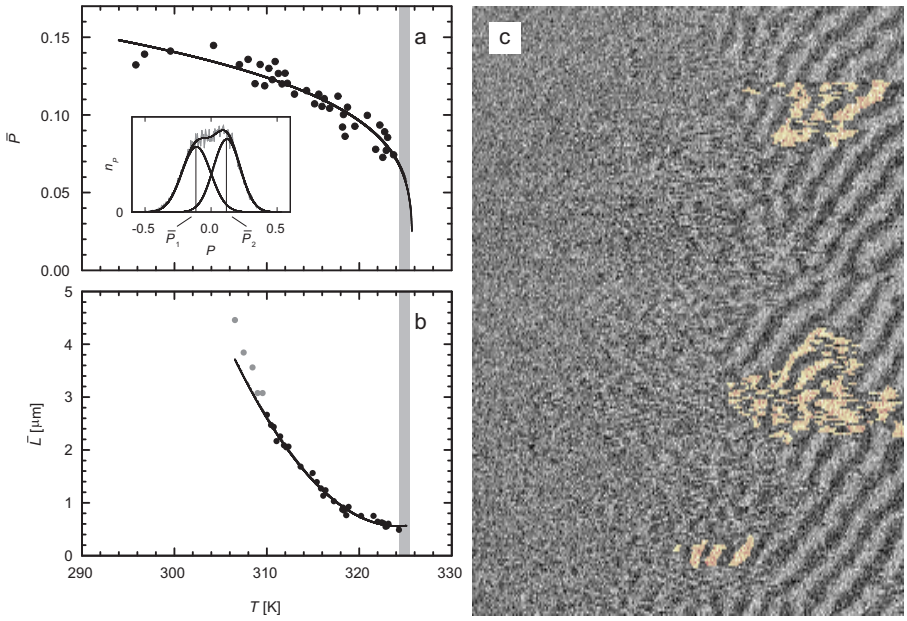

Figure 4.1: (top left) plots the spatial average $\bar{P}$ of $|P|$ versus T for a film of uniform thickness $D = 1.95$ AL. For the exact determination of $\bar{P}$ see the original literature. $\bar{P}$ is a measure of the mean spin polarization **inside** the stripes, i.e. the local magnetization. The temperature dependence of $\bar{P}$ in Fig. 4.1 (top left) – a slow variation at low temperatures followed by an enhanced decrease within a small temperature range – suggests that the magnetization approaches its Curie-temperature T_c^0. Following standard methods we estimate T_c^0 by fitting the experimental data in Fig. 4.1 (top left) with a power law $\bar{P} \propto (T_c^0 - T)^\beta$ (continuous curve) and obtain $T_c^0 = 325.7 \pm 1.3$ K. In the same temperature range, we observe [Fig. 4.1 (bottom left)] that the mean stripe width $\bar{L}$, obtained by counting the number of stripes within a given length, settles down according to $(\bar{L} - \bar{L}_c) \propto (T_c^0 - T)^2$ (continuous line) toward a limiting value $\bar{L}_c \neq 0$, in agreement with a mean field argument which explains in details in the original literature. Below T_c^0, we observe a temperature interval [shaded area in Fig. 4.1 (top left)], inside which the stripes acquire mobility, see Fig. 4.1 (right). Mobility stops at a temperature (which we identify as T_A) corresponding to the left-hand side of the shaded area. Below this temperature patterns become stationary (the sequence of stationary patterns at low temperatures is described elsewhere). Fig. 4.1 (right) shows the transition from the high-temperature contrastless paramagnetic phase (top of the image) to the stationary stripe phase at lower temperatures (bottom of the image). The temperature range covered in the image of Fig. 4.1 (right) is about 3 K, the image being taken approximately at room temperature. Some of the peculiar features of the stripe formation indicative of stripe mobility are colored in the image for convenience. In the lower section of the image, corresponding to lower temperatures, stripe sections are suddenly terminated along one sharp horizontal line. In the next line they continue albeit displaced. The initial stage of stripe formation consists of a sequence of such displacements, systematically observed at horizontal lines. As a result of these displacements, the stripe phase that forms just below T_c^0 appears blurred. Toward the bottom of the image, the continuous sections tend to become longer; the stationary stripe pattern visible well below T_c^0 forms.

Figure 4.2: (left): $40 \times 15 \mu m^2$ topographic (a), in-plane (b,d and e) and out-of-plane (c) polarization images of a Co STM tip. The black-and white contrast in the in-plane polarization images corresponds to left and right magnetization along the tip axis. The gray areas are either magnetized perpendicular to the tip axis or have no remanent magnetization. Image (b) shows the magnetization of the tip after heating in UHV, (d) after applying an external field of 750 Oe along the tip axis, and (e) after the reversal of the applied field. The corresponding out-of-plane polarization image (c) shows no contrast. We conclude that the tip consists mostly of magnetic segments with alternating magnetization along the tip axis. (right): $50 \mu m$ wide SEMPA out-of-plane polarization image of 2-ML-thick Fe element on Cu(100). Two elements of the sample were prepared to have opposite magnetization by selective switching of one element in an external field (a). Afterwards, the tip is approached to the left element and moved from A to B. In Fig. 4.2 (right b) it is shown that the magnetization of this element has been switched.

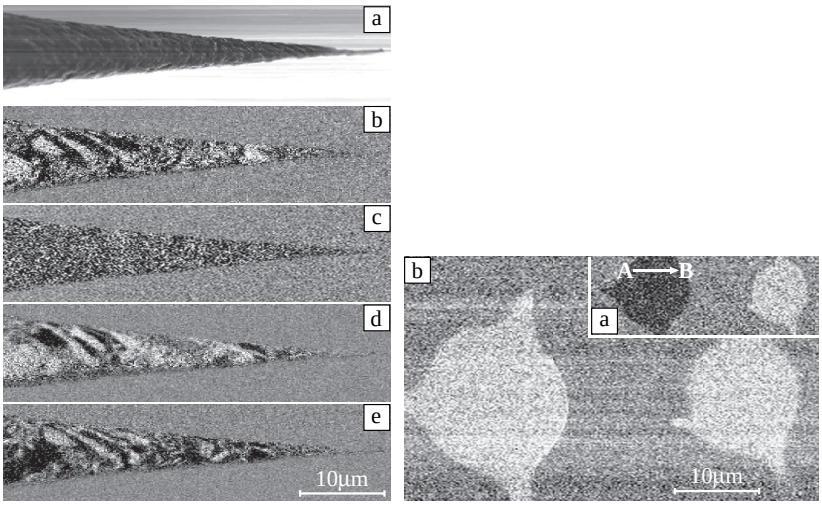

4.2 Quasicrystal surfaces

In molecular-beam epitaxy, the lattice mismatch between the substrate and the adsorbate dictates the growth mode of the surface film. A small mismatch leads to pseudomorphic growth, while a larger mismatch results in a domain structure of the growing film, which often consists of self-size selecting islands possibly leading to the formation of quantum dots. The choice of quasicrystals as a substrate material certainly produces such nanometric islands, because on a quasicrystalline surface atoms are found in an aperiodic distribution enhancing the lattice mismatch. Quasicrystals lack periodicity, but possess long-range orientational order with fivefold or tenfold point-group symmetries that cannot occur in ordinary crystals. Therefore, the structural transition on the atomic scale at the interface where an ordinary crystal and a quasicrystal intersect cannot maintain conditions for epitaxial growth on a global scale. We have used well-prepared and characterized surfaces of icosahedral (i-) Al-Pd-Mn (AlPdMn) and decagonal (d-) Al-Co-Ni (AlCoNi) quasicrystals to serve as substrates for growing different magnetic and nonmagnetic metals as well as semiconductors.

For structural investigations we employ low-energy electron diffraction (LEED) and secondary-electron imaging (SEI). Electron-diffraction patterns reveal the size and symmetry of the surface unit cell in the reciprocal space, while the observed SEI patterns represent a central projection of the real-space atomic arrangement in a near-surface region. Electronic structure is investigated using photoemission and electron-energy-loss spectroscopy. Information about the chemical state and concentration at the surface is obtained in Auger electron spectroscopy.

4.2.1 Crystal-quasicrystal interfaces. Electronic structure

J.-N. Longchamp, Y. Weisskopf, M. Erbudak (with C. Carbone and P. Moras, Elettra)

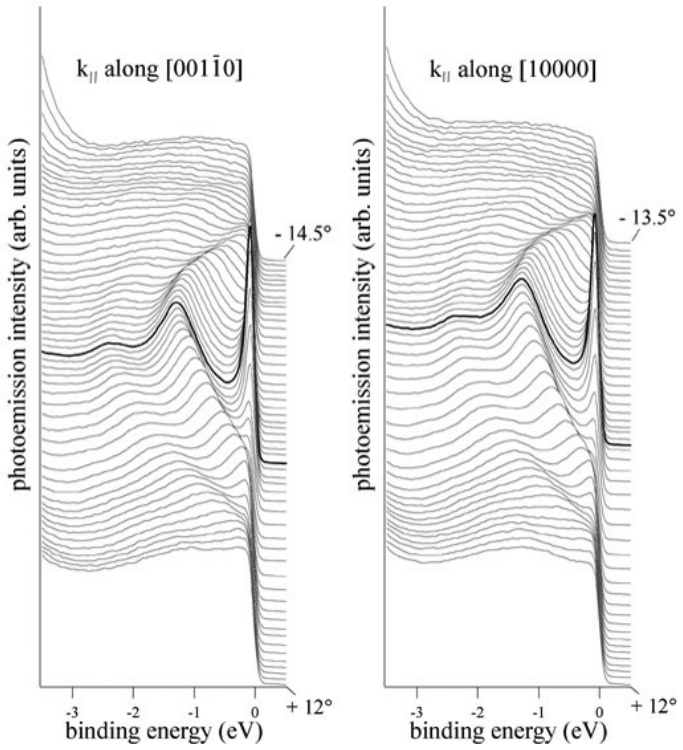

Figure 4.3: Energy-distribution curves for 1.7 nm of Ag on d-AlCoNi, along two major quasicrystalline directions.

Two-dimensional quantum-well states (QWS) with a discrete energy spectrum are formed in thin metal films that are electronically isolated from the environment. If the states, however, can couple to the substrate wave functions across the interface, the resulting hybridization causes delocalization of the QWS. Thus, such states are efficient probes of the interactions between the film and the substrate.

We have produced crystal-quasicrystal interfaces by growing Ag films on d-AlCoNi and i-AlPdMn. By virtue of self-organization processes at quasiperiodic surfaces, a multidomain face-centered cubic structure is formed with (111) terminations having a grain size of 5 ± 1 nm.

Angle-resolved photoemission from the *sp*-valence levels of Ag confirms the formation of QWS due to confinement along the direction normal to the film plane. We observe that the valence levels exhibit a highly dispersive character inspite of the noncrystalline rotational order of the nanoscale metal islands. This suggest that domain boundaries in the film morphology have negligible influence on the electronic states, and the local crystalline arrangement dominates over the microscopic island distribution.

It is also observed that QWS are distributed over a wide binding-energy range and appear to be insensitive to specific features of the density of states of the quasicrystalline substrates, which act as an highly reflecting barrier for Ag electrons. This is an expected result because Bloch waves in the Ag layer possess point-group symmetries derived from the crystalline atomic arrangement. In contrast, critical wave functions of the quasicrystal obey to crystal-forbidden symmetries. Electronic coupling is, therefore, strictly forbidden due to the orthogonality of the states across the interface for every energy and wave vector.

According to our interpretation, no electronic communication takes place across the interface even though it would energetically be possible. Hence, following this conclusion and without resorting to the so-called pseudo gap, no tunneling current would flow across a junction even though electronic states are present at the Fermi level.

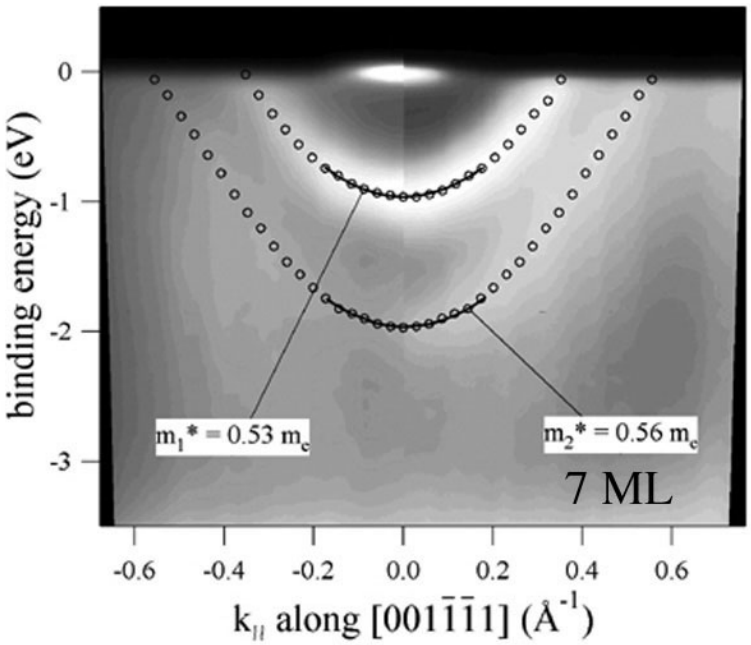

Figure 4.4: Intensity plot measured along a twofold-symmetry direction of the i-AlPdMn fo 1.7 nm of Ag.

4.2.2 Fe and Ni on i-AlPdMn. Atomic structure

Y. Weisskopf, S. Burkardt, M. Erbudak, J.-N. Longchamp

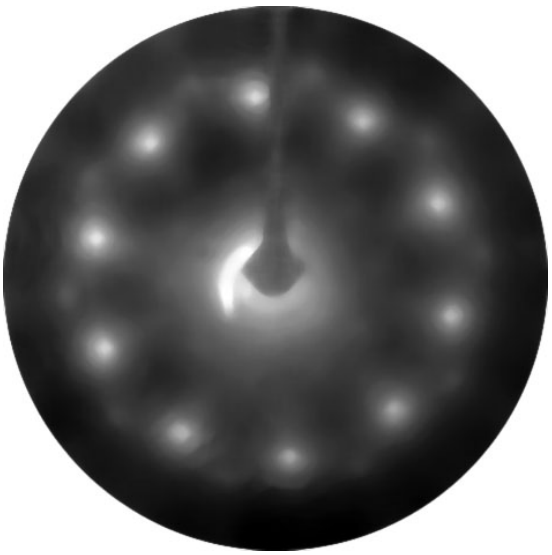

Figure 4.5: Electron diffraction pattern at 125 eV from 1.9 monolayers of Ni in the cubic 5 domain structure grown on i-AlPdMn.

CsCl-type, nm-size domains with a lattice constant of approximately 0.29 nm can be generated by the deposition of Fe and Ni on the fivefold-symmetry surface of i-AlPdMn. Fe and Ni intermix with the substrate surface at the initial stage of growth forming thereby unordered surface layers. During further deposition, Al migrates from the substrate to Al-Ni and Al-Fe layers which grow on the layers formed by intermixing and consist of domains which possess a CsCl-type structure, expose their (110) faces, and are rotated by 72° with respect to each other. On the CsCl-type domains, body-centred cubic Fe and Ni domains grow. Removing relatively low coverages of Fe or Ni by sputtering reveals 5 distinct CsCl-type AlPd domains exposing their (113) faces and rotated by 72° with respect to each other, while the structural CsCl(110) character of the interface, established for higher coverages, favors the formation of domains exposing their (110) faces during sputtering. In all cases, the orientational relationship between domains and the quasicrystal is determined by the optimum matching of the CsCl structure with the periodic, discrete average structure of the quasicrystal. Accordingly, the domains possess well-defined orientations mediated by the substrate structure. These findings demonstrate the affinity of the quasicrystal structure to the cubic structure. For sufficiently high deposits, Ni domains exhibit a surface structure which consists of 1 dimensional (D) rows and Fe domains show a small tilt. In-plane magnetic ordering is observed for Fe domains, while Ni domains exhibit out-of-plane magnetic ordering. Intermixing results in a non-magnetic interface region.

4.2.3 Si on i-AlPdMn. A new phase

J.-N. Longchamp, M. Erbudak, Y. Weisskopf

Vacuum deposition of Si on the pentagonal surface of AlPdMn in excess of one monolayer leads to the growth of an amorphous phase. LEED signal from the quasicrystalline substrate gradually diminishes with film thickness and the SEI pattern shows no new structure originating from the growing Si layers. This unordered growth is observed for substrate temperatures of $250 - 370$ K. Above 370 K, AES shows a marked decrease in the Si signal due to diffusion into the substrate and, simultaneously, a fivefold-symmetric LEED pattern evolves similar to that obtained from the clean surface. A similar diffraction pattern is obtained by deposition of 2 Si monolayers onto the substrate kept at room temperature and subsequently annealed to 380 K.

These observations could be interpreted as a complete diffusion of Si into deep bulk layers of the substrate leaving the quasicrystalline order in tact at the surface. However, quantitative AES analysis indicates the formation of a new quasicrystalline Al-Si-Pd-Mn phase at the surface by absorption of Si into the surface layers and substitution of Al by Si. In this new icosahedral phase the surface concentration is shifted from 85% Al to 38% Al and 47% Si.

4.2.4 Generation of quasicrystalline structures

P. Can, P. Milas (Bogaziçi University)

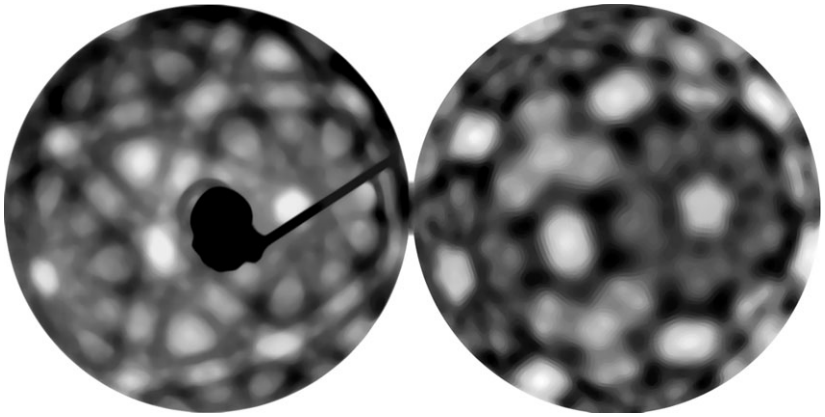

Figure 4.6: Secondary-electron pattern (left) is compared with calculations (right) based on single-scattering approximation of electrons applied to the quasicrystalline lattice generated here.

Three models have been proposed to account for the structure of quasicrystals. The Penrose model suggests that quasicrystals are composed of two or more unit cells that fit together according to specific rules. The glass model suggests that clusters of atoms join in a somewhat random way determined by local interactions. The random-tiling model, which combines some of the best features of the other two models, suggests that the strict matching rules of the Penrose model need not be obeyed as long as local interactions leave no gaps in the structure.

We have devised two algorithms for calculating quasiperiodic lattices by the strip projection method. For the 2D algorithm a 5D simple cubic integral lattice with a unit lattice constant is employed as the root lattice with a rhombic icosahedron as the projection window. For the 3D case, a 6D simple cubic integral with a unit lattice constant is taken as root lattice with a rhombic triacontahedron as the projection window.

We have applied single-scattering cluster calculations on the generated quasiperiodic lattice with the aim of reproducing the SEI patterns obtained from the main symmetry axes of i-AlPdMn. Apart from contrast features with a considerable multiple-electron-scattering contribution, the agreement between the experimental SEI patterns and the simulations are remarkably good. Since we only consider a statistical distribution of different atoms in the simulation, the agreement implies that the chemical order in the near-surface region of the sample does not produce an appreciable change in the contrast features of the secondary-electron pattern.

4.3 Epitaxial IV-VI narrow-gap semiconductor layers

M. Arnold, F. Felder, M. Rahim, A.N. Tiwari, and H. Zogg; www.tfp.ethz.ch

Narrow gap lead chalcogenide (IV-VI) layers like PbX, $Pb_{1-x}Sn_xX$, $Pb_{1-y}Eu_yX$ and $Pb_{1-y}Sr_yX$ (X=Te, Se) are investigated for applications and basic research. The band gaps of the active infrared layers are between 0.1 and 0.25 eV (corresponding to wavelengths in the mid-IR range). Larger band gaps are realised with larger y values for the cladding $Pb_{1-y}Eu_yX$ and $Pb_{1-y}Sr_yX$ layers. All layers are grown by solid source molecular beam epitaxy (MBE) onto Si(111)-substrates by employing a CaF2 buffer layer, or onto BaF2(111) substrates. The layers are heavily lattice- and (for Si-substrates) thermal-expansion mismatched. Misfit and threading dislocations therefore are present. However, lead-chalcogenides are fault tolerant. Even with threading dislocations densities in the 10^7 cm^{-2} to 10^8 cm^{-2} range, optoelectronic devices with reasonable quality are obtained. The minority carrier lifetimes τ are determined by the density of the threading dislocations ρ, $\tau \sim 1/\rho$.

We have realized photovoltaic infrared detectors and applied them to fabricate complete heteroepitaxial monolithic two-dimensional Infrared Focal Plane Arrays (2d IR-FPA) on active Si-substrates. As IR-sources, we fabricated optically pumped edge-emitting mid-IR lasers, again on Si-substrates.

In addition, it is easy to fabricate Bragg mirrors with very high reflectivity over a broad spectral range. These mirrors consist of quarter wavelength stacks of layers with alternating high (n_H) and low (n_L) refractive indices. With the materials typically used, EuSe (n_L=2.4) or BaF2 (n_L=1.4) with low indices, PbX or $Pb_{1-x}Sn_xX$ ($n_H > 4$) with high indices, two to three quarter wavelength n_L/n_H pairs suffice to obtain reflection coefficients $>99\%$. With such mirrors, complete Fabry-Perot cavities can be grown.

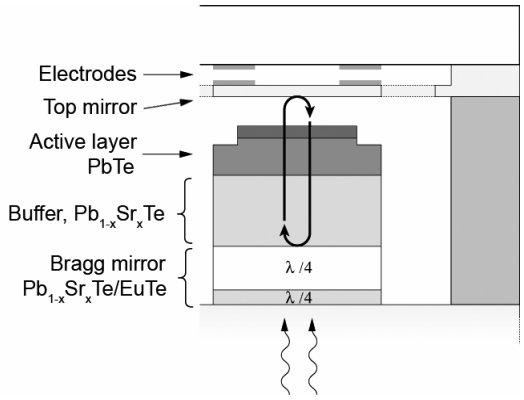

Figure 4.7: Design of a tunable mid-infrared RCED with a moveable electro statically actuated top mirror.

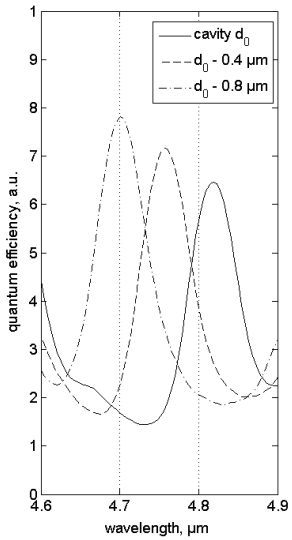

Figure 4.8: Measured sensitivity spectrum of a tunable RCED at three different distances, d_0, $d_0 - 0.4\ \mu$m and $d_0 - 0.8\ \mu$m, of the top mirror (95 K).

By placing the active detector layer inside the cavity, a **resonant cavity enhanced detector (RCED**) is obtained. It is sensitive at the resonance wavelengths only where it exhibits a high quantum efficiency. The positions of the resonances are determined by the length of the cavity. With a monolithic approach, this length is determined by the optical path inside the cavity and is fixed. To obtain a tunable cavity length, the top mirror is arranged on a free standing membrane whose distance with respect to the second bottom mirror can be varied by e.g. micromechanical means (Fig. 4.7). Such an arrangement forms a micro infrared spectrometer. Fig. 4.9 shows calculated results of the wavelength dependent peak quantum efficiency as a function of the position of the top mirror. A first design was realised to demonstrate the principle. A preliminary spectral response for two different cavity lengths is shown in Fig. 4.8.

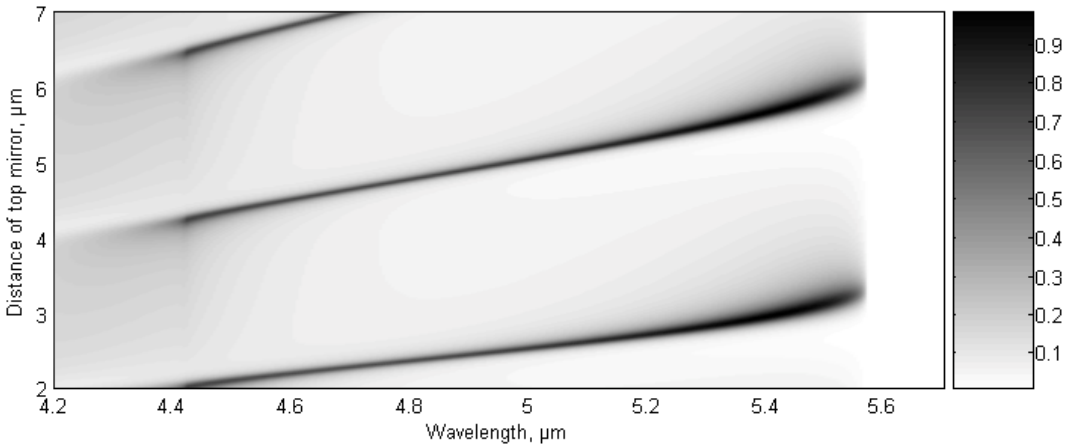

Figure 4.9: Simulated quantum efficiency of a tunable PbTe RCED as a function of wavelength and mirror distance.

Another application of a Fabry-Perot cavity with a tunable top mirror is the **vertical *external* cavity surface emitting laser** (V*E*CSEL). Monolithic vertical cavity surface emitting lasers (VCSELs) have become technologically important up to the near-IR range because of their easy planar processing, and their small beam divergence which results in a good beam quality. A VECSEL is defined as half VCSEL with an external curved mirror. The cavity length is tunable by moving the external mirror, which allows the tuning of the output wavelength over quite a broad range.

We realized the first VECSEL for the mid-IR range by using IV-VI narrow bandgap materials. As already stated, high reflection Bragg mirrors are easily obtained with IV-VI compounds. The active layer of the VECSEL simply consists of a few μm thick PbTe layer. It is pumped optically with a commercial laser diode with 1.55 μm wavelength (Fig. 4.10). The maximum emission wavelength at 150K operation temperature is 4.96 μm with a pump power slightly above threshold. Here, the spectrum is nearly monomode (Fig. 4.11, right curve). The wavelength shifts to shorter values at higher pump-powers due to heating of the active layer (Fig. 4.11, right curve).

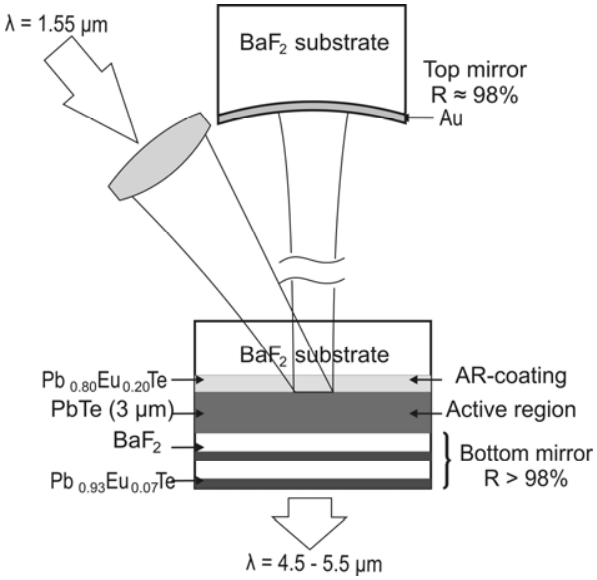

Figure 4.10: Schematic representation of the VECSEL.

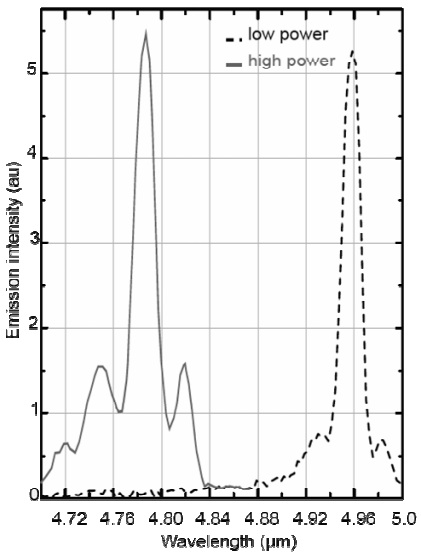

Figure 4.11: Spectra of VECSEL at 150 K. Right curve: One dominating mode at low pumping power; left curve: Multimode emission at higher pumping power.

4.4 Thin-film solar cells based on Cu(In,Ga)Se_2 compound semiconductors

D. Brémaud, S. Bücheler, A. Chirila, K. Ernits, R. Verma, M. Kaelin, H. Zogg, and A.N.Tiwari; www.tfp.ethz.ch

Safe, cheap, abundant, renewable, and environment-friendly generation of electricity is of considerable interest for our society. Thin-film solar cell technology based on the polycrystalline compound semiconductor Cu(In,Ga)Se_2 (usually abbreviated as "CIGS") is a very promising solution for this task. New cell concepts to improve the stability and efficiency are among further projects.

Alternative Transparent Back Contacts

Tandem solar cells (two or more stacked solar cells) are important to further improve the photovoltaic conversion efficiency by better utilization of the solar spectrum. CIGS for such applications require transparent electrical back contacts. Therefore, the conventional Mo contact for CIGS has to be replaced with an appropriate transparent conducting layer. We have developed CIGS solar cells with a transparent conductive oxide, ITO, as back contact. To facilitate or allow the formation of an ohmic contact a very thin $MoSe_2$ interface layer has been applied between ITO and CIGS to obtain carrier transport through tunneling. Therefore, Mo layers have been sputtered on the ITO and selenized before the deposition of CIGS. The $MoSe_2$ layers have been investigated to determine the thickness of $MoSe_2$ and the converted ratio of Mo. CIGS layers were then grown by evaporation of elemental Cu, In, Ga, and Se, at a max. temperature of $450°C$. Because the used alternative back contacts act as barrier and inhibit the Na diffusion from the glass substrate, we have added Na separately using a post deposition treatment. The properties of CIGS layers with and without Na have been investigated by different methods (SEM, SIMS, EDX). The photovoltaic properties of small area solar cells were characterized with I-V and quantum efficiency measurements. Under simulated AM1.5 standard test conditions an efficiency of 11.9% (V_{oc} = 603 mV, J_{sc} = 31.4 mA/cm^2, FF= 63.1%, total area = 0.6 cm^2, no ARC) with ITO back contacts has been achieved on SLG substrates.

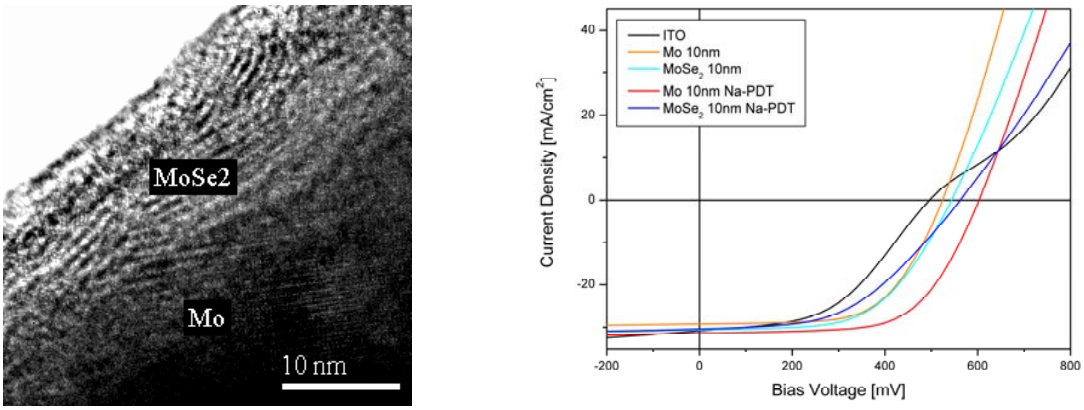

Figure 4.12: *Left:* High resolution transmission electron microscope (HRTEM) image of thin Mo-layer showing formation of $MoSe_2$. *Right:* J-V measurements showing the improving effect of $MoSe_2$-layer and Na post deposition treatment (Na-PDT)

Ultrasonic sprayed In_xS_y

In_2S_3 films produced by ultrasonic spray pyrolysis (USP) method are developed as an alternative buffer-layer for CIGS solar cells. We have optimized the In_2S_3 spray process parameters and investigated the properties of USP-In_2S_3 layers grown at different substrate temperatures and spray solution concentrations. Thickness measurements showed that the film growth rate increases with substrate temperature and precursor concentration in the solution. Optical transmission decreased with higher substrate temperature and lower thiourea concentration in the spray solution. Scanning Electron Microscopy (SEM) images showed that continuous thin In_2S_3 buffer-layers have been grown on glass substrates. X-ray Diffraction (XRD) and X-ray Photoelectron Spectroscopy (XPS) measurements revealed that mainly In_2S_3 phases

were formed in the films. We achieved solar cell efficiencies up to 9.5% for CIGS/In_2S_3 cells after light soaking, compared to 12.9% efficiency for CIGS cell with a standard chemical bath deposited CdS buffer-layer.

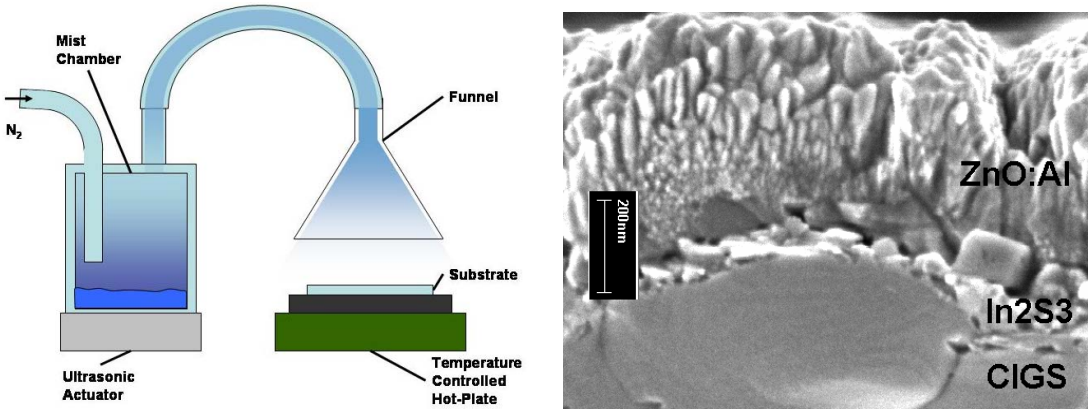

Figure 4.13: *Left:* Schematic of the USP system; mist of the solution generated by the ultrasonic actuator is transported through a tube and the funnel for a spray. *Right:* SEM cross-section image of the CIGS solar cell with USP-In_2S_3 as a buffer-layer.

Upscaling of flexible CIGS solar cells

Flexible solar cells on polyimide foil of 5×5 cm^2 have been developed using vacuum evaporated CIGS layer and we have achieved conversion efficiencies up to 14.1%, which is a record for any kind of solar cell grown on polymer foil. We have started the upscaling of the deposition process to grow layers on 30×30 cm^2 size substrates by in-house assembly of a CIGS deposition system. Development of large area flexible solar cells and mini-modules has started, and as a proof of concept flexible mini-modules to run small ventilator-fans have been made. A mini-module with a 16 cm^2 total area efficiency of 7.9% has been developed. The factors for further efficiency improvements were identified although this result is already among the most efficient solar modules produced on polymer foil.

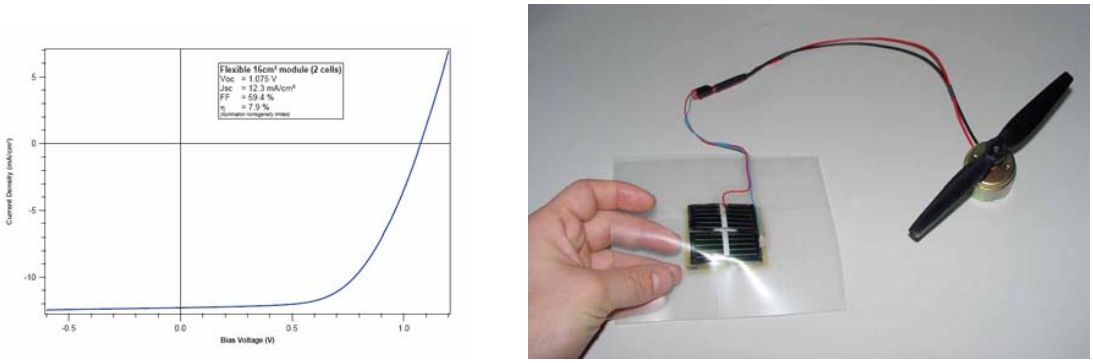

Figure 4.14: *Left:* J-V curve of 16 cm^2 mini-module obtained by connection of two large area cells with metal grids. *Right:* Flexible mini-module to run a ventilator-fan.

Chapter 5

Quantum devices

(http://qudev.ethz.ch/)

Head
Prof. Dr. Andreas Wallraff

Academic Staff
Romeo Bianchetti
Alfredo Bismuto
Will Braff
Dr. Parisa Fallahi
Johannes Fink
Martin Göppl
Dr. Peter Leek
Jonah Waissman

Technical Staff
Hansrudolf Aeschbach

Administrative Staff
Gaby Strahm

In spring 2006, we have started up a new research group at ETH Zurich to study quantum properties of novel micro- and nano-structured electronic devices and their interaction with classical and quantum electromagnetic fields. In its starting year the research group included two postdoctoral associates, two graduate students, one masters student, three summer interns, a technician and a secretary, see group photograph 5.1.

Figure 5.1: Group photograph summer 2006. Top row from the left: Hansrudolf Aeschbach, Johannes Fink, Will Braff, Martin Göppl, Jonah Waissman, Andreas Wallraff. Bottom row: Gaby Strahm, Romeo Bianchetti, Peter Leek, Parisa Fallahi

The research focus of the Quantum devices group is positioned at the intersections of mesoscopic condensed matter physics, atomic physics and quantum optics, where physical systems with intriguing properties and exciting applications can be realized. In our new lab quantum electronic circuits are operated in regimes previously only accessible in atomic physics and quantum optics. In one of our main activities we investigate the fundamentals of the interaction of matter and light in the context of *cavity quantum electrodynamics* (QED). The realization of strong coupling between a single solid state quantum two-level system (a qubit) and a single mode of a quantized electromagnetic field, allows us to study interactions on the single photon level, where changes in the state of an individual quantum system give rise to a large nonlinear response of the coupled system. In this novel regime, now also referred to as *circuit quantum electrodynamics*, the physics of open solid state quantum systems is investigated in particular in the view of coherence and decoherence. Open quantum systems are an ideal setting to study the interface between the classical and the quantum world, shedding light on the quantum measurement process and its back-action on the quantum system under test. Such matters are also of great importance in *quantum information science*. In this field of activity we aim at controlling the dynamics of collections of quantum systems to investigate complex physical and computational problems. In our lab, the coherent dynamics of superconducting quantum electronic circuits are investigated to test basic concepts of quantum information processing. Another direction that we explore is applications of *microwave quantum electronic circuits* as sensitive, possibly quantum limited, nano-electronic measurement devices and detectors.

5.1 Circuit quantum electrodynamics

Researchers in many fields of physics have envisaged coupling a single quantum two-level system coherently to a quantum harmonic oscillator. Until recently, this feat had only been achieved in the realm of atomic physics and quantum optics, where such experiments have been at the focus of research in the past decade. In a recent experimental

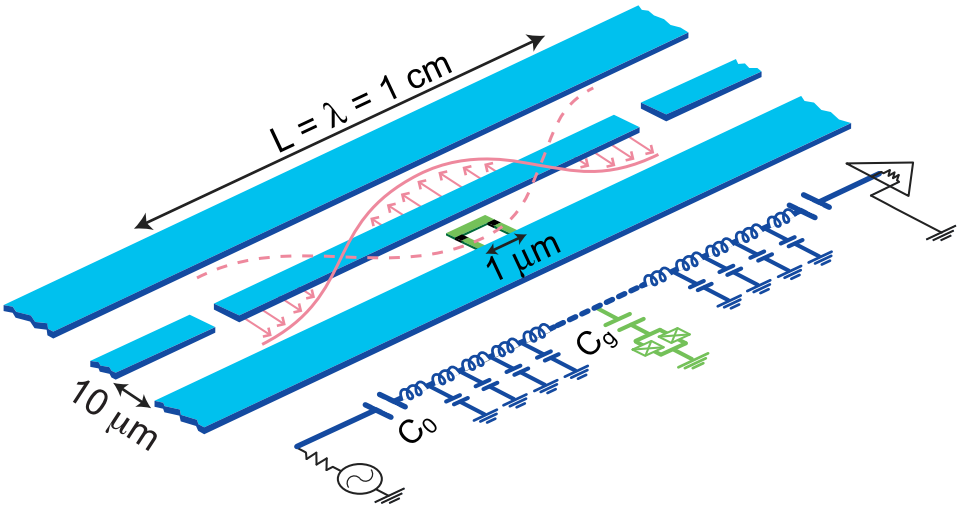

Figure 5.2: Schematic view of a Cooper pair box - a quantum mechanical two level system - (shown in green) coupled to a transmission line resonator (blue) in the circuit quantum electrodynamics architecture [2].

breakthrough, it was demonstrated for the first time in an experiment that a solid-state nano-electronic superconducting circuit, acting as an artificial atom, can be coupled coherently to a single microwave photon stored in an on-chip cavity [1]. The success of this approach is based on the ability to design and fabricate mesoscopic solid-state two-level systems with controllable properties, such as large effective electric dipole moments ($d \sim 10^4\, ea_0$), and to develop 1D on-chip cavities with small mode volumes and very large vacuum electric fields ($E_0 \sim 0.1\,\mathrm{V/m}$) leading to large controllable electric dipole interactions. A sketch of a typical circuit QED sample configuration is shown in Fig. 5.2. Key aspects are also large bandwidth and low noise microwave techniques which we have developed for experiments with mesoscopic devices at low temperatures. Mastering these techniques, it is possible to realize the new paradigm of circuit quantum electrodynamics in which we plan to address fundamental quantum optics questions and go beyond the current state of the art of atomic cavity QED. Because of the strong interactions of matter and light in solids coherent quantum optical effects can be observed in circuit QED even though the coupling to environmental degrees of freedom leading to decoherence is much larger in a solid state environment than in atomic systems.

[1] A. Wallraff et al., *Circuit quantum electrodynamics: Coherent coupling of a single photon to a Cooper pair box*, Nature (London) **431**, 162 (2004).
[2] A. Blais, R.-S. Huang, A. Wallraff, S. M. Girvin, and R. J. Schoelkopf, *Cavity quantum electrodynamics for superconducting electrical circuits: an architecture for quantum computation*, Phys. Rev. A **69**, 062320 (2004).

5.2 Quantum information processing

Circuit quantum electrodynamics provides an ideal setting for implementing elements of a superconducting quantum information processor. In this architecture qubits are efficiently controlled and measured using electromagnetic fields at microwave frequencies. Quantum information can be converted from stationary qubits into photons that can be used for mediating interactions between distant qubits. These photons may even be used for coupling to distant quantum bits realized in an altogether different technology allowing for the formation of novel hybrid systems. In our first measurements we have found coherence times of several hundred nanoseconds in a charge qubit effectively isolated from its environment and have realized a high visibility quantum non-demolition (QND) dispersive read-out of an individual qubit. We will further analyze and identify sources of decoherence with the aim to eliminate them to a level such that error correction becomes feasible. This enables coupling of multiple qubits using the resonator as a non-local coupling bus which will allow for the implementation of logical gates and first simple quantum algorithms. These attractive features make this architecture a prominent candidate for addressing quantum computation problems beyond the single qubit level using techniques that are also applicable to other approaches for solid state quantum information processing.

5.3 Microwave quantum electronic circuits

Research on mesoscopic devices, such as quantum dots, nanowires, micro or nano mechanical systems, nanotubes or even single molecules can benefit enormously from the use of fast and sensitive measurement techniques at RF and microwave frequencies. Probing ac-properties of such systems, the measurement bandwidth can be increased drastically, enabling time-resolved experiments on shorter time scales with larger signal to noise ratios than in traditional dc- or low frequency transport measurements. Coupling sub-micron or nano-scale devices, that typically have high impedances and large wiring stray capacitances limiting the measurement bandwidth, to a high frequency resonant circuit, such as a cavity or a lumped LC circuit, allows one to probe the conductance, capacitance or inductance of the device at microwave frequencies. For example, the ground state properties and the excitation spectrum of quantum dots or nanotubes can be inferred from a susceptibility measurement instead of residing to dc transport measurements. These measurements have the additional advantage that capacitive or inductive coupling of the device under test can be realized in a less perturbing way than by attaching dc contacts to the device under test. In recent years, similar techniques have been demonstrated at lower frequencies (e.g. the radio frequency single electron transistor) and are currently implemented in some of the highest sensitivity measurements performed with mesoscopic devices (e.g. in nano mechanical resonators). These techniques also benefit from the available low-noise cryogenic amplifier technologies, which have very well characterized noise performance. In our lab, use of such techniques will bring novel mesoscopic experiments on short time scales at large signal to noise ratios into range.

5.4 Lab construction

One of the main tasks in 2006 was the design and construction of a lab space and the subsequent installation of experimental equipment that would enable low-noise, sensitive measurements on nanosecond time scales on superconducting quantum electronic circuits at millikelvin temperatures. In a first step we planned and realized the infrastructure required for the installation of a 10 mK high-access dilution refrigerator for low noise electrical measurements. The building vibration spectrum and the electromagnetic environment at the installation site were carefully analyzed and necessary precautions were taken. The lab renovations, including the creation of a pit 2 m x 1 m x 2.5 m in size required for installing the cryostat, were completed by summer 2006. Design, manufacturing and mounting of lifting equipment, support-frames, vacuum tubes, vibration isolations and vacuum pumps was completed well before the delivery of the dilution refrigerator system in October 2006. The engineering office and the machine shop of the

Figure 5.3: The experimental setup consisting of a dilution refrigerator wired for low noise and high frequency measurements and a rack of microwave electronic equipment including sources, up and down converters, digitizers and pulse generators.

physics department were of great help in this period. In November 2006 the installation and test run of the dilution refrigerator system was completed successfully. A low base temperature of $\sim$5 mK was reached in the first cool-down proving that the refrigerators mounting scheme and pump line configuration was designed to allow full performance of the system.

In parallel with the efforts in the installation of the low temperature system, the microwave measurement setup required for circuit QED experiments was planned, realized and tested. Also, custom made electromagnetic filters were developed and installed. The complete microwave wiring inside and outside of the cryostat was designed in order to provide a circuit with optimum performance at microwave frequencies while considering thermal aspects of the cabling in the ultra-low temperature environment. In particular stainless steel coaxial lines from room temperature to the cryogenic environment were installed and a stable voltage supply for an ultra low noise microwave amplifier was realized. The setup, test and synchronization of the data acquisition system, including microwave pulse generation and sampling with ns-resolution was realized. The efforts were rewarded, when we were able to perform first successful measurements on a superconducting qubit circuit in December 2006.

5.5 Sample fabrication

We have developed a robust photolithography process for the fabrication of superconducting microwave resonators in coplanar geometry, to 2 μm resolution, using the facilities available in the ETH clean-room FIRST. A negative resist process provides us with excellent resolution and consistent undercut resist profile, see Fig. 5.4(a). Subsequent electron beam evaporation and lift-off of a 200 nm Al film realizes the resonator, see Fig. 5.4(b). The quality factor of the resonators are controlled using interdigitated input and output coupling capacitors, see Fig. 5.4(c). This approach allows us to fabricate a variety of high quality resonant circuits for circuit QED experiments as well as for other projects.

We have also completed first steps towards the implementation of e-beam lithography and shadow evaporation techniques required for the fabrication of quantum electronic circuits based on sub-micron $\mathrm{Al/Al_xO_y/Al}$ superconducting tunnel junctions. For that purpose long and narrow freestanding resist bridges were fabricated, see Fig. 5.4(d), using a bi-layer electron-beam resist (PMMA/MAA) with controlled undercut. The upper layer (PMMA 950k) ($\sim$ 60 nm thick) serves as a mask for the subsequent evaporation of Al while the lower layer (PMMA/MAA) ($\sim$ 600 nm thick)

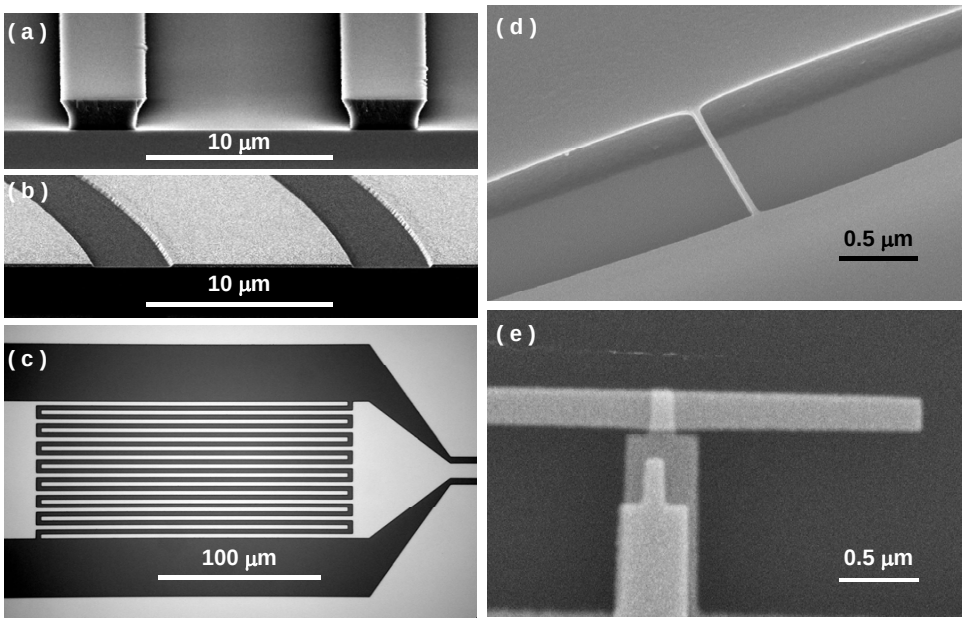

Figure 5.4: (a) Resist Profile. (b) Evaporated Al thin film in coplanar waveguide geometry. (c) Interdigitated capacitor at the input of a coplanar resonator. (d) Freestanding resist bridge for fabrication of Josephson junctions. (e) Josephson junction test structure.

serves as spacer. Josephson tunnel junctions are fabricated by two subsequent evaporations of Al under different angles with a oxidation step in between, see Fig. 5.4(e). The junction size and the thickness of the oxide layer determine the Josephson and charging energies of the structure. Accurate control of these parameters is crucial for realizing devices based on Josephson tunnel junctions.

5.6 First circuit QED results at ETH Zurich

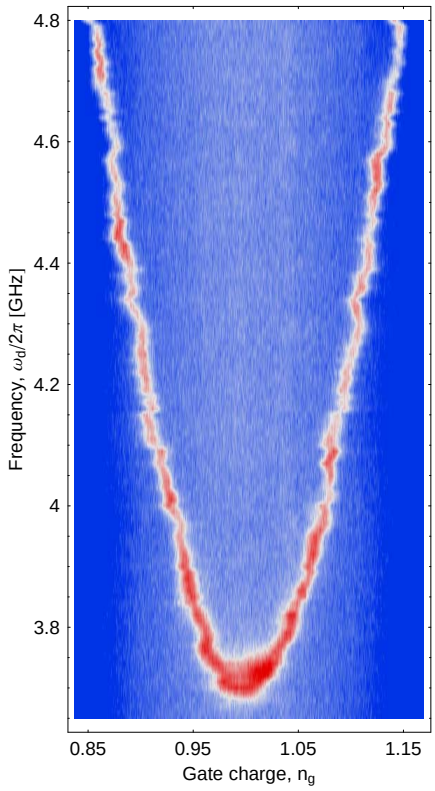

Figure 5.5: Spectroscopic measurement of the energy level separation in a Cooper pair box (CPB).

In December 2006 we were able to perform first low temperature measurements of a circuit QED sample. The device, a Cooper pair box coupled to a transmission line cavity was fabricated at Yale University. Devices in the circuit QED architecture are extremely interesting for applications in quantum information processing. Among its many attractive features, circuit QED provides an ideal setting to effectively control the coupling of qubits, i.e. the quantum two-level systems which carry the information, to their electromagnetic environment. Making use of a cavity detuned from the qubit, we isolate the qubit from its environment to achieve energy relaxation times on the order of $T_1 \sim 5\,\mu$s and coherence times of $T_2 \sim 500\,$ns that could be measured with both spectroscopic and time resolved techniques. These are among the longest coherence times demonstrated so far for charge qubits in particular and for superconducting qubits in general. At the origin of these long coherence time is a simple and clean design of the microwave circuit into which qubits are embedded and the use of a minimal set of well characterized materials for sample fabrication. Another key ingredient is our ability to perform sensitive and efficient measurements of mesoscopic solid state devices at microwave frequencies and low temperatures.

While isolating qubits from the environment, the cavity provides at the same time strong and controlled coupling of qubits to a single mode of a quantum electromagnetic field. This field can be used to simultaneously control and readout the qubit state and also couple multiple qubits to each other. The off-resonant strong coupling between the qubit and the resonator can be used to perform a quantum non-demolition (QND) dispersive readout of the qubit state, see Fig. 5.5. The measurement signal, a phase shift of microwaves transmitted through the cavity dispersively coupled to the CPB, is color coded.

We have also performed first time-resolved measurements of the qubit quantum state with high visibility by mapping out the dispersive shift of the cavity frequency in response to a state change of the qubit induced by a short resonant microwave pulse. For continuous measurements, populating the resonators with only a few photons at a time, we understand the temporal response of the cavity field to a qubit state change quantitatively. This allowed us to determine the population of the excited qubit state. In particular, we have already been able to perform measurements of Rabi oscillations, see Fig. 5.6, with a good visibility. This indicates that we are able to control the qubit state well and that we can determine the qubit state from the dispersive interaction of the qubit with the measurement field.

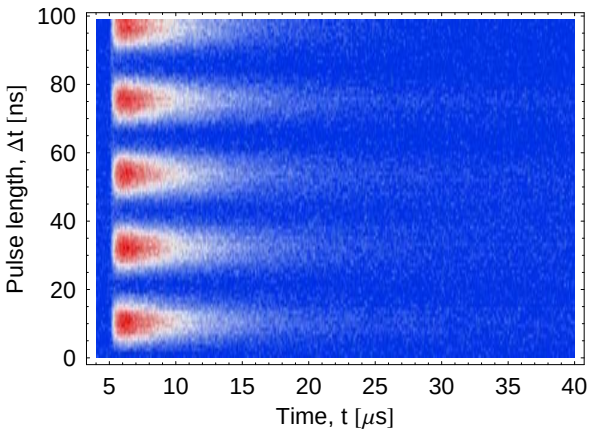

Figure 5.6: Measurements of Rabi oscillations of a Cooper pair box at a fixed microwave power vs. pulse length.

Having successfully completed these first measurements we are confident to be able realize a successful next generation of circuit QED experiments in 2007.

Chapter 6

Publications

T. Akiyama, K. Suter, N. F. de Rooij, A. Baumgartner, A. Gildemeister, T. Ihn, K. Ensslin and U. Staufer
Scanning Probe with Tuning Fork Sensor, Microfabricated Silicon Cantilever and Conductive Tip for Microscopy at Cryogenic Temperature
Jap. J. Appl. Phys. 45, 1992 (2006)

C.H. Back, D. Pescia and M. Buess
Vortex Dynamics
Topics Appl. Phys., Spin Dynamics in Confined Magnetic Structures III, B. Edited by Hillebrands, A. Thiaville, 101, 137 (2006), Springer Verlag, Berlin Heidelberg

A. Baumgartner, T. Ihn, K. Ensslin, G. Papp and F. Peeters, K. Maranowski and A. C. Gossard
Classical Hall effect in scanning gate experiments
Phys. Rev. B 74, 165426 (2006)

A. Bilusic, A. Smontara, J. Dolinsek, P. McGuiness, H.R. Ott
Phonon scattering in quasicrystalline i-$Al_{72}Pd_{19.5}Mn_{8.5}$: A study of the low-temperature thermal conductivity
Journal of Alloys and Compounds, online available, 7th July (2006)

D. Brémaud, D. Rudmann, H.M. Upadhyaya, P. Liska, K.R. Thampi, M. Grätzel, A. N. Tiwari
Development of high efficiency nanocrystalline dye-sensitised / Cu(In,Ga)Se_2 tandem solar cells
Proceedings 21st European Photovoltaic Solar Energy Conference, Dresden, 263-266 (2006)

M. Brühwiler, S.M. Kazakov, J. Karpinski and B. Batlogg
Large mass enhancement in $RbOs_2O_6$
Physica B: Condensed Matter, Volumes 378-380, 880-881, (2006)

M. Brühwiler, B. Batlogg, S.M. Kazakov, Ch. Niedermayer and J. Karpinski
Na_xCoO_2: Enhanced low-energy excitations of electrons on a 2d triangular lattice
Physica B: Condensed Matter, Volumes 378-380, 630-631, (2006)

M. Brühwiler, B. Batlogg, S. M. Kazakov, J. Karpinski
Mass enhancement, correlations, and strong-coupling superconductivity in the beta-pyrochlore KOs_2O_6
Phys. Rev. B 73, 094518 (2006)

G. Caimi, L. Degiorgi, H. Berger, and L. Forro
Optical evidence for a magnetically driven structural transition in the spin web Cu_3TeO_6
Europhys. Lett. 75, 496 (2006)

G. Caimi, L. Degiorgi, H. Berger, and L. Forró
Phonon analysis of the S=1 quantum spin systems $Ni_5Te_4O_{12}X_2$ (X=Cl and Br)
J. Phys.: Condens. Matter 18, 4065 (2006)

G. Caimi, A. Perucchi, L. Degiorgi, H.R. Ott, V.M. Pereira, A.H. Castro Neto, A.D. Bianchi, and Z. Fisk
Magneto-optical evidence of double exchange in a percolating lattice
Phys. Rev. Lett. 96, 016403 (2006)

R. Cubitt, C.D. Dewhurst, M.R. Eskildsen, S.J. Levett, A. Matadeen, J. Jun, S.M. Kazakov, J. Karpinski, S.L. Bud'ko, N.E. Anderson and P.C. Canfield,
Penetration depth anisotropy in MgB_2 single crystals and powders
Journal of Physics and Chemistry of Solids 67, 493-496 (2006)

D. Daghero, R.S. Gonnelli, G.A. Ummarino, A. Calzolari, Valeria Dellarocca, V.A. Stepanov, S.M. Kazakov, J. Jun and J. Karpinski
Effect of the magnetic field on the gaps of MgB2: A directional point-contact study
Journal of Physics and Chemistry of Solids 67, Issues 1-3, 424-427 (2006)

L. Degiorgi
The Drude model in correlated systems
Ann. Phys. 15, 571 (2006)

L. Degiorgi and D. Jerome
Transport and optics in quasi-one-dimensional organic conductors
J. Phys. Soc. Jap. 75, 051004 (2006)

D. DiCastro, M.Ortolani, E.Cappelluti, U.Schade, N.D.Zhigadlo, J.Karpinski
Infrared properties of $Mg_{1-x}Al_x(B_{1-y}C_y)_2$ single crystals in the normal and superconducting state
Phys. Rev. B 73, 174509 (2006)

C. Ellenberger, B. Simovic, R. Leturcq, T. Ihn, S. E. Ulloa, K. Ensslin, D. C. Driscoll, and A. C. Gossard
Two-subband quantum Hall effect in parabolic quantum wells
Phys. Rev. B 74, 195313 (2006)

C. Ellenberger, T. Ihn, C. Yannouleas, U. Landman, K. Ensslin, D. Driscoll, and A.C. Gossard
Excitation spectrum of two correlated electrons in a lateral quantum dot with negligible Zeeman splitting
Phys. Rev. Lett. 96, 126806 (2006)

K. Ensslin
Pinning down the last spin
Nature Physics, News&Views 2, 587 (2006)

M. Erbudak, J.-N. Longchamp, Y. Weisskopf
Self-assembled nano-structures on the icosahedral Al-Pd-Mn quasicrystal
Turkish J. Physics 30 213-219 (2006)

K. Ernits, M. Kaelin, D. Brémaud, T. Meyer, U. Müller, A.N. Tiwari
Ultrasonically sprayed In_2Se_3 films for Cu(In,Ga)Se_2 solar cells
Proceedings 21st European Photovoltaic Solar Energy Conference, Dresden, 1853-1856 (2006)

A. Fuhrer, P. Brusheim, T. Ihn, M. Sigrist, K. Ensslin, W. Wegscheider, and M. Bichler
Fano effect in a ring-dot system with tunable coupling
Phys. Rev. B 73, 205326 (2006)

J. Fujii, F. Borgatti, G. Panaccione, M. Hochstrasser, F. Maccherozzi, G. Rossi and der Laan G. Van
Evidence for in-plane spin-flop orientation at MnPt7Fe(100) interface revealed by x-ray magnetic linear dichroism
Phys. Rev. B 73 , 214444 (2006)

J. Gambetta, A. Blais, D. I. Schuster, A. Wallraff, L. Frunzio, J. Majer, M. H. Devoret, S. M. Girvin, and R. J. Schoelkopf
Qubit-photon interactions in a cavity: Measurement-induced dephasing and number splitting
Phys. Rev. A 74, 042318 (2006)

M. Ganchev,J. Kois, M. Kaelin, S. Bereznev, E. Tzvetkova, O. Volobujeva, N. Stratieva, A. N. Tiwari
Preparation of Cu(In,Ga)Se_2 layers by selenization of electrodeposited Cu-In-Ga precursors
Thin Solid Films 11, 325-327 (2006)

J.L. Gavilano, B. Pedrini, K. Magishi, J. Hinderer, M. Weller, H.R. Ott, S.M. Kazakov, J. Karpinski
Localized versus itinerant magnetic moments in $Na_{0.7}CoO_2$
Phys. Rev. B 74, 064410 (2006)

J.L. Gavilano, E. Felder, D. Rau, H.R. Ott, P. Millet, F. Mila, T. Chicorek, A.C. Mota
$Na_2V_3O_7$: An unusual low-dimensional quantum magnet
Physica B 378-380, 123-124 (2006)

C. Goldmann, C. Krellner, K. P. Pernstich, S. Haas, D. J. Gundlach, and B. Batlogg
Gate Bias Stress in Rubrene ”Flip-Crystal” Field-Effect Transistors
J. Appl. Phys. 99, 034507 (2006)

C. Goldmann, D. J. Gundlach, and B. Batlogg
Evidence of Water-Related Discrete Trap State Formation in Pentacene Single Crystal Field-Effect Transistors,
Appl. Phys. Lett. 88, 063501 (2006). - This paper was also selected for the February 20th, 2006 issue of the Virtual Journal of Nanoscale Science and Technology

R.S. Gonnelli, D. Daghero, A. Calzolari, G.A. Ummarino, M. Tortello, V.A. Stepanov, N.D. Zhigadlo, K. Rogacki, J. Karpinski, C. Portesi, et al.
Recent achievements in MgB_2 physics and applications: A large-area SQUID magnetometer and point-contact spectroscopy measurements
Physica C: Superconductivity, Volume 435, Issues 1-2, 59-65, (2006)

R.S. Gonnelli, D.Daghero, G.A.Ummarino, A.Calzolari, M.Tortello, V.A.Stepanov, N. D. Zhigadlo, K. Rogacki, J.Karpinski
The effect of magnetic impurities in a two-band superconductor: A point-contact study of Mn-substituted MgB_2 single crystals
Phys. Rev. Lett. 97, 037001 (2006)

R.S. Gonnelli, D. Daghero, G.A. Ummarino, A. Calzolari, Valeria Dellarocca, V.A. Stepanov, S.M. Kazakov, J. Jun

and J. Karpinski
A point-contact study of the superconducting gaps in Al-substituted and C-substituted MgB_2 single crystals
Journal of Physics and Chemistry of Solids 67, Issues 1-3, 360-364 (2006)

D. Graf, M. Frommenwiler, P. Studerus, T. Ihn, K. Ensslin, D.C. Driscoll and A.C. Gossard
Local oxidation of Ga[Al]As heterostructures with modulated tip-sample voltages
J. Appl. Phys. 99, 053707 (2006)

V. Guritanu, A.B. Kuzmienko, D. van der Marel, S.M. Kazakov, J. Karpinski
Anisotropic optical conductivity and two colors of MgB_2
Phys. Rev. B 73, 104509 (2006)

S. Gustavsson, R. Leturcq, B. Simovic, R. Schleser, P. Studerus, T. Ihn, K. Ensslin, D. C. Driscoll, and A. C. Gossard
Counting statistics and super-Poissonian noise in a quantum dot
Phys. Rev. B 74, 195305 (2006)

S. Gustavsson, R. Leturcq, B. Simovic, R. Schleser, T. Ihn, P. Studerus, K. Ensslin, D. C. Driscoll, A. C. Gossard
Counting statistics of single-electron transport in a quantum dot
Phys. Rev. Lett. 96, 076605 (2006)

J. Hinderer, S.M. Weyeneth, M. Weller, J.L. Gavilano, E. Felder, F. Hulliger, H.R. Ott
NMR study of CeTe at low temperatures
Physica B 378-380, 765-766 (2006)

A. Kemp, M.V. Fistul, A. Wallraff, Y. Koval, A. Lukashenko, B.A. Malomed, and A.V. Ustinov
Energy Level Spectroscopy of a Bound Vortex-Antivortex Pair
Quantum Computation in Solid State Systems, B. Ruggiero, P. Delsing, C. Granata, Y. Pashkin, P. Silvestrini, (Eds.)
ISBN 0-387-26332-2, Springer, (2006)

R. Khasanov, A.Shengelaya, K.Conder, E.Morenzoni, I.M.Savic, J.Karpinski, H.Keller
Correlation between oxygen isotope effects on transition temperature and magnetic penetration depth in high-temperature superconductors close to optimal doping
Phys. Rev. B 74, 064505, (2006)

G. Khrypunov, A. Romeo, F. Kurdesau, D. L. Bätzner, H. Zogg, A. N. Tiwari
Recent developments in evaporated CdTe solar cells
Solar Energy Materials and Solar Cells 90 (6), 664-677 (2006)

V.G. Kogan, R. Prozorov, S. L. Bud'ko, P. C. Canfield, J. R. Thompson, J. Karpinski, N. D. Zhigadlo, and P. Miranovi
Effect of field-dependent core size on reversible magnetization of high-κ superconductors
Phys. Rev. B 74, 184521 (2006)

A. Kohen, T. Cren, Y. Noat, T. Proslier, F. Giubileo, F. Bobba, A.M. Cucolo, N. Zhigadlo, S.M. Kazakov, J. Karpinski, et al.
Recent progress in vortex studies by tunneling spectroscopy
Physica C: Superconductivity, Volumes 437-438, 145-148, (2006)

A. Kohen, F. Giubileo, F. Bobba, T. Proslier, N. Zhigadlo, S.M. Kazakov, J. Klein, J. Karpinski, A.M. Cucolo and D.

Roditchev
Lazy Fisherman method of vortex analysis: application to MgB_2
Journal of Physics and Chemistry of Solids 67, 442-446 (2006)

C. Krutzler, M. Zehetmayer, M. Eisterer, H.W. Weber, N.D. Zhigadlo, J. Karpinski, and A. Wisniewski,
Anisotropic reversible mixed-state properties of superconducting carbon doped $Mg(B_{1-x}C_x)$ single crystals
Phys. Rev. B 74, 144511 (2006)

F. Kurdesau, G. Khripunov, A. F. da Cunha, M. Kaelin, A. N. Tiwari
Comparative study of ITO layers deposited by DC and RF magnetron sputtering at room temperature
Journal of Non-Crystalline Solids 352 (9-20), 1466-1470 (2006)

G. Lamura, A. Gauzzi, S.M. Kazakov, J. Karpinski and A. Andreone
High-resolution measurements of the magnetic penetrationdepth on $YBa_2Cu_4O_8$ single crystals
Journal of Physics and Chemistry of Solids 67, 447-449 (2006)

R. Leturcq, R. Bianchetti, G. Götz, T. Ihn, K. Ensslin, D. C. Driscoll and A. C. Gossard
Coherent nonlinear transport in quantum rings
Physica E 35, 327 (2006)

R. Leturcq, L. Schmid, K. Ensslin, D. C. Driscoll, and A. C. Gossard
Kondo effect in a three-terminal quantum ring
Phys. Sat. Solidi, 243, 3653 (2006)

R. Leturcq, L. Schmid, K. Ensslin, Y. Meir, D. C. Driscoll and A. C. Gossard
Probing the Kondo density of states in a three-terminal quantum ring
Physica E 34, 441 (2006)

R. Leturcq, L. Schmid, T. Ihn, K. Ensslin, D.C. Driscoll, and A.C. Gossard
Asymmetries of the conductance matrix in a three-terminal quantum ring in the Coulomb blockade regime
Physica E 34, 445 (2006)

R. Leturcq, D. Sanchez, G. Götz, T. Ihn, K. Ensslin, D. C. Driscoll, A. C. Gossard
Magnetic field symmetry and phase rigidity of the nonlinear conductance in a ring
Phys. Rev. Lett. 96, 126801 (2006)

E. Liarokapis, D. Lampakis, D. Palles, J. Karpinski and C. Panagopoulos
A Raman view of local lattice distortions and charge transfer in cuprates
Journal of Physics and Chemistry of Solids, Volume 67, Issues 9-10, 2065-2071, (2006)

P. Liska, K. R. Thampi, M. Grätzel, D. Brémaud, D. Rudmann, H. M. Upadhyaya, A. N. Tiwari
Nanocrystalline dye-sensitized solar cell/copper indium gallium selenide thin-film tandem showing greater than 15% conversion efficiency
Appl. Phys. Lett. 88, 203103 (2006)

J.-N. Longchamp, M. Erbudak, Y. Weisskopf
In situ formation of a new Al-Pd-Mn-Si quasicrystalline phase on the pentagonal surface of the Al-Pd-Mn quasicrystal
Journal de Physique IV France 132 117-120 (2006)

S. Manalo, H. Michor, G. Hilscher, M. Brühwiler, and B. Batlogg
Superconducting properties of $RbOs_2O_6$ analyzed within Eliashberg theory
Phys. Rev. B 73, 224520 (2006)

L. Meier, G. Salis, C. Ellenberger, E. Gini, and K. Ensslin
Gate tunability of stray-field-induced electron spin precession in a GaAs/ InGaAs quantum well below an interdigitated magnetized Fe grating
Phys. Rev. B 74, 245318 (2006)

L. Meier, G. Salis, C. Ellenberger, E. Gini, and K. Ensslin
Stray-field induced modification of coherent spin dynamics
Appl. Phys. Lett. 88, 172501 (2006)

T. Michlmayr, N. Saratz, A. Vaterlaus, D. Pescia and U. Ramsperger
Local magnetic field generation with a scanning tunneling microscope
Virtual J. Nan. Sci. Tech. 17 May 1, 13 (2006)

T. Michlmayr, N. Saratz, A. Vaterlaus, D. Pescia and U. Ramsperger
Local magnetic field generation with a scanning tunneling microscope
J. Appl. Phys. 99, 08N502 (2006)

P. Moras, Y. Weisskopf, J.-N. Longchamp, M. Erbudak, P.H. Zhou, L. Ferrari, C. Carbone
Quantum size effects arising from incompatible point-group symmetries: angle-resolved photoemission study
Phys. Rev. B 74 121405 (2006)

M. Mulazzi, M. Hochstrasser, M. Corso, I. Vobornik, J. Fujii, J. Osterwalder, J. Henk and G. Rossi
Matrix elements effects in angle-resolved valence band photoemission with polarized light from the Ni(111) surface
Phys. Rev. B 74, 035118 (2006)

C.Dubois, N.Jenkins, A.A.Manuel, O.Fischer, N.D.Zhigadli, J.Karpinski
Crystal-edge scanning tunneling spectroscopy on aluminium-doped magnesium diboride
Supercond. Sci. Technol. 19, 695-698, (2006)

H.R. Ott
Heavy electrons and non-Fermi liquids, the early times
Physica B 378-380, 1-6 (2006)

D. Pal, L. DeBeer-Schmitt, T. Bera, R. Cubitt, C.D. Dewhurst, J. Jun, N. D. Zhigadlo, J. Karpinski, V. G. Kogan, M. Eskildsen
Measuring the penetration depth anisotropy in MgB2 using small-angle neutron scattering
Phys. Rev. B 73, 012513 (2006)

G. Panaccione, G. Rossi, M. Hochstrasser, M. Sperl, M. Reinwald, G. Woltersdorf, W. Wegscheider and C.H. Back
Influence of surface treatment on the magnetic properties of $Ga_xMn_1 - xAs$ thin films
Phys. Rev. B 74, 104421 (2006)

M. Papagno, D. Pacile, G. Caimi, H. Berger, L. Degiorgi, and M. Grioni
Electronic structure of one-dimensional copper oxide chains in $LiCu_2O_2$ from angle-resolved photoemission and optical spectroscopy
Phys. Rev. B 73, 115120 (2006)

P. Parisiades, D. Lampakis, D. Palles, E. Liarokapis and J. Karpinski
The relation of the broad band with the E_2g phonon and superconductivity in the $Mg(B_{1-x}C_x)_2$ compound
Journal of Magnetism and Magnetic Materials (2006)

B. Pedrini, S. Weyeneth, J.L. Gavilano, J. Hinderer, M. Weller, H.R. Ott, S.M. Kazakov and J. Karpinski
Magnetic transition in $Na_{0.5}CoO_2$ at 88 K
Physica B: Condensed Matter, Volumes 378-380, 861-862, (2006)

B. Pedrini, S. Weyeneth, J.L. Gavilano, J.Hinderer, M. Weller, H.R. Ott, S.M. Kazakov, J. Karpinski
Magnetic transition in $Na_{0.5}CoO_2$ at 88K
Physica B 378-380, 861-862 (2006)

K.P. Pernstich, D. Oberhoff, C. Goldmann, and B. Batlogg
Modeling the water related trap state created in pentacene transistors
Appl. Phys. Lett. 89, 213509 (2006)

A. Perucchi, L. Degiorgi, Rongwei Hu, C. Petrovic, and V. F. Mitrovic
Optical investigation of the metal-insulator transition in $FeSb_2$
Eur. Phys. J. B54, 175 (2006)

A. Pfund, I. Shorubalko, R. Leturcq, and K. Ensslin
Top-gate defined double quantum dots in InAs nanowires
Appl. Phys. Lett. 89, 252106 (2006)

A. Pfund, I. Shorubalko, R. Leturcq, M. T. Borgström, F. Gramm, E. Müller, and K. Ensslin
Fabrication of semiconductor nanowires for electronic transport measurements
Chimia A726, 729 (2006)

A. Pioda, D. Brunner, S. Kicin, T. Ihn, M. Sigrist, A. Fuhrer, K. Ensslin, M. Reinwald, and W. Wegscheider
Scanning a metallic tip close to a quantum point contact
Physica E 32, 167 (2006)

O. Portmann, A. Vaterlaus and D. Pescia
Observation of stripe mobility in a dipolar frustrated ferromagnet
Phys. Rev. Lett. 96, 047212 (2006)

O. Portmann, M. Buess, A. Vindigni, A. Vaterlaus, D. Pescia and C.H. Back
Micromagnetism in the ultrathin limit
Thin Solid Films 502, 2 (2006)

O. Portmann
Micromagnetism in the ultrathin limit
Logos Verlag berlin, 2006, ISBN 3-8325-1232-2

K. Rogacki, B. Batlogg, J. Karpinski, N.D. Zhigadlo, G. Schuck, S.M. Kazakov, P. Wägli, R. Puzniak, A. Wisniewski, F. Carbone, A. Brinkman, D. van der Marel
Strong magnetic pair breaking in Mn substituted MgB_2
Phys. Rev. B 73, 174520 (2006)

A. Romeo, G. Khrypunov, F. Kurdesau, M. Arnold, D.L. Batzner, H. Zogg, A.N. Tiwari
High efficiency flexible CdTe solar cells on polymer substrates
Solar Energy Materials and Solar Cells 90 (18-19), 3407-3415 (2006)

B. Rössner, B. Batlogg, H. von Känel, D. Chrastina, and G. Isella
Hole band nonparabolicity and effective mass measurement in p-SiGe/Ge hetero-structures
Mat. Sci. in Semicond. Processing 9, 777-780 (2006)

B. Rössner, H. von Känel, D. Chrastina, G. Isella, and B, Batlogg
2-D hole gas with two-subband occupation in a strained-Ge channel: Scattering mechanisms
Thin Solid Films 508, 351-354 (2006)

G.Schuck, S.M.Kazakov, K.Rogacki, N.D.Zhigadlo, J.Karpinski
Crystal growth, structure, and superconducting properties of beta-pyrochlores KOs_2O_6
Phys. Rev. B 73, 144506 (2006)

A. Sacchetti, L. Degiorgi, T. Giamarchi. N. Ru, and I.R. Fisher
Chemical pressure and hidden one-dimensional behavior in rare-earth tri-telluride charge-density wave compounds
Phys. Rev. B 74, 125115 (2006)

I. Shorubalko, A Pfund, R Leturcq, M T Borgström, F Gramm, E Müller, E Gini and K Ensslin
Tunable few electron quantum dots in InAs nanowires
Nanotechnology 18, 044014 (2006)

M. Sigrist, T. Ihn, K. Ensslin, M. Reinwald, and W. Wegscheider
Phase coherence in the cotunneling regime of a coupled double quantum dot
Physica E 34, 497 (2006)

M. Sigrist, S. Gustavsson, T. Ihn, K. Ensslin, D. Driscoll, A. Gossard, M. Reinwald, and W. Wegscheider
Few-electron quantum dot fabricated with layered scanning force microscope lithography
Physica E 32, 5 (2006)

M. Sigrist, T. Ihn, K. Ensslin, D. Loss, M. Reinwald, W. Wegscheider
Phase coherence in the inelastic cotunneling regime
Phys. Rev. Lett. 96, 036804 (2006)

B. Simovic, S. Gustavsson, R. Leturcq, P. Studerus, K. Ensslin, J. Forrer, A. Schweiger, and R. Schuhmann
Study of the microwave-induced transport through a quantum dot inserted in a 35-GHz loop-gap resonator
Physica E 34, 480 (2006)

B. Simovic, C. Ellenberger, K. Ensslin, H.-P. Tranitz, W. Wegscheider
Oscillations of the magnetoresistance of a two-dimensional electron gas under microwave irradiation: Influence of the irradiation frequency
Physica E 34, 93 (2006)

B. Simovic, R. Schuhmann, J. Forrer, P. Studerus, S. Gustavsson, R. Leturcq, K. Ensslin, and A. Schweiger
Design of Q-Band loop-gap resonators at frequencies (34-36 GHz) for single electron spin spectroscopy in semiconductor nanostructures
Rev. Sc. Instr. 77, 064702 (2006)

H.M. Singer, I. Singer-Liginova, J.H. Bilgram, and G. Amberg
Morphology diagram of thermal dendritic solidification by means of phase-field models in two and three dimensions
J. Crystal Growth 296, 58-68 (2006)

H.M. Singer and J.H. Bilgram
Integral scaling behavior of different morphologies of 3D xenon crystals
Physica D 219, 101-110 (2006)

A.V. Sologubenko, N.D.Zhigadlo, J.Karpinski, H.R.Ott
Thermal conductivity of Al-doped MgB_2: Impurity scattering and the validity of the Wiedemann-Franz law
Phys. Rev. B 74, 184523 (2006)

A.V. Sologubenko, N.D. Zhigadlo, J. Karpinski, H.R. Ott
Thermal conductivity of Al-doped MgB_2: Impurity scattering and the validity of the Wiedemann-Franz law
Phys. Rev. B 74, 184523 (2006)

S. Streule, M. Medarde, A. Podlesnyak, E. Pomjakushina, K. Conder, S. Kazakov, J. Karpinski, J. Mesot
Short range charge ordering in $Ho_{0.1}Sr_{0.9}CoO_{3-x}$ (0.15¡x¡0.49)
Phys. Rev. B 73, 024423 (2006)

A. Vindigni, A. Rettori, M.G. Pini, C. Carbone and P. Gambardella
Finite-sized Heisenberg chains and magnetism of the one-dimensional metal systems
Appl. Phys. A 82, 385 (2006)

P. Wachter
Localized versus itinerant: Towards the limits
Proceedings 36iémes Journées des Actinides, K41, Oxford, (2006)

P. Wachter, A. Jung and F. Pfuner
Exciton condensation in intermediate valent $Sm_{0.90}La_{0.10}S$
Phys. Letters A 359, 528 (2006)

Y. Weisskopf, M. Erbudak, J.-N. Longchamp, T. Michlmayr
Ni deposition on the pentagonal surface of an icosahedral Al-Pd-Mn quasicrystal
Surface Science 600 2594-2599 (2006)

Y. Weisskopf
Growth of CsCl-type domains on icosahedral quasicrystal Al-Pd-Mn
Logos Verlag, Berlin, 2006, ISBN 3-8325-1420-1

M. Weller, J. Hinderer, J.L. Gavilano, B. Pedrini, D. Rau, I. Sheikin, M. Chiao, H.R. Ott
NQR studies of $CePd_2In$ under hydrostatic pressure
Physica B 378-380, 829-830 (2006)

O. Wittwer and J. H. Bilgram
Three-dimensional xenon dendrites: Characterization of sidebranch growth
Phys. Rev. E 74, 041604 (2006)

O. Wittwer and J.H. Bilgram
Onset and amplitude of sidebranches in three dimensional growth of xenon dendrites
Mat. Sci. and Eng. A 413-414, 447 (2005)

S. Wu, P.Geiser, J.Jun, J.Karpinski, J.-R.Park, R.Sobolewski
Long-lived, coherent Acoustic phonon oscillations in GaN single crystals
Appl. Phys. Lett. 88, 041917 (2006)

M. Zehetmayer, C. Krutzler, M. Eisterer, J. Jun, S.M. Kazakov, J. Karpinski and H.W. Weber
Effect of disorder on the irreversible magnetic properties of single crystalline MgB2: comparison of carbon doping and neutron irradiation
Physica C: Superconductivity, Volumes 445-448, 65-68 (2006)

M. Zehetmayer, M. Eisterer, R.Müller, M.Weigand, J.Jun, S. M. Kazakov, J. Karpinski, H. W. Weber
Flux pinning in neutron irradiated MgB_2 single crystals
Journal of Physics: Conference Series 43 651-654, (2006)

H. Zogg, M. Arnold
Narrow spectral band monolithic lead-chalcogenide-on-Si mid-IR photodetectors
Opto-Electronics review 14, 1, 33-36 (2006) (invited)

Chapter 7

Talks

(⋆ = invited)

Arnold, F. Felder, M. Rahim, N. Quack, S. Blunier, H. Zogg M.
Resonant Cavity Photodetektoren für Infrarotsensoren mit durchstimmbarer Wellenlänge
DMBE WS06, Deutscher MBE-Workshop, Hamburg, Germany, 26-27.9.2006

⋆ Batlogg B.
Pyrochlore-structured superconductors AOs2O6: mass enhancement and low frequency phonons
Novel Materials and Superconductivity, Planneralm, Austria, 14.02.2006

Batlogg B.
Negative thermal expansion in van der Waals bonded crystals
APS March Meeting, Baltimore, USA, 14.03.2006

Batlogg B.
Narrow band tails in organic semiconductor crystals
APS March Meeting, Baltimore, USA, 15.03.2006

⋆ Batlogg B.
Bulk and interface electronic density of states :a systematic and quantitative study
ICAM Conference on Organic Crystalline Electronics, Baltimore, USA, 18.03.2006

⋆ Batlogg B.
Organic Semiconductors : basic questions and practical issues
EUROFET Conference, Berlin, Wildau, Germany, 27.06.2006

Belousov A.
III-Nitride bulk crystals growth under high pressure
1st MRC Graduate Symposium, Zurich, Switzerland, 29.06.2006

Belousov A.
III-Nitride bulk crystals growth under high pressure
Summerschool on Wide-bandgap Semiconductor Quantum Structures, Monte Verita, Switzerland, 27.08.2006

⋆ Bilgram J.
Controlling of Complex Structures
7th Warren Symposium, Schloss Ringberg, Germany, 22.01.2006

* Bilgram J.
Controlling of Complex Structures
14. Jahrestagung, Deutsche Gesellschaft für Kristallographie, Freiburg im Breisgau, Germany, 04.04.2006

* Bilgram J.
Erstarren von Xenon: Modellexperimente für das Erstarren von Metallen
Physikalisches Kolloquium, TU Braunschweig, Germany, 02.05.2006

Brémaud D.
Flexible and Lightweight Cu(In,Ga)Se_2 Solar Cells
Nonmetallic Inorganic Materials Seminar, Zurich, Switzerland, 13.6.2006

Brühwiler M.
Itinerant Correlated Electrons on the Pyrochlore Lattice;
American Physical Society March Meeting, Baltimore, USA, 16.03.2006

* Brühwiler M.
Superconductivity in the beta-pyrochlore Osmates;
8th International Conference on Materials and Mechanisms of Superconductivity and High Temperature Superconductors, Dresden, Deutschland, 11.07.2006

Bukowski Z.
High-pressure growth of Rb, K and Na osmate single crystals with the pyrochlore structure
Swiss Physical Society-MaNEP Meeting, Lausanne, Switzerland, 13.02.2006

Bukowski Z.
$Na_2Os_2O_{6.5}$-new metallic pyrochlore synthesized under high pressure
8th International Conference on Materials and Mechanism of Superconductivity and High Temperature Superconductors, M2S-HTSC VIII, Dresden, Germany, 13.07.2006

Can P.
A critical test for a quasicrystalline icosahedral model
13th Conference on Statistical Physics, Istanbul, Türkei, 6.7.2006

* Degiorgi L.
Magneto-optical evidence of double exchange in a percolating lattice
Internal MaNEP Workshop 2006, Neuchatel, Switzerland, 6.2.2006

Degiorgi L.
Optical evidence for a magnetically driven structural transition inthe spin web Cu_3TeO_6
March Meeting of the American Physical Society, Baltimore, U.S.A., 13.3.2006

Degiorgi L.
Magneto-optical evidence of double exchange in a percolating lattice
March Meeting of the American Physical Society, Baltimore, U.S.A., 14.3.2006

* Degiorgi L.
Magneto-optical investigation of Ca-doped Europium Hexaborides
Colloquium at the Physics Department of the Temple University, Philadelphia, U.S.A., 20.3.2006

* Degiorgi L.
Magneto-optical investigation of Ca-doped Europium Hexaborides
Seminar at the Physics Department of the Boston University, Boston, U.S.A., 22.3.2006

* Degiorgi L.
Faszination der Physik
Kinder-Vorlesung, ETH Zürich, Zürich, Switzerland, 8.6.2006

* Degiorgi L.
Magneto-optical evidence of double exchange in a percolating lattice
International Conference on Low Energy Electrodynamics in Solids 2006, Tallinn, Estonia, 1.7.2006

* Ensslin K.
Electrons in quantum dots - one by one
Edgar Lüscher Seminar, Klosters, Switzerland, 04.02.2006

* Ensslin K.
Time-resolved single electron transport through quantum dots
Meeting of the Swiss Physical Society, Lausanne, Switzerland, 13.02.2006

* Ensslin K.
Noise in quantum dots
DARPA Spin Qubit meeting, Lenzerheide, Switzerland, 16.2.2006

* Ensslin K.
Klassische Computer und Quanten-Computer
Erwachsenenbildung Erzingen, Germany, 30.03.2006

* Ensslin K.
Shot noise in quantum dots
Seminar, University of Marseille Marseille, France, 24.04.2006

* Ensslin K.
Shot noise in quantum dots
Workshop on ”Quantum Coherence, Noise and Decoherence in Nanostructures”, Dresden, Germany, 15.05.2006

* Ensslin K.
Electrons in quantum dots - one by one
Physics colloquium, University of Düsseldorf, Germany, 01.06.2006

* Ensslin K.
Two subband quantum Hall effect
Workshop on ”Strongly correlated low-dimensional systems”, Ascona, Switzerland, 02.07.2006

* Ensslin K.
Is inelastic cotunneling phase coherent?
28th International conference on the physics of semiconductors Vienna, Austria, 28.07.2006

* Ensslin K.
Shot Noise in Quantum Dots
International Conference on nanoscience and Technology Basel, Switzerland, 30.07.2006

* Ensslin K.
Shot Noise in Quantum Dots
6th Rencontres du Vietnam, ”Nanophysics: from fundamentals to applications” Hanoi, Vietnam, 06.08.2006

* Ensslin K.
Spatially resolved Raman spectroscopy of single- and few-layer graphene
International seminar and workshop, graphene week Dresden, Germany, 25.09.2006

* Erbudak M.
Nanotechnology - A physicist view
Colloquium at the Turkish Academy of Sciences, Istanbul, Türkei, 1.5.2006

Erbudak M.
A critical test for a quasicrystalline icosahedral model
13th Conference on Statistical Physics, TR-Istanbul, 6-8.7.2006

* Erbudak M.
Stacking of objects in nature and quasicrystallography
Physics Seminar, Akdeniz University, Antalya, Türkei, 20.9.2006

* Erbudak M.
Electronic structure of quasicrystals
Physics Seminar, Samsun University, Samsun, Türkei, 3.10.2006

Ernits, D. Brémaud, M. Kaelin, T. Meyer, U. Müller, A.N. Tiwari K.
Ultrasonically Sprayed InxSy Films for Cu(In,Ga)Se_2 Solar Cells
21st European Photovoltaic Solar Energy Conference, Dresden, Germany, 4-8.9.2006

Felder, M. Rahim, M. Arnold, H. Zogg F.
Komponenten für VECSEL im mittleren Infrarot
36. IR Kolloquium, Freiburg i.Brs., Deutschland, 4-5.4.2006

Fell M.
Transiente dendritische Wachstumsformen bei Temperaturänderungen
DGKK Kinetikseminar, Halle, Germany, 15.02.2006

Fell M.
Transient Growth and Controlled Side Branching of Xenon Dendrites
APS, Baltimore, USA, 13.03.2006

Fell M.
Controlling of Structure Formation in Crystal Growth
DPG, MM, Dresden, Germany, 29.03.2006

Fell M.
Controlling of Structure Formation in Crystal Growth
Symposium on Structure Formation and Self-Organization, Dresden, Germany, 30.03.2006

* Gildemeister A.
A Scanning Gate Microscope for Dilution Refrigerator Temperatures
Visit of the Goldhaber-Gordon group, Stanford University, USA, 16.01.2006

Gildemeister A.
Scanning Gate Microscopy on Semiconductor Quantum Dots
14th International Winterschool on New Developments in Solid State Physics Mauterndorf, Austria 13.02.2006

Gildemeister A.
Scanning Gate Microscopy
QSIT Conference, Engelberg, Switzerland, 21.03.2006

Gildemeister A.
Scanning Gate Microscopy of a Quantum Dot with Charge Read-Out
Nanospectra Meeting Zurich, Switzerland, 4.05.2006

Gildemeister A.
Scanning Gate Microscopy of a Coupled Quantum Dot - Quantum Point Contact System
28th International conference on the physics of semiconductors, Vienna, Austria, 24.07.2006

Gildemeister A.
Ultra Low Temperature Scanning Gate Microscopy of Semiconductor Nanostructures
Industry Day, Zurich, Switzerland, 4.09.2006

Goldmann C.,
Charge Transport in Organic Single-Crystal Field-Effect Transistors,
Solid state Seminar ETH Zurich, Switzerland, 27.04. 2006

Graf D.
Electrical transport and raman spectroscopy on individual few-layer graphene
MRC Graduate Symposium Zurich, Switzerland, 29.06.2006

Graf D.
Raman spectroscopy on individual few-layer graphene islands
28th International conference on the physics of semiconductors, Vienna, Austria, 25.07.2006

Graf D.
Quantum dots with internal substructure
28th International conference on the physics of semiconductors, Vienna, Austria, 26.07.2006

* Grbic B.
Hole transport in nanostructures defined on ptype C-doped GaAs heterostructures
SFB Seminar, Institute for Applied and Experimental Physics Regensburg, Germany, 06.02.2006

Grbic B.
Single-hole transistor in p-type GaAs/AlGaAs heterostructures
14th International Winterschool on New Developments in Solid State Physics Mauterndorf, Austria 15.02.2006

Grbic B.
Hole transport in p-type GaAs quantum dots and point contacts
28th International conference on the physics of semiconductors,Vienna, Austria, 26.07.2006

Gustavsson S.
Design of loop-gap resonators at Q band frequencies (34-36 GHz) for single electron spin spectroscopy in semiconductor nanostructures
14th International Winterschool on New Developments in Solid State Physics Mauterndorf, Austria 15.02.2006

Gustavsson S.
Counting statistics of single electron transport in a quantum dot
14th International Winterschool on New Developments in Solid State Physics Mauterndorf, Austria 15.02.2006

Gustavsson S.
Design of loop-gap resonators at Q band frequencies (34-36 GHz) for single electron spin spectroscopy in semiconductor nanostructures
4th International Conference on Quantum Dots, Chamonix, France, 02.05.2006

Gustavsson S.
Counting statistics of single electron transport in a quantum dot
4th International Conference on Quantum Dots, Chamonix, France, 02.05.2006

Gustavsson S.
Counting statistics of single electron transport in a quantum dot
28th International conference on the physics of semiconductors, Vienna, Austria, 24.07.2006

Hergert, R. Hock (University of Erlangen-Nurnberg), D. Rudmann, A.N. Tiwari F.
Crystal growth mechanisms of chalcopyrite compounds and the role of sodium doping
E-MRS 2006 Spring Meeting, Nice, France, 29.5-2.6.2006

Hochstrasser M.
Epitaxial Ferromagnet on Ge(111): Mn_5Ge_3
2006 APS March Meeting, Baltimore, USA, 17.3.2006

* Hochstrasser M.
The Advanced Photoelectric-effect Experiments (APE) Beamline at the ELETTRA Synchrotron: A multipurpose facility to study electronic and magnetic properties
Rutgers University, Piscataway, USA, 20.3.2006

* Hochstrasser M.
The Advanced Photoelectric-effect Experiments (APE) Beamline at the ELETTRA Synchrotron: A multipurpose facility to study electronic and magnetic properties
Laboratorium für Festkörperphysik, ETH Zurich, Switzerland, 11.05.2006

* Ihn T.
Phase-coherence in the inelastic cotunneling regime
QSIT workshop, Arosa, Switzerland, 20.01.2006

* Ihn T.
Scanning Force Microscope Investigations on Low-Dimensional Electron Systems
Seminar der Gruppe von Klaus von Klitzing, Max Planck Institut für Festkörperforschung Stuttgart, Germany, 13.03.2006

* Ihn T.
Quantum dots on parabolic quantum wells: g-factor tuning and electronic correlations
Int. Conf. on High Magnetic Fields in Semiconductor Physics Würzburg, Germany, 03.08.2006

* Ihn T.
Real-time single-electron detection. What next?
Workshop on quantum information processing Castasegna, Switzerland, 25.09.2006

* Ihn T.
Phase-coherent currents through quantum dots in the inelastic cotunneling regime
Seminar in der Gruppe von Elisa Molinari, Modena, Italien, 09.10.2006

* Ihn T.
Measuring current and noise by counting single electrons
Int. Workshop on Spectroscopy of Semiconducting Nanoparticles Duisburg, Germany, 08.12.2006

Kalb W.
New organic semiconductors for flexible electronics
Eurofet Meeting, Berlin, Germany, 25.06.2006

Kalb W.
New organic semiconductors for flexible electronics
MRC Graduate Symposium, Zürich, Switzerland, 29.06.2006

Kalb W.
Field-effect in new small molecule organic semiconductors
ECOF 10, Riga, 21.08.2006

Karpinski J.
Magnetic and non-magnetic substitutions in MgB_2 single crystals: influence on superconducting properties and structure
Swiss Physical Society-MaNEP Meeting, Lausanne, Switzerland, 13.02.2006

Karpinski J.
Magnetic and non-magnetic substitutions in MgB_2 single crystals influence on superconducting properties and structure
American Physical Society March Meeting, Baltimore, USA, 11.03.2006

* Karpinski J.
Influence of magnetic and non-magnetic substitutions in MgB_2 single crystals, on superconducting properties and structure
Ceramic Congress CIMTEC, Acireale, Sicily, Italy, 04.06.2006

⋆ Karpinski J.
Influence of substitutions, defects and inhomogeneities on superconducting properties and structure of boride and oxide superconductors
From Solid State Physics to Biophysics, Cavtat, Kroatia, 24.06.2006

Karpinski J.
Magnetic and non-magnetic substitutions in MgB_2 single crystals: influence on superconducting properties and structure
8th International Conference on Materials and Mechanism of Superconductivity and High Temperature Superconductors, M2S-HTSC VIII, Dresden, Germany, 09.07.2006

⋆ Karpinski J.
MgB_2 single crystals, Influence of magnetic and non-magnetic substitutions on superconducting properties and structure
MRS Warsaw, Poland, 04.09.2006

Karpinski J.
Influence of magnetic and non-magnetic substitutions in MgB_2 single crystals, on superconducting properties and structure
Controlled Mesoscopic Phase Separation, Heraklion, Greece, 24.10.2006

Karpinski J.
Crystal growth, structural studies, and superconducting properties of beta-pyrochlore KOs_2O_6
8th International Conference on Materials and Mechanism of Superconductivity and High Temperature Superconductors, M2S-HTSC VIII, Dresden, Germany, 10.07. 2006

⋆ Kicin S.
Local spectroscopy of quantum dots
Institute of Electrical Engineering-seminar Bratislava, Slovakia, 12.01.2006

⋆ Leturcq R.
Counting statistics of single electron transport in a quantum dot
International Conference Nanoelectronics 2006, Lancaster University, UK, 09.01.2006

⋆ Leturcq R.
Coherent nonlinear transport in quantum rings
14th International Winterschool on New Developments in Solid State Physics, Mauterndorf, Austria, 16.02.2006

⋆ Leturcq R.
New materials for transport experiments in semiconductor quantum dots
International Workshop on Multifunctional Materials III Bariloche, Argentina, 07.03.2006

⋆ Leturcq R.
Counting statistics of single electron transport in a quantum dot
21st Conference of the European Physical Society, Condensed Matter Division Dresden, Germany, 27.03.2006

⋆ Leturcq R.
New materials for transport experiments in semiconductor quantum dots
2nd International Workshop of NANO Systems Institute Seoul, Corea, 08.05.2006

Leturcq R.
Magnetic field symmetry and phase rigidity of the nonlinear conductance of a ring
28th International Conference on the Physics of Semiconductors Vienna, Austria, 28.07.2006

* Leturcq R.
Magnetic field asymmetry of the nonlinear transport in quantum rings
6emes Rencontres du Vietnam, Hanoi, Vietnam, 09.08.2006

Longchamp J.-N.
Quasicrystals as template for the growth of self-assembled and oriented nanocrystals
International Workshop on Nanostructured Materials, Antalya, Turkey, 21.6.2006

Longchamp J.-N.
Self-Assembled and Oriented Nanocrystals on Quasicrystal Surfaces
International Conference on NANO-Structures Self Assembling, Aix-en-Provence, France. 2.7.2006

Meier L.
Stray-field-induced modification of coherent spin dynamics
QSIT-Meeting, Arosa, Switzerland, 21.01.2006,

Meier L.
Stray-field-induced modification of coherent spin dynamics
Annual Meeting of the Swiss Physical Society Lausanne, Switzerland, 13.02.2006

Meier L.
Stray-field-induced modification of coherent spin dynamics
QSIT-Meeting, Engelberg, Switzerland, 23.03.2006

Meier L.
Stray-field-induced modification of coherent spin dynamics
Department Meeting IBM Rüschlikon, Rüschlikon, Switzerland, 29.09.2006

Michlmayr T.
Local Magnetic fields
ICMFS, Sendai, 17.8.2006

Michlmayr T.
Local Magnetic Fields
Nanoscience Platform - Industry day, ETH Zürich, 4.9.2006

* Monnier R.
Physikunterricht gestern und heute
Alumni-Treffen: 50 Jahre Bauingenieur Diplom ETH Zürich, Switzerland, 14.09.2006

* Monnier R.
Quelques scénarios de catastrophes naturelles
ETH unterwegs, Bulle, Switzerland, 21.11.2006

Müller T.
A Radio Frequency Quantum Point Contact Charge Read-Out
28th International Conference on the Physics of Semiconductors Vienna, Austria, 28.07.2006

* Ott H.R.
Open questions in relation to designing emergent matter
ICAM meeting: Designing Emergent Matter, Denver, USA, 21-26.6.2006

* Ott H.R.
Electronic and magnetic properties of low dimensional spin systems
Miniworkshop on New States of stable and unstable Quantum Matters, Trieste, Italy, 13-19.8.2006

* Ott H.R.
Research funding by SNF
Conference on research funding strategies, Taipei, Taiwan, 26-31.8.2006

* Ott H.R.
Introduction to the physics of low-D systems
MaNEP Summer School on low-D systems, Saas Fee, Switzerland, 11.9.2006

* Ott H.R.
Thermal properties of low-D systems
MaNEP Summer School on low-D systems, Saas Fee, Switzerland, 12.9.2006

Pernstich K.
Contact properties and bias stress effects in PTCDI transistors
Eurofet Meeting, Eindhoven, Netherlands, 19.01.2006

Pernstich K.
Modeling water - related traps states created in Pentacene single crystal FETs
Eurofet Meeting, Wildau, Germany, 26.06.2006

* Pescia D.
Correlations in modulated structures
Texas AM University, College Station USA, 29.01.2006

* Pescia D.
Was müssen die Gymnasialschüler wissen, um an der ETH erfogreich zu sein
Kolloqium für Lehrpersonen, ETH Zurich, 11.11.2006

Pfund A.
Transport in semiconductor nanowires
MRC Graduate Symposium, Zurich, Switzerland, 29.06.2006

Pfund A.
Transport in Semiconductor Nanowire Devices
International Conference on Nanoscience and Technology Basel, Switzerland, 02.08.2006

Portmann O.
Micromagnetism in the ultrathin limit
APS March Meeting, Baltimore, 15.3.2006

Portmann O.
Vectorial spin structure of walls between head-to-head domains
IWST 2006, Nancy, 2-4.10.2006,

Rahim, M. Arnold, F. Felder, H. Zogg, I. Zasavitskiy M.
Vertical External Cavity Surface Emitting Laser (VECSEL) for the Mid-Infrared with IV-VI Compounds
DMBE WS06, Deutscher MBE-Workshop, Hamburg, Germany, 26-27.9.2006

Ramsperger U., Saratz N., Michmlayr T., Pescia D.
Spintronic Devices
Micro and nano Science Platform - Industry Day, ETH Zürich, 4.9.2006

Rudmann, D. Brémaud, A.N. Tiwari D.
A mechanism for Na effects based on the presence of Na at CIGS grain boundaries
E-MRS 2006 Spring Meeting, Nice, France, 29.5-2.6.2006

Rössner B.
Low-temperature transport in high quality strained Ge channels in SiGe
Annual APS March Meeting 2006, Baltimore, USA, 16.03.2006

Rössner B.
Hole band nonparabolicity and effective mass measurement in p-SiGe/Ge hetero-structures
EMRS Spring Meeting, Nice, France, 29.05.2006

Sacchetti A.
Pressure-driven orbital reorientation and change in Mott Hubbard gap in $YTiO_3$
Journal Club LFKP ETHZ, Zürich, Schweiz, 8.12.2006

Saratz N.
Domain Nucleation in ultrathin Fe films on Cu(100)
ICMFS (Intl. Colloqium on magnetic films and surfaces), Sendai, 17.8.2006

Saratz N.
Magnetism at Low temperatures
Nanoscience Platform - Industry day, ETH Zürich, 4.9.2006

Stassen A.
Charge transport in rubrene and its derivatives
Eurofet Meeting, Eindhoven, Netherlands, 19.01.2006

Stassen A.
High mobility in rubrene SC-FETs: The influence of pi-stacking
MRS springmeeting San Francisco, USA, 16.04.2006

Stassen A.
Bulk and interface trap states in organic single crystals for field-effect devices
SPIE Optronics Meeting San Diego, USA, 11.09.2006

* Tiwari A.
Flexible solar cells based on compound semiconductors
21st European Photovoltaic Solar Energy Conference, Dresden, Germany, 4-8.9.2006

* Tiwari A.N.
Prospects of low cost (non-vacuum) processes for thin film CIGS solar cells,
Summer School on Photovoltaics, Talinn, Estonia, 21-25.8.2006

* Tiwari A.N.
CdTe thin film solar cells
Summer School on Photovoltaics, Talinn, Estonia, 21-25.8.2006

* Tiwari A.N.
Prospects of flexible solar cells for cost effective and sustainable energy production
3rd Bi-Annual Nanotech for Investors Summit: Global Investment Opportunities & Market Impact, Zurich, Switzerland, 11.9.2006

Vindigni A.
Inverse transition of magnetic domain patterns in ultrathin Fe films on Cu(100): a quantitative analysis
APS March Meeting, Baltimore, 13-17.3.2006

* Vindigni A.
Open questions in modulated 2D magnetic patterns
SISSA,Trieste, 05.06.2006

* Vindigni A.
Glauber Model and Single-Chain Magnets
Laboratoire de Chimie Inorganique et Materiaux Moleculaires, CNRS, Universite Pierre et Marie Curie, 27.06.2006

Von Känel H.
Effective mass measurement: Influence of hole band nonparabolicity in SiGe/Ge quantum wells
Third Int. SiGe Technology and Device Meeting (ISTDM), Princeton, New Jersey, USA, 15.05.2006

* Wachter P.
Localized versus itinerant: Towards the limits
36iémes Journées des Actinides, St. Catherine's College, Oxford, UK, 04.04.2006

* Wachter P.
Similarities between Cu and Pu containing "high Tc" superconductors
IWOSMA-3, CECAM Lyon, France, 02.06.2006

* Wachter P.
Similarities between Cu and Pu containing "high Tc" superconductors
15th Int. Conf. on Solid Compounds of Transition Elements, Krakow, Poland, 15.07.2006

* Wallraff A.
Quantum Optics and Quantum Computing with Superconducting Circuits Interactions and Dynamics in Low Dimen-

sional Quantum Systems
Weizmann Institute of Science, Israel, 04.01.2006

* Wallraff A.
A Dispersive Qubit Readout
Gordon Research Conference on Superconductivity, Santa Ynez Valley Marriott, Buellton, USA, 22.01.2006

* Wallraff A.
Superconducting Qubits and Cavities
International Symposium on Mesoscopic Superconductivity and Spintronics 2006 (MS + S2006), NTT R&D Center, Atsugi, Kanagawa, Japan, 27.02.2006

Wallraff A.
Coherent control in circuit QED
APS March Meeting 2006, Baltimore, USA, 13.03.2006

Wallraff A.
Towards single shot read-out in circuit quantum electrodynamics (QED)
APS March Meeting 2006, Baltimore, USA, 14.03.2006

Wallraff A.
RF critical current of Josephson junction
APS March Meeting 2006, Baltimore, USA, 15.03.2006

Wallraff A.
Cavity Josephson Bifurcation Amplifier: a microwave readout for a superconducting qubit
APS March Meeting 2006, Baltimore, USA, 16.03.2006

* Wallraff A.
Superconducting qubits
Condensed Matter and Materials Physics (CMMP06), University of Exeter, UK, 19.04.2006

* Wallraff A.
Circuit QED: Superconducting Qubits and Cavities
366. WE-Heraeus-Seminar: Qubits and Macroscopic Quantum Coherence: From Superconducting Devices to Ultracold Gases, Bad Honnef, Germany, 07.05.2006

* Wallraff A.
Circuit QED: Superconducting Qubits and Cavities
International Workshop on Solid State Based Quantum Information Processing, Herrsching, Bavaria, 24.05.2006

* Wallraff A.
Quantum Optics and Quantum Information Processing with Superconducting Circuits
Colloquium, Section de Physique, Universite de Geneve, Geneva, Switzerland, 19.06.2006

* Wallraff A.
Circuit Quantum Electrodynamics: Superconducting Qubits and Cavities
Seminar Atelier de Physique Theorique, Département de Physique Théorique, Universite de Geneve, Geneva, Switzerland, 20.06.2006

* Wallraff A.
Quantum Optics and Quantum Information Processing with Superconducting Circuits
8th International Conference on Materials and Mechanisms of Superconductivity and High Temperature Superconductors, Dresden, Germany, 09.07.2006

* Wallraff A.
Quantum Optics and Quantum Information Processing with Superconducting Circuits
SFB/TR21 Control of quantum correlations in tailored matter (COCOMAT) Workshop, Freudenstadt-Lauterbad, Germany, 13.10.2006

* Wallraff A.
Was ist Licht?
An den Grenzen des Wissens, Interdisziplinäre Veranstaltungsreihe UZH und ETHZ, ETH Zürich, Switzerland, 16.11.2006

Weisskopf Y.
Quasicrystal-crystal interfaces: Fe and Ni nanostructures on the pentagonal surface of icosahedral Al-Pd-Mn quasicrystal
Symposium on Surface Science 2006, St. Christoph am Arlberg, Österreich, 9.3.2006

Weisskopf Y.
Self-assembled nanostructures on quasicrystal surfaces
1st MRC Graduate Symposium, Zürich, Schweiz, 29.6.2006

Weisskopf Y.
Quasicrystal-crystal interfaces
Aperiodic 2006, Zao, Miyagi, Japan, 21.9.2006

Weller M.
"Magnetic Field-Induces Superconductivity in the Ferromagnet URhGe", F. Lévy, I. Sheikin, B. Grenier, et al. Science 309, 1343 (2005)
Journal Club LFKP ETHZ, Zürich, Schweiz, 27.1.2006

Weller M.
NMR study of CeTe at low temperatures
SPS/MaNEP meeting, Lausanne, Schweiz, 14.2.2006

Weller M.
NMR studies of $BaVS_3$
SPS/MaNEP meeting, Lausanne, Schweiz, 14.2.2006

* Weller M.
NMR/NQR studies of two unusual magnetic systems: $BaVS_3$ and $CePd_2In$
Institutsseminar Hochfeldlabor Rossendorf, Rossendorf (Dresden), Deutschland, 7.4.2006

Weller M.
"Switching the electrical resistance of individual dislocations in singel-crystalline $SrTiO_3$", S. Krzysztof et al. Nature Materials 5, 312 (2006)
Journal Club LFKP ETHZ, Zürich, Schweiz, 7.7.2006

Wittwer O.
Characterization of Instabilities of 3D Xenon Crystals
DPG, MM, Dresden, Germany, 29.03.2006

Wittwer O.
Xenon Dendrites: Onset and Amplitude of Sidebranches
Symposium on Structure Formation and Self-Organization, Dresden, Germany, 30.03.2006

Zhigadlo N.D.
Synthesis of $Ca_{2-x}Na_xCuO_2C_{l2}$ single crystals under high pressure
Swiss Physical Society-MaNEP Meeting, Lausanne, Switzerland, 14.02.2006

Zhigadlo N.D.
High-pressure synthesis and superconductivity of $Ca_{2-x}Na_xCuO_2C_{l2}$
8th International Conference on Materials and Mechanism of Superconductivity and High Temperature Superconductors, M2S-HTSC VIII, Dresden, Germany, 10.07.2006

Zhigadlo N.D.
MgB_2 single crystals substituted with magnetic ions: Strong suppression of superconductivity
8th International Conference on Materials and Mechanism of Superconductivity and High Temperature Superconductors, M2S-HTSC VIII, Dresden, Germany, 11.07.2006

* Zogg H.
Applied research on semiconductor devices: Infrared optoelectronics and thin film solar cells;
Societe Fribourgoise de Chimie, SFC, Univ. Fribourg, 25.4.2006